Queen Mary, University of London

School of Engineering and Materials Science

Modified TiO_2 Photocatalysts for the Degradation of Organic Pollutants and H_2 generation via Solar Energy Conversion

Armando M. Lacerda

Supervisors: Prof. Steve Dunn & Prof. Igor Larrosa

This thesis is submitted in partial fulfilment of the requirements for the degree of Doctor of Philosophy

July 2015

DECLARATION

I, Armando M. Lacerda Neto, confirm that the research included within this thesis is my own work or that where it has been carried out in collaboration with, or supported by others, that this is duly acknowledged below and my contribution indicated. Previously published material is also acknowledged below.

I attest that I have exercised reasonable care to ensure that the work is original, and does not to the best of my knowledge break any UK law, infringe any third party's copyright or other Intellectual Property Right, or contain any confidential material.

I accept that the College has the right to use plagiarism detection software to check the electronic version of the thesis.

I confirm that this thesis has not been previously submitted for the award of a degree by this or any other university.

The copyright of this thesis rests with the author and no quotation from it or information derived from it may be published without the prior written consent of the author.

Signature:

Date:

Details of collaborations and publications

1. Lacerda, A.M., Larrosa, I. & Dunn, S., 2015, *Plasmon enhanced visible light photocatalysis for TiO_2 supported Pd nanoparticles*, Nanoscale, DOI: C5NR03659C
2. Lacerda, A.M., Larrosa, I. & Dunn, S., 2014, *Highly Efficient Plasmonic Palladium-Titanium Dioxide Co-Catalyst in the Photodegradation of Rhodamine B Dye*, Advances in Science and Technology, 93, pp.184–189. DOI: AST.93.184
3. Lacerda, A.M., Larrosa, I. & Dunn, S., 2015, *TiO_2 supported Pd co-catalysts for solar hydrogen generation from the photo-induced reforming of methanol,* Advanced Energy Materials, Under Review

“Religion is a culture of faith; science is a culture of doubt.”

— Richard Feynman

ACKNOWLEDGEMENTS

I would like to express my sincerest gratitude to Professors Steve Dunn and Igor Larrosa for their supervision and support for the duration of my doctoral studies. Thank you for always encouraging and inspiring new ideas.

I would also like to thank the members of both the Dunn group and the Larrosa group, past and present, for providing a stimulating and enjoyable working environment, and for the engaging scientific and non-scientific discussions. Special thanks to Dr. Joe Briscoe for all your help, interest and input. It has truly been a pleasure working with you all.

I would also like to extend a huge thank you to my family and friends for their support over the years.

To my partner Fiona Woods – thank you for your endless patience, help and support.

ABSTRACT

Titanium dioxide (TiO_2) is one of the most widely used and studied semiconductor photocatalysts due to its stability, low toxicity and natural abundance. However, its wide band gap of 3.2 eV limits its photoactivity to the ultraviolet (UV) region of the electromagnetic spectrum. In order to take advantage of the freely available and sustainable energy from the Sun it is necessary to modify the physical properties of TiO_2 to sensitise its surface to visible light excitation.

In this thesis, a new photocatalyst was synthesised using a photochemical reduction procedure to deposit nanostructured Pd metal onto TiO_2. The catalyst was systematically optimised to improve its photocatalytic activity.

The new photocatalyst consisting of Pd nanoparticles of 2 – 4 nm in diameter deposited on 20 nm TiO_2 displays an 8% enhancement in solar light harvesting capability compared to the unmodified TiO_2. This increased photo-response of the modified photocatalyst corresponded to a reaction half-life for rhodamine b decolourisation of 0.5 min compared to the 9.4 min for pristine TiO_2 under identical reaction conditions. The improvement in the visible light activity is due to a significant red-shift in the absorption profile of the catalyst, which is associated with the visible light active local surface plasmon resonance of the Pd nanostructures supported on TiO_2. This overall red-shift in the light harvesting potential of the catalyst leads to photocatalytic activity for photo-excitations up to 600 nm.

The modified TiO_2 was also tested in the ambient temperature, photo-induced reforming of methanol to produce hydrogen gas (H_2). The highest rate of H_2 generation, which was measured at 5820 μmol/hour/gram of catalyst, corresponded to a solar to

hydrogen conversion efficiency of 0.95%. This value represents a 14% increase in the rate of H_2 production of similar systems and is among the highest obtained in the literature for TiO_2 modified with platinum group metals (PGMs).

Table of Contents

LIST OF FIGURES

LIST OF TABLES

LIST OF EQUATIONS

$$S_A = \pi\left(\frac{d}{2}\right)^2 = \pi\left(\frac{4.5\text{cm}}{2}\right)^2 = 15.9\text{cm}^2 \quad (3.7)$$ 83

$$P = I_s \times S_A = 100\text{mW/cm}^2 \times 15.9\text{cm}^2 \approx 1.6\text{W} \quad (3.8)$$ 83

$$E_{in} = Pt = 1.6\text{W} \times 3600\text{s} = 5.76\text{kJ} \quad (3.9)$$ 83

$$E_{out} = (0.67 \times V_{H_2} \times \Delta G^0_{MeOH}) + (0.33 \times V_{H_2} \times \Delta G^0_{H_2O}) \quad (3.9)$$ 84

$$E_{out} = \frac{V_{H_2}}{3}\left[2\Delta G^0_{MeOH} + \Delta G^0_{H_2O}\right] \quad (3.10)$$ 84

$$C_0 - C_{MS} = C_f \quad (3.11)$$ 88

$$wt\% = \left(C_f \diagup 1000\right) \times 100 \quad (3.12)$$ 89

$$(1 - C \diagup C_o) \times 100 = \%\text{adsorption} \quad (3.13)$$ 91

$$r = -\frac{dC}{dt} = \frac{k_r K_a C}{1 + K_a C} \quad (3.14)$$ 93

$$-\frac{dC}{dt} = k_{app} C \quad (3.15)$$ 93

$$\ln \frac{C_0}{C} = k_{app} t \quad (3.16)$$ 93

$$C = C_0 e^{(-k_{app} t)} \quad (3.17)$$ 94

$$C_0 e^{(-k_{app} t)} \equiv C_0 e^{\frac{-t}{\tau}} \equiv C_0 \left(\frac{1}{2}\right)^{\frac{t}{t_{1/2}}} \quad (3.18)$$ 94

$$-k_{app} t \equiv -\frac{t}{\tau} \equiv \frac{t}{t_{1/2}} \ln\left(\frac{1}{2}\right) \quad (3.19)$$ 94

$$-k_{app} \equiv -\frac{1}{\tau} \equiv -\frac{1}{t_{1/2}} \ln(2) \quad (3.20)$$ 94

LIST OF ABBREVIATIONS

AM	air mass
CB	conduction band
CVD	chemical vapour deposition
DFT	density functional theory
DoS	density of states
DR	diffuse reflectance
DSSC	dye sensitised solar cells
FLAPW	full-potential linearized augmented plane wave
GC	gas chromatography
HOMO	highest occupied molecular orbital
ICP	inductively coupled plasma
IEP	isoelectric point
LSPR	localised surface plasmon resonance
LUMO	lowest unoccupied molecular orbital
MeOH	methanol
PAO	photo-assisted oxidation
PCO	photocatalytic oxidation
PGM	platinum group metal
PSPR	propagating surface plasmon resonance

PVP	poly(N-vinyl-2-pyrrolidone)
PZC	point of zero charge
Redox	reduction/oxidation
RET	resonant energy transfer
RhB	rhodamine b
SPR	surface plasmon resonance
STH	solar to hydrogen
TCD	thermal conductivity detector
TEM	transmission electron microscope
TiO_2	titanium dioxide
UV-vis	ultraviolet/visible
VB	valence band
XPS	x-ray photoelectron spectroscopy
XRD	x-ray diffraction

1 Introduction

The growing need to develop alternative sources of clean, sustainable and renewable energy has arisen from the continuing depletion of fossil fuels and the accumulation of CO_2 in the Earth's atmosphere due to the growing energy demands of an ever increasing global population.

The Sun could provide an abundant source of sustainable energy for the production solar fuels if its power could be harvested efficiently to photochemically produce H_2 via the photolysis of water[1–3] or from the reforming of biofuels,[4,5] using heterogeneous catalysis as an alternative to traditional methods. Similarly, solar energy could also be used for the environmental remediation of toxic pollutants such as the decontamination of industrial effluents in rivers, the depollution of oil spills in oceans or provide a source of clean drinking water via the complete mineralisation of contaminants to CO_2 and H_2O. For example, the use of commercial dyes by manufacturing industries such as the textile, pharmaceutical, paint and cosmetic industries regularly results in the release of excess contaminants into the local environment posing a threat to both aquatic and human populations.[6] Photocatalysis is a promising method for the effective treatment of this industrial effluent.

Heterogeneous photocatalysis relies on the unique properties of semiconductor materials to harvest incident light and drive reactions in a wide range of applications, Figure 1.1. However, the photochemical conversion efficiencies of heterogeneous photocatalyst systems remains low since most systems are limited to operation under UV light and are not yet viable for industrial scale applications. Efficiencies must increase to at least 10%[2,7] for industrial and commercial viability. The 'holy grail' in this field is to

design a photocatalyst capable of effectively harvesting and converting visible light energy, in order to maximise the conversion efficiency of solar and artificial light driven reactions of such systems for practical applications.

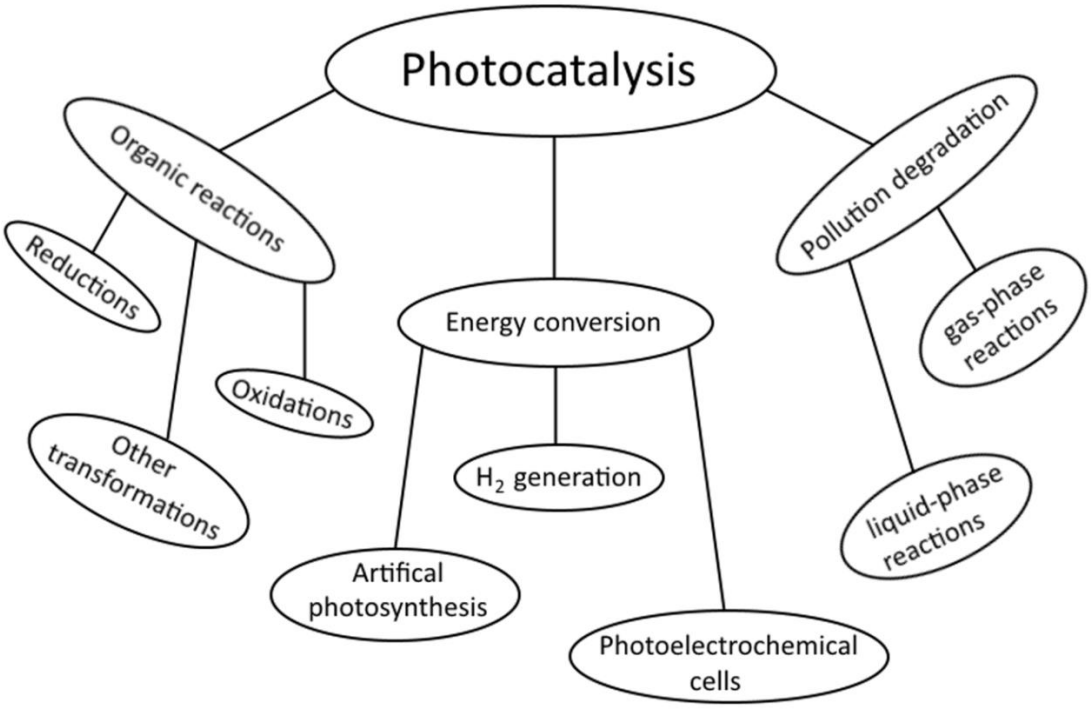

Figure 1.1 The main applications of photocatalytic reactions

Since the first reported system capable of producing H_2 from aqueous solutions under UV light was discovered in 1972,[8] considerable efforts have been made over the last 40 years to improve the physical properties of semiconductor materials. The aim has been to both increase the photocatalytic activity and extend the photo-reactivity of these systems into the visible region to maximise the solar light harvesting potential.[9–11]

One of the main materials used in photocatalysis has been the semiconductor TiO_2. It is a material that shows excellent photocatalytic properties, good stability, is low in toxicity, relatively low in cost and widely available.

The photo-active properties of TiO_2 arise from the absorption of incident super band gap photons resulting in the generation of excited charge carriers within the material known as electron-hole pairs. These are the species that react with adsorbed compounds on the surface of the semiconductor.

The main limitation to this process is rate at which the excited charge carriers recombine. The recombination of electron-hole pairs prevents further reactions from taking place and essentially deactivates the system. Chemical alterations to improve the physical properties of TiO_2 have been widely studied and include techniques such as bulk or surface chemical modification.[12–14] The efficiency of the modified catalyst can be increased by preventing the recombination of excited charge carriers responsible for redox reactions with adsorbates on its surface; by extending its optical response into the visible spectrum or a by the combination of both.[15,16]

This thesis reports the investigation into the synthesis of a novel TiO_2 based photocatalyst that contributes an efficient visible light harvesting system to the field of photocatalysis.

The investigation into the photocatalytic activity of this new photocatalyst focussed on the liquid-phase degradation of organic pollutants and the generation of H_2 under simulated solar light. The principle objectives of this project were:

- To synthesise and investigate the physical properties of a new photocatalyst based on TiO_2 supported metal systems and assess its photocatalytic activity in the degradation of dyes and in H_2 generation under solar irradiation.

- To optimise the physical properties of the photocatalyst via a systematic variation of the synthesis parameters in order to improve its photocatalytic efficiency.
- To investigate the visible light response of the system and the effect of metal loading of the photocatalyst on its activity.
- To investigate the optimum parameters for degradation reactions under solar conditions and determine the effect of catalyst loading, dye loading and pH.
- To investigate the potential of the photocatalyst for H_2 generation and determine the reactions mechanisms occurring on the surface of the catalyst.
- To investigate the effect of spatially separating the reduction and oxidation reactions on the surface of the catalyst and determine the capability of the photocatalyst to drive over all water splitting reactions.

This thesis has 7 chapters. These are:

Chapter 1: Introduction.

Chapter 2: Review of the background literature and relevant concepts in TiO_2 photocatalysis. A broad overview is given on the techniques used in modifying TiO_2 systems with a focus on the techniques used in this work.

Chapter 3: The materials used and the methods to carry out the various tests and characterisations are described.

Chapter 4: The synthesis and optimisation procedure of the photocatalyst is investigated by studying the effects of changing parameters related to photochemical deposition of Pd on the physical properties and photocatalytic activity of the catalyst.

Chapter 5: The potential of the photocatalyst for applications in the degradation of pollutants is tested. The effect of catalyst loading, pollutant concentration, pH on the efficiency of the system and the recyclability of the catalyst is discussed.

Chapter 6: The photocatalytic activity of the catalyst in the generation of hydrogen via the photo-reforming of methanol is investigated.

Chapter 7: A summary of the overall conclusions are presented and suggestions for future work are made.

2 Literature review

2.1 Heterogeneous photocatalysis

The term photocatalysis can be defined as a combination of the words 'photoreaction' and 'catalysis'. It refers to a chemical transformation of a species induced by the absorption of electromagnetic radiation, or photoreaction, which is accelerated by the presence of a catalyst. This definition includes photosensitisation, where a chemical compound may undergo a transformation due to the absorption of light by another compound - the photosensitiser, but it does not apply to the acceleration of a thermal reaction by electromagnetic irradiation. The photocatalyst can accelerate the photoreaction in one of two ways: it can interact with a substrate in its original or excited state, or it can interact with the products of the photoreaction.

Heterogeneous photocatalysis can be described as the acceleration of a photoreaction in which the reactant and the photocatalyst exist in different phases, and where reactions occur on the surface of the photocatalyst. There are two main categories that reactions in heterogeneous photocatalysis can be grouped into and this depends on whether it is the reactant or the photocatalyst that is the subject of the initial photoexcitation. When the photocatalyst is induced into a photo-excited state, and transfer of an electron to an adsorbed molecule in its ground state occurs, this is termed a sensitised photoreaction. If the adsorbed molecule, such as a dye molecule for example, is initially photo-excited and reacts with a ground state photocatalyst, this is known as a catalysed photoreaction. These two definitions represent different pathways under which photocatalytic reactions can occur. In both cases the end result is the

reduction or oxidation of a target compound resulting in its subsequent conversion into a desired product or products.

The initial interest in heterogeneous photocatalysis with semiconductors for the purposes of solar fuel production and other photocatalytic reactions such as the breakdown of organic pollutants, was driven by the work of Fujishima and Honda in 1972.[8] They reported the photolysis of water by the UV light irradiation of a titanium dioxide (TiO_2) single crystal subject to a small electrical bias with a platinum counter electrode. Their discovery represents a landmark into the research of photo-induced redox reactions on TiO_2 photocatalysts via solar energy conversion.

2.2 Semiconductors

Semiconductors are ideal materials for heterogeneous photocatalysis since their unique electronic structure allows for the spatial separation of excited charge carriers upon the absorption of photons with energies larger than or equal to the semiconductor energy band gap. The spatially separated charge carriers can then react with target species adsorbed to the surface of the semiconductor in reduction or oxidation (redox) reactions. If the semiconductor remains unchanged after continuous and exothermic interfacial charge transfer, the process can be described as heterogeneous photocatalysis.[17]

2.2.1 Origin of the electronic band structure of semiconductors

The electrons associated with a single atom are known to occupy atomic orbitals at discrete energy levels. When a number of atoms come together to form a solid the electron wavefunctions occupying neighbouring atoms begin to overlap. The Pauli Exclusion Principle states that the electrons within a system cannot occupy the same

quantum state and this leads to the splitting of the energy levels within the atomic orbital. Since the number of electrons associated with the large quantity of atoms that make up a solid is so vast, and the difference between the energy states of the electrons is infinitesimally small, the electronic structure can be approximated to a continuous band. Figure 2.1 shows the splitting of the energy levels within the electron orbitals 2 s and 2 p as a function of the interatomic separation, where the 2 s orbital contains 2 N states and the 2 p orbital contains 6 N states (N being the number of atoms in the solid). As the distance between the orbitals decreases, the orbitals merge and split into two bands each containing 4 N states. At a temperature of zero Kelvin the lower band, known as the valence band (VB) is completely filled with electrons while the higher band, or conduction band (CB) is completely empty.

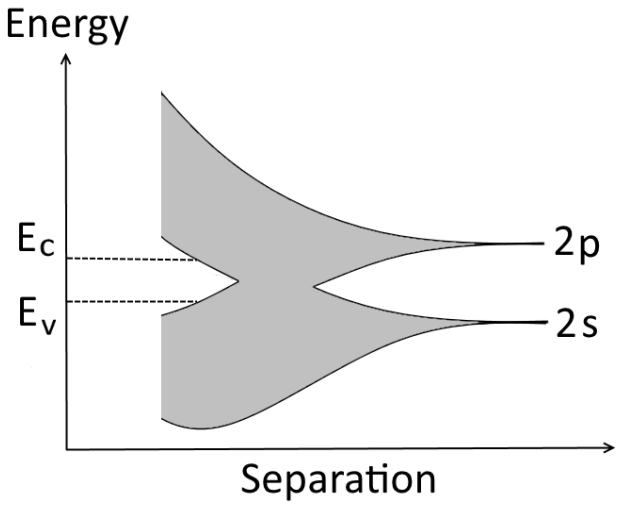

Figure 2.1 The splitting of electronic energy levels results in the formation of a continuous electronic band

The band structure of semiconductors is an extension of the concept of molecular orbitals where the regions of interest are the highest occupied molecular orbital (HOMO), which in the semiconductor forms the VB and the lowest unoccupied

molecular orbital (LUMO), which is the CB. The region that makes up the difference in energy between the highest energy level in the VB and the lowest energy level in the CB is a forbidden zone where electrons cannot exist and is known as the energy band gap (E_g). The origin of the band structure as a function of the number of electronic orbitals is shown in Figure 2.2.

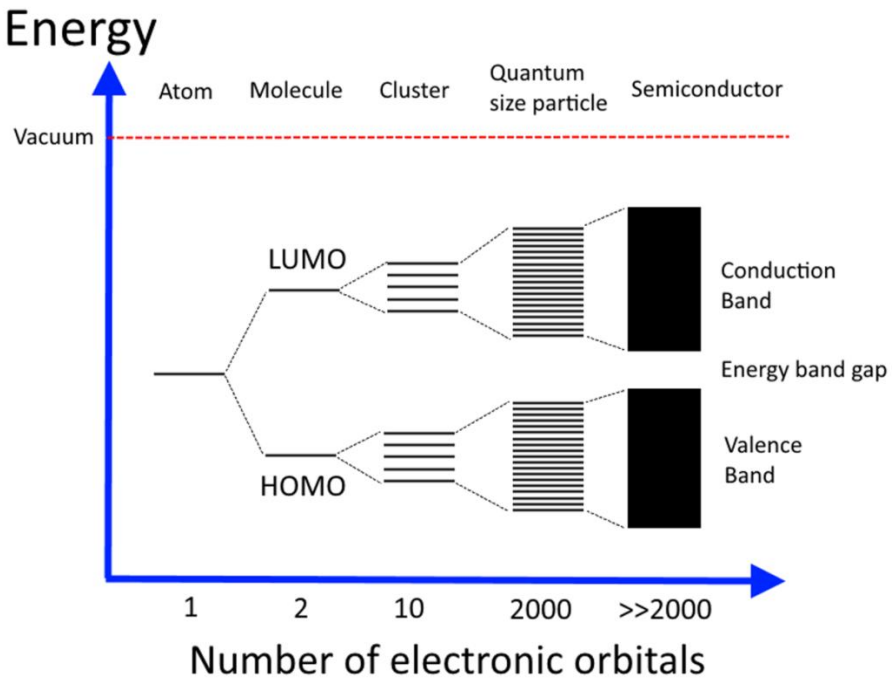

Figure 2.2 Origin of the band structure of semiconducting materials (adapted from Hoffman et al., 1995)[18]

The electrical conductivity of a material requires the movement of electrons to occupy partially filled states in the CB of that material. In the case of metals, there is an overlap of the CB and the VB, and so the vacant states in the CB can be readily occupied. Insulators have a relatively large E_g such that electrons cannot be promoted to the CB and so the material is not electrically conductive. However, the E_g for semiconductors is sufficiently small that electrons may be promoted from the VB to the CB via some

transfer of energy to the material. The promotion of an electron to the CB creates an electron vacancy in the VB that can be thought of as a positively charged hole.

The hole is a mobile entity since it can be filled by another electron, which in turn creates a vacancy in the space where it transferred from. The conductivity of metals, semiconductors and insulators as a function of the E_g is shown in Figure 2.3.

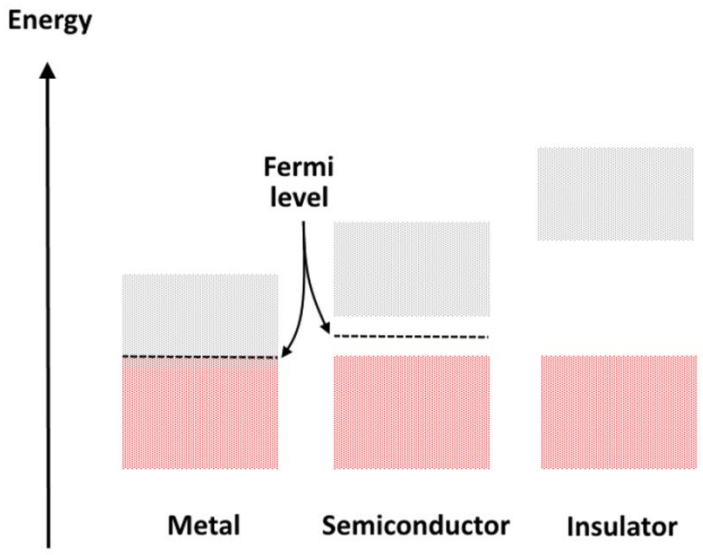

Figure 2.3 The conductivity of solid state materials in terms of the band gap value

Electron transfer from the VB to the CB in a semiconductor can be achieved via an excitation that is sufficiently energetic to overcome E_g. Furthermore, there are two different types of band gap that exist for semiconductors and the type of transition that an electron has to make is determined by the lattice structure of the semiconductor. The crystal structure of semiconductors can be described by its Bravais lattice. The Fourier transform of this lattice gives the reciprocal lattice of the crystal in what is known as momentum or k space. The minimum energy state of the CB and the maximum energy state of the VB, and consequently the type of transition that electrons must make, are determined by the value of the k vector. If the values of the k vector for the VB and CB

are equal to each other the band gap is known as direct, Figure 2.4 a. However, if the k vectors are not equal the band gap is known as indirect, Figure 2.4 b.

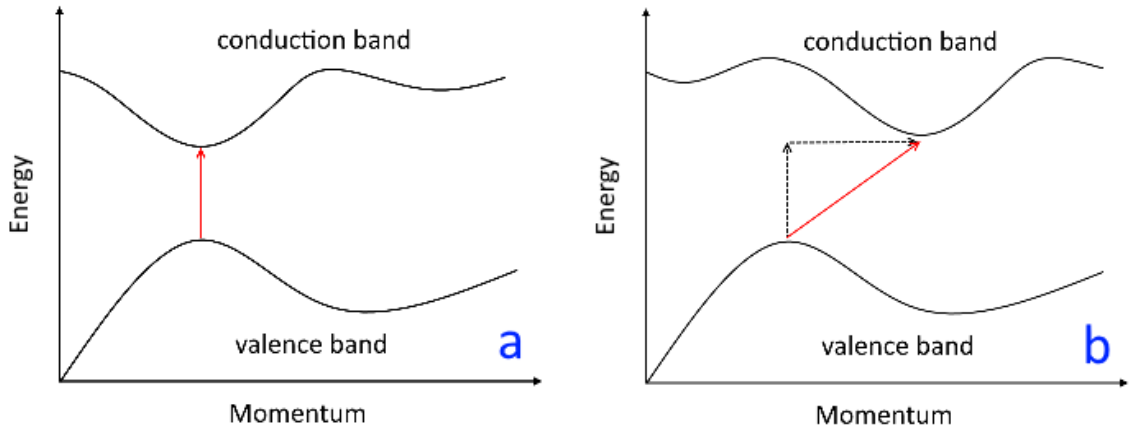

Figure 2.4 The type of transition electrons make in semiconductors that have a) a direct band gap and b) an indirect band gap

In semiconductors with a direct band gap, the absorption of photons can provide the energy required to produce an electron-hole pair as there is no change in momentum. However, if the band gap is indirect a change in momentum is required and the absorbed photon must interact with a lattice vibration, known as a phonon, in order to gain or lose the momentum necessary to complete the transition to the conduction band. The absorption process can also proceed in reverse where photons are emitted as the electrons and holes recombine in the valence band. The transitions are significantly slower for semiconductors with an indirect band gap since three entities; an electron, a photon and a phonon must intersect as opposed to just two, as is the case of semiconductors with a direct band gap.

The photocatalytic properties of a semiconductor are thus directly related to the magnitude of its E_g (and type of transition), which is typically between 1 and 4 electron volts (eV). The band gap is 0 eV for conductors and greater than 4 eV for insulators.[19]

There is a large range of materials that have been discovered over the last few decades with suitable E_g values for photocatalytic reactions and some of these common elemental and compound semiconductors are shown in Table 2.1.

Table 2.1 E_g values of some well known semiconductors (adapted from Rajeshwar, 2007)[20]

Semiconductor	Band gap energy/ eV	Wavelength/ nm
ZnO	3.35	370
TiO_2 (anatase)	3.20	387
TiO_2 (rutile)	3.00	413
CdS	2.42	512
GaP	2.30	539
CdSe	1.70	729
CdTe	1.50	827
GaAs	1.40	886
InP	1.35	918
Si	1.17	1060

2.2.2 Band engineering

The E_g of a semiconductor can be manipulated by a process called doping. Doping consists of the introduction of impurities to the bulk of the material. These impurities occupy energy states close to either its VB or CB edges, Figure 2.5. This results in electrons or holes occupying energy states, and requiring less energy to be promoted to the CB. A semiconductor is considered p-type if the impurities introduced create vacant states, or holes, close to the upper edge of the VB thus promoting easier transition of electrons. The majority carriers in p-type semiconductors are holes. N-type semiconductors are doped with impurities that introduce electron states close to its CB where the majority carriers are electrons.

Doped semiconductors are classed as extrinsic, while undoped semiconductors are known as intrinsic and may also be p-type or n-type. In extrinsic semiconductors the redistribution of charge carriers within the material will alter the position of the Fermi level.

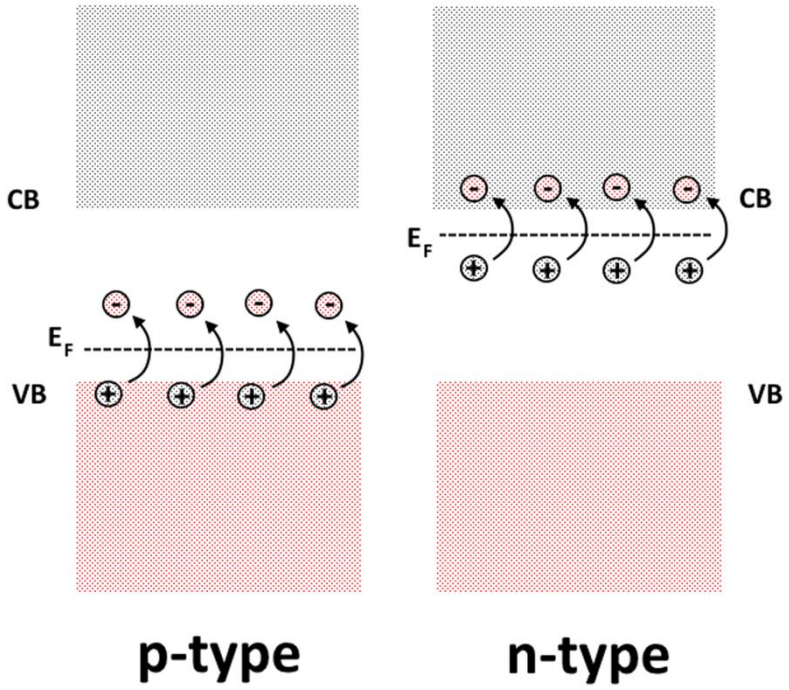

Figure 2.5 Impurities introduced to a material increasing the number of vacant energy states close to the VB results in a p-type semiconductor (left). Impurities that add electronic states close to the CB edge results in an n-type semiconductor

The Fermi level is an important parameter in solid state materials that determines its electronic properties. At thermodynamic equilibrium, the Fermi level represents a region of energy states at which there is a 50% probability of it being occupied by electrons. In an intrinsic semiconductor, the Fermi level lies at a value equidistant from the CB and the VB. For p-type semiconductors the Fermi level lies close to the VB, while for n-type semiconductors the Fermi level lies close to the CB.

As described above, the doping of semiconductors results in the modification of its band structure and this can have beneficial effects in terms of improving its physical properties for photocatalytic applications.

2.3 Semiconductor photochemistry

The generation of an electron-hole pair in a semiconductor allows for the conversion of light into electrical or chemical energy and is the basic principle that underpins the study of photoelectrochemistry and photocatalysis.[18,20–23] The absorption of a super-band gap photon, leading to photocatalytic redox reactions on the surface of the semiconductor is illustrated in Figure 2.6. Photocatalysis can be summarised as the photoexcitation and separation of charge carriers, the transportation of charge within the material, and surface charge transfer. Photoexcitation of a semiconductor with electromagnetic radiation equal to or exceeding E_g induces a charge separation in the material. Incident super-band gap photons are absorbed by electrons which are promoted from the semiconductor VB to its CB. As the excited electrons are delocalised from the VB, electron-hole pairs are created and diffuse towards the surface of the material.

$$e^- + A \rightarrow A^- \quad \textbf{(2.1)}$$

$$h^+ + D \rightarrow D^+ \quad \textbf{(2.2)}$$

Photogenerated electrons and holes that reach the surface of the semiconductor react with electron acceptors in reduction reactions or with electron donors in oxidation reactions (represented by A and D in Figure 2.6), which are chemical species adsorbed on the surface of the material.

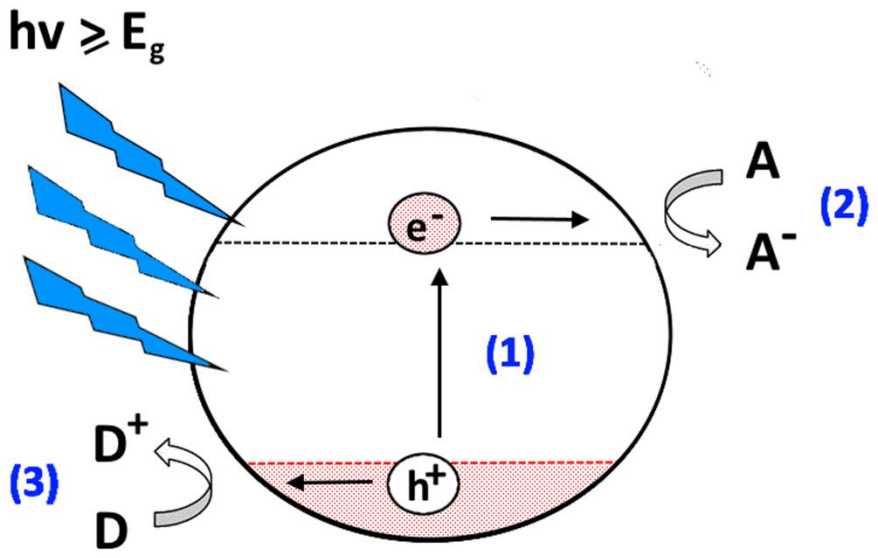

Figure 2.6 The origin of the generation of an electron-hole pair as a result of the absorption a super-band gap photon due to incident irradiation on a semiconductor particle

One of the main limitations in semiconductor photocatalysis is the recombination of photogenerated carriers. This process occurs between the photo-generation of an electron-hole pair and the surface charge transfer in the process described in Figure 2.6. After the photo-induced charge separation in the semiconductor, electrons and holes must reach the surface of the material to react with adsorbed chemical species via surface charge transfer. However, a large proportion of the excited charge carriers recombine before reaching the surface, dissipating the absorbed energy as heat and as a result no redox reactions can take place with adsorbed species.

2.3.1 Factors influencing photoactivity of semiconductors

The value of E_g, the recombination rate of charge carriers and the surface charge transportation properties in semiconductors are the main parameters that can significantly affect their photoactivity. These mechanisms are influenced by the electronic, bulk and surface structure, which are intrinsic properties of the semiconductor. Other factors that influence the photocatalytic efficiency of a reaction

are associated with the semiconductor size and morphology, and are considered extrinsic factors.

The conductive properties of semiconductors arise from their unique electronic band structure which allows for the movement of electrons induced via thermal or photochemical excitation. Nonetheless, this band structure can be a limiting factor to the photoactive properties of a photocatalytic material concerning reactions under solar or visible light irradiation. This is because the energy required to initiate the movement of electrons can be greater than the energy associated with the incident light, in which case, electrons cannot be promoted to the CB. Another limiting factor is the lifetime of the excited charge carriers and the charge transportation properties within the material, which is highly dependent on its crystal structure.[21] The other parameter affecting the photocatalytic activity of a semiconductor is related to the transportation of charge carriers at its surface to adsorbed species. This may be influenced by the introduction of heterostructures on the catalyst surface.

Approaches to improving the limitations of semiconductors in photocatalytic reactions fall into three general categories: crystal growth, doping and heterostructuring. These aspects of semiconductor modification can have a significant impact on the optical response range, the redox potentials of excited charge carriers and on the bulk and surface charge transportation properties of the material.

One of the most widely studied semiconductors for photocatalytic applications in the last few decades has been TiO_2. As such, the modification processes and subsequent effects are among the most documented in the field.

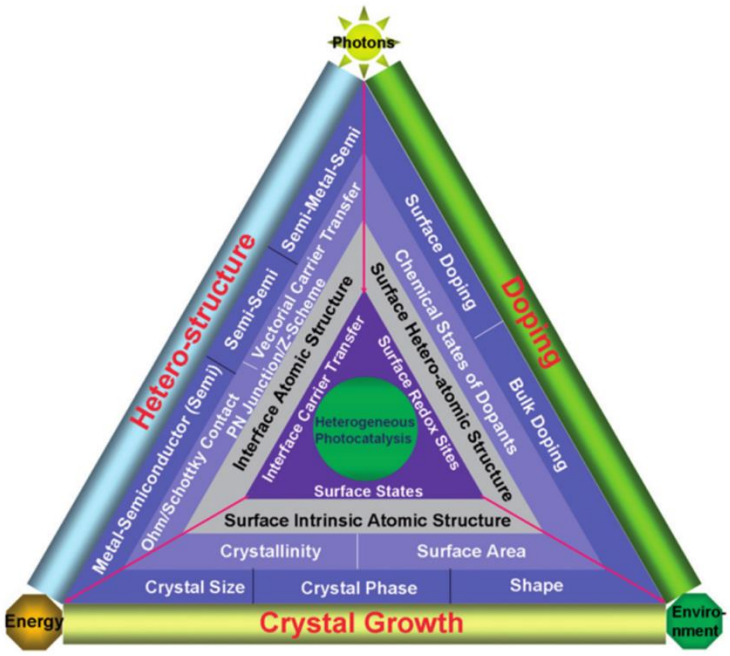

Figure 2.7 The relation between crystal growth, doping and heterostructure in semiconductor photocatalysis (adapted from Liu et al., 2010)[14]

Its use in a vast range of photo-driven applications has been largely due to the beneficial modification of its physical properties via a greater understanding of the mechanisms governing the crystal structure, the concentration and nature of dopants, and the heterostructure engineering. This correlation between the main aspects of the crystal growth, doping and heterostructuring are shown in Figure 2.7.

2.4 TiO_2 photocatalysts

The first photoactive effects of TiO_2 were reported by Lenz in 1920 who observed a darkening of the material due to UV irradiation.[24] Goodeve and Kitchener then described its photosensitising effects in 1938 when used as a white pigment in paints and wallpapers.[25] However, it was not until 1972 with the work of Fujishima and Honda that intense research into the photocatalytic properties of TiO_2 began in earnest.

Over the last 4 decades TiO_2 photocatalysts have been used in a wide range applications from water splitting and solar fuel conversion,[1,2,4,26–43] to organic pollutant decomposition for environmental remediation[6,44–56] and they have been incorporated in materials for antimicrobial and self-cleaning surfaces.[57–64]

One of the main drawbacks of TiO_2 photocatalysts in terms of solar energy harvesting is the large E_g of approximately 3.2 eV of unmodified TiO_2. This wide band gap limits the photoactive properties to the UV region of the solar spectrum, of which approximately only 4% is composed of UV irradiation. In order to maximise the available solar energy, it is necessary to sensitise the TiO_2 surface to the visible region by extending its optical response range. Another important parameter that can improve the efficiency of TiO_2 photocatalysts is the bulk and surface charge transportation properties.[17] The bulk structure can be influenced by the manipulation of the crystal growth to alter the degree of crystallinity, while the engineering of heterostructures on the TiO_2 surface can promote the efficient transfer of charge.[16]

2.4.1 Crystal structure

TiO_2 is an intrinsic n-type semiconductor that exists in three naturally occurring crystal phases known as anatase, rutile and brookite, and can be synthesised under laboratory conditions. All three phases are composed of Ti^{4+} atoms and six O^{2-} coordinated together to form a TiO_6 octahedron. Distortions in the octahedra of each phase results in the formation of crystal structures that differ in configuration for each of the three phases. Both anatase and rutile have a tetragonal crystal structure, while brookite is orthorhombic. Figure 2.8 shows the three naturally occurring phases of TiO_2. Of the

three TiO_2 polymorphs the most stable configuration is rutile however, the most photocatalytically active phase is generally considered to be anatase.[65,66]

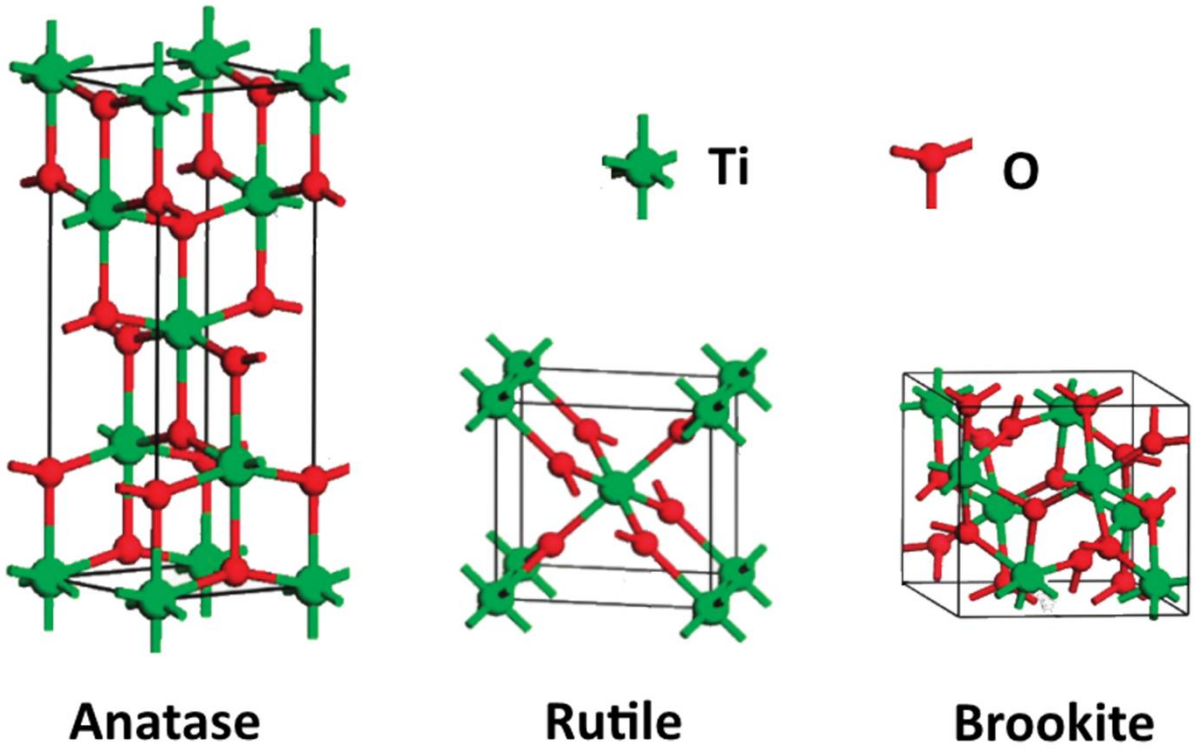

Figure 2.8 The three polymorphs of TiO_2: anatase, rutile and brookite are shown (Adapted from Zhang et al., 2014)[66]

This is thought to be due to the band structure of anatase compared with that of rutile or brookite. The band gap values of anatase, rutile and brookite are reported to be 3.2 eV, 3.0 eV and 3.3 eV, respectively.[54] Density of states (DoS) considerations and density functional theory (DFT) calculations[66] have shown that anatase has an indirect band gap whereas rutile and brookite both have direct band gap transitions. The result is longer lifetimes of photogenerated charge carriers in anatase photocatalysts compared with either the rutile or brookite phases.

The recombination rate of the photogenerated charge carriers is one of the main limitations to TiO_2 photocatalysts. It has been shown that the degree of crystallinity of single crystal TiO_2 photocatalysts can affect its charge transportation properties such

that a high level of purity will more efficiently transport excited charge carriers through the crystal lattice. This is due to the lack of defects and imperfections within the bulk that can act as charge recombination centres.[67] In colloidal systems using TiO_2 particles in the micro or nano scale, a high level of crystallinity is difficult to achieve during preparation and so surface and bulk defects and irregularities exist that significantly affect the photo-efficiency of the system.[21] The degree of crystallinity of a TiO_2 photocatalyst may be controlled via the application of a thermal treatment, which can drive out defects in the crystal lattice and increase the phase purity.[68] However, for particulate systems the thermal annealing process will cause agglomeration of the particles resulting in a reduction of the active surface area of the photocatalyst and the subsequent decrease in photo-efficiency of the system.[69] Therefore, a balance must be reached between the degree of crystallinity and size of particulate TiO_2 photocatalysts in order to achieve optimum efficiency.

There has been some research reporting the benefits of mixed phase titania, such as anatase/rutile for example in terms of improved charge separation properties.[70,71] The increased photocatalytic activity of the mixed phase systems are thought to arise from the interfacial electron transfer at the phase boundary. However, there are two opposing views regarding the mechanism of this mixed phase system. Briefly, one is that rutile can act as the electron sink due to its lower CB edge compared with anatase, while the other is that low-energy trap sites in the anatase phase capture excited electrons from the rutile phase.[14] More recently, Scanlon et al. have published a comprehensive study on the band alignment of mixed phase anatase and rutile photocatalysts supporting the transfer of electrons from the CB of the rutile phase to the lower energy

CB of the anatase phase.[72] Irrespective of the charge carrier transfer mechanism between the two phases, it is clear that a synergistic effect exists when the interface of these two distinct phases of TiO_2 are brought into contact in a mixed phase photocatalyst system.

Perhaps the most well-known and widely investigated mixed phase TiO_2 photocatalyst is the commercially available form commonly referred to as P25. P25 is composed of nanoparticles with an average diameter of 21 nm, a surface area of approximately 50 m^2/g and an anatase to rutile proportion of around 4:1.[73,74] It is often used as a reference catalyst with which to compare the activity of new modified TiO_2 based photocatalysts due to its relatively high photocatalytic activity.[75]

2.5 TiO_2 modification

2.5.1 Doping

The band structure of semiconductors can be altered via the bulk chemical modification process of doping. For TiO_2 the process is usually carried out in order to extend its optical response range into the visible region by replacing the Ti^{4+} or the O^{2-} ions in the lattice structure with metal or non-metal substitutes. Doping sites are not restricted to the substitution of atoms within the lattice but may also be interstitial, where dopants are located between the Ti^{4+} and O^{2-} sites.[76,77] The dopant species are usually incorporated into the lattice structure of TiO_2 to reduce the E_g value by either lowering the upper edge of the CB or raising the lower VB edge. This has the effect of sensitising TiO_2 to visible range wavelengths.

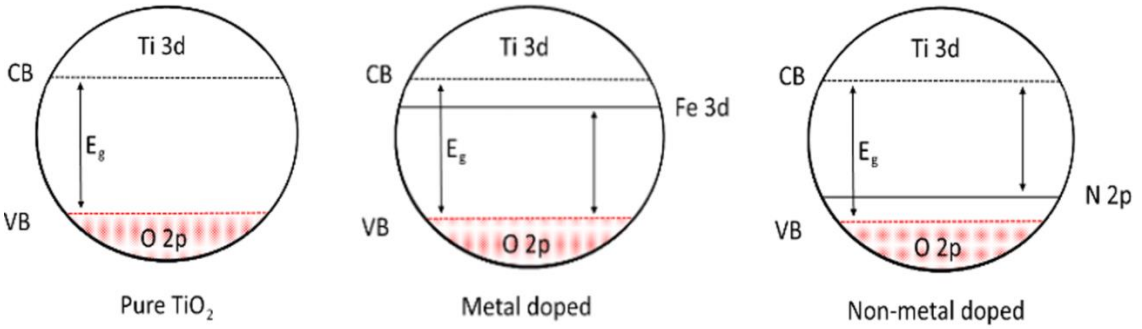

Figure 2.9 Examples of introduced states within the TiO_2 band gap due to metal and non-metal dopants using iron (Fe) and nitrogen (N) as representative elements to illustrate band gap narrowing

2.5.1.1 Metal doped TiO_2

Many transition metal elements have been used as dopants in TiO_2 photocatalysts[16,28,30,63,78–88] and the synthesis procedures generally fall into one of three categories: wet chemistry, high temperature treatment or ion implantation. The method of preparation of metal-doped TiO_2 photocatalysts can have an effect on the resultant band structure. As an example, Anpo et al. reported a significant difference in the resultant optical properties of chromium (Cr)-doped TiO_2 prepared via a wet impregnation method compared with those synthesised via ion implantation.[88] The increase in the optical response was found to be higher for the catalyst synthesised via the ion implantation method where a band to band red-shift was observed. In the same publication, the group used the ion implantation procedure to investigate the optical response of TiO_2 doped with a range of transition metals. They found a red-shift corresponding to the different dopants such that the magnitude of the red-shift for V > Cr > Mn > Fe > Ni, allowing the visible light absorption of these metal-doped TiO_2 photocatalysts. However, these red-shifts were observed under specific synthesis

conditions and only after the metal doped TiO_2 photocatalysts were subjected to calcination in O_2 at temperatures of 450°C – 550°C.

Another key factor in the use of dopants in TiO_2 photocatalysts is their ability to act as electron and hole traps, thus retarding the rate of charge carrier recombination. Choi et al., published a comprehensive study of the effects of doping TiO_2 with various different metals and found that the most important feature was the enhanced charge transport properties of TiO_2 as a result of an effective dopant.[16] The group proposed that dopants should act as both electron and hole traps in order to be photoactive. This is because the trapped electron or hole may recombine with its mobile counterpart. Their remarks were supported by the observation that dopants found coexisting in different oxidation states within the TiO_2 showed an increase in the photoactivity of the doped TiO_2. However, dopants with closed shell electronic configurations such as Li^+, Mg^{2+}, Al^{3+} and Zn^{2+} for example, were found to have an insignificant influence on the photoactivity of those systems.

In general, the doping of TiO_2 materials with metal ions is dependent on the type and concentration of dopant as well as the procedure of its introduction and should be carefully considered depending on the application of the photocatalyst.

2.5.1.2 Non-metal doped TiO_2

Most non-metal elements such as B, C, N and F have also been used as dopants in TiO_2 photocatalysts.[89–95] Among the non-metal dopants, N has perhaps shown the most promise in terms of improving the photoactivity of TiO_2 in the visible range.[96] Nitrogen can be easily introduced to the TiO_2 lattice as it is similar in atomic size to oxygen, is highly stable and has a small ionisation energy.[54]

The first report of N doping was by Sato in 1986 when he reported the visible light response of a TiO_2 photocatalyst that was prepared using NH_4OH during the calcination step.[97] However, it was not until the work of Asahi et al. in 2001 that research into the doping of TiO_2 with non-metal ions intensified. The groups' paper proposed a set of requirements in order to achieve visible light activity for TiO_2 from theoretical studies of DoS and full-potential linearized augmented plane wave (FLAPW) formalism calculations, which were supported by experimental observations.[89] They reported that in order to achieve visible light activity in TiO_2 the following criteria should be met: the dopant should produce states in the TiO_2 E_g that absorb visible light; the new impurity states and the resulting new lower CB edge should be as high as that of the TiO_2; new states in the E_g should overlap with band states of TiO_2 to allow the transfer of photogenerated charge carriers to the active sites at the surface. The last two considerations require that the dopant be an anionic rather than a cationic species since the introduction of metal cations often result on localised d-states within the band gap of TiO_2, which act as recombination centres.[89]

Non-metal doped TiO_2 catalysts have been synthesised via a range of techniques including sol-gel synthesis, sputtering deposition and chemical vapour deposition (CVD), with some comprehensive reviews into the visible light activity of a broad range of catalysts having been produced by Chen and Mao in 2007[98] and Fujishima et al. in 2008.[96]

As with metal doped TiO_2 photocatalysts, the preparation method, and the type and concentration of non-metal dopants influence the resultant band structure and the visible light activity of the catalyst.

2.5.2 Heterostructuring of TiO_2 catalysts

The engineering of the surface structure of TiO_2 to form heterostructures via chemical modification is carried out with the objective of increasing its visible wavelength response, as well as improving the interfacial charge transfer properties and selectivity towards organic compounds. The creation of a heterostructure poses some advantages compared with doping in terms of the separation of photogenerated charge carriers and the ability to spatially separate redox reactions and confine the reduction and oxidation to different active sites on the photocatalyst surface. Some of the main approaches to the engineering of heterostructures are shown in Table 2.2.

Table 2.2 Main strategies for engineering heterostructures with TiO_2 photocatalysts

Mechanism	Description	References
Semiconductor coupling	TiO_2 coupling with other semiconductors promotes the efficient charge separation and reduces the probability of charge carrier recombination	99–101
Sensitisation	Typically a dye molecule is used as a sensitizer to absorb visible light energy and transfer an electron to the CB of the semiconductor	102–106
Metal deposition	Noble metals are deposited on the TiO_2 surface to improve optical response and increasing photoactivity	52,107–109

2.5.2.1 Semiconductor coupling

TiO_2 photocatalysts coupled with other semiconductors are a type of heterostructured photocatalyst. These catalysts are based on a charge transfer mechanism between the two semiconductors in contact with one another. Upon irradiation, photogenerated charge carriers transfer from the lower VB maximum or CB minimum of one

semiconductor to the higher VB maximum or CB minimum of the other semiconductor. Examples of semiconductor/TiO_2 heterostructured photocatalysts are CdS/TiO_2 catalysts used in the degradation of aqueous pollutants,[99] and IrO_2/TiO_2 and $BiVO_4$/TiO_2, which are used for solar water splitting.[110,111]

The structure of the coupled semiconductors is usually in the form of TiO_2 supported semiconductor nanoparticles or in the form of core-shell structures. The geometry of these heterostructures in terms of particle size and contact surface can affect the photocatalytic efficiency of these systems.[112,113] The synthesis of these heterostructures typically involves long preparation times using complex procedures requiring high temperature treatments, inert atmospheres and multi-step processes.

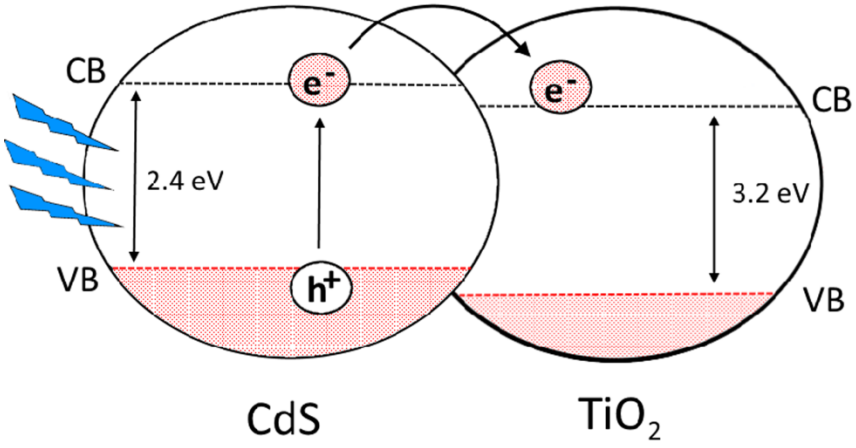

Figure 2.10 Semiconductor coupling taking CdS as a representative semiconductor coupled to TiO_2. The band gap for CdS is sufficiently narrow to allow visible light absorption. The photogenerated electron is transferred to the TiO_2 CB and can react with adsorbed species on the TiO_2 surface

Coupling of the semiconductors can result in synergistic effects by overcoming shortcomings in the individual components such as improved charge carrier trapping or wavelength response. However, one major drawback of these structures is the decrease in the redox potential of excited charge carriers due to the release of potential energy during transfer between the semiconductors.[14]

2.5.2.2 Dye sensitisation of TiO_2 surfaces

Sensitisation of the surface of TiO_2 with dyes is another approach to improving its optical response into the visible region. The most well-known example of this mechanism is the dye sensitised solar cell (DSSC)[114] however, dye sensitisation has also been employed as an efficient visible light harvesting mechanism in other reactions.[103–106] The basic mechanism of improved visible light response for the system involves the absorption of visible light photons by the dye, resulting in the excitation of an electron from the HOMO to the LUMO of the dye.

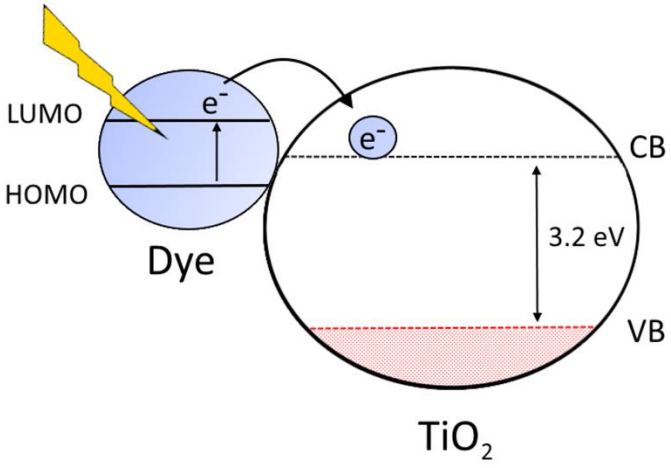

Figure 2.11 Visible light excitation of the dye promotes an electron from the HOMO to the LUMO followed by electron transfer to TiO_2 CB. Electron can then react with adsorbed species on TiO_2, which acts as a mediator.

The excited electron in the dye is then transferred to the TiO_2 which acts as a mediator between the excited dye molecule and an electron acceptor on the surface of the TiO_2. During this process, the VB of the TiO_2 remains unaffected and thus the LUMO of the dye molecule should be more negative than the CB of the TiO_2 in order for efficient charge transfer. The subsequent reactions that take place on the surface of the TiO_2 involve the formation of radicals that can start a chain reaction and ultimately lead to the degradation of the dye.[54]

An understanding of the mechanism governing the interfacial transfer between the excited dye molecule, the TiO_2 and the adsorbates is essential for these applications. This is because the electron transfer kinetics is highly dependent on the physical properties of the sensitizer, the TiO_2 and thus the interactions between the two.

2.5.2.3 Metal deposition on TiO_2

The deposition of metals on the surface of TiO_2 has been shown to improve its spectral response,[115–117] as well as reducing the rate of recombination of the photogenerated charge carriers by acting as electron and hole trap sites on the TiO_2 surface.[108,118] The metals used to decorate the semiconductor surface are typically noble metals such as Rh, Pt, Pd, Au, and Ag,[31,36,119–122] as well as other transition metals such as Mn and Co.[123] Some metal oxides such as RuO_2 and NiO[27,124,125] have also been successfully deposited onto TiO_2.

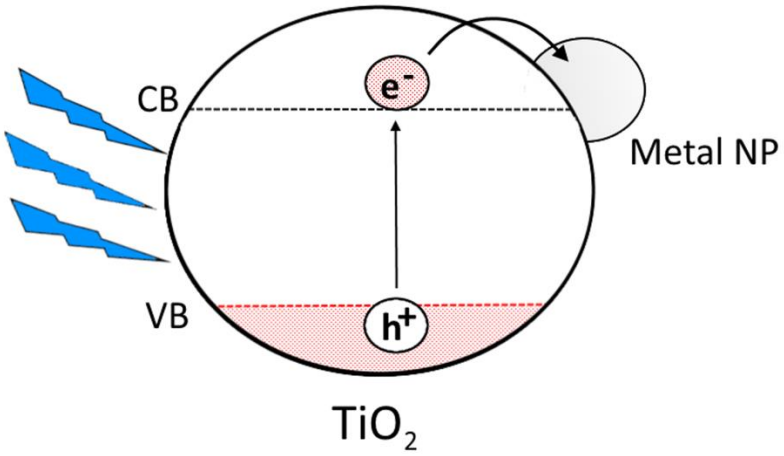

Figure 2.12 TiO_2 supported metal nanoparticles trap photogenerated electrons allowing holes to react with adsorbents on the semiconductor

The method of deposition proceeds from the reduction of metal cations in a metal salt precursor via photochemical, impregnation or hydrothermal reactions that anchor the metal nanoparticles to the TiO_2 surface. Figure 2.12 shows the concept of a supported

metal nanoparticle acting as trap site for the photogenerated charge carrier; in this case an electron. However, other compounds such as RuO_2 are thought to act as hole trapping sites when loaded onto TiO_2 supports.[17,126,127] The resultant photocatalyst is usually composed of nanoparticles randomly dispersed over the semiconductor surface, although techniques are constantly being developed to control the size, morphology and distribution of the supported nanoparticles.

2.6 TiO_2 supported metal co-catalysts

TiO_2 supported metal co-catalyst systems were described by Bard in 1979 where the TiO_2 powder supported Pt particle system could be thought of as a self-contained short circuited photoelectrochemical cell.[128] The same analogy was also made by Nozik in 1980 who described the system as 'photochemical diodes' where the two electrodes of a photoelectrochemical cell were combined.[129]

2.6.1 Photochemical reduction of metals on TiO_2 surfaces

The procedure for the photochemical reduction of metals was first studied due to its use in the initial steps of photographic processes using Ag^+ and Pd^{2+} cations.[130] This was followed by the reduction of other metals such as Cu and Rh[120,131] to investigate the kinetics of deposition and the effect of the metals on the photocatalytic activity of the co-catalyst. In general, the photochemical reduction process consists of photocatalytic redox reactions on the TiO_2 surface in the presence of a metal salt precursor and can be summarised in Figure 2.13 below, using the reduction of Pd^{2+} from $PdCl_2$ as a typical example.

The redox reactions on the surface of TiO_2 are initiated by the photogenerated charge carriers that diffuse to the surface of the semiconductor where the metal cations in the

precursor solution are reduced by the electrons, while the holes react with Cl ions and releasing Cl_2.

The nucleation process of the metal nanoparticles is thought to proceed at simultaneous locations via surface states on the semiconductor, followed by the growth of the metal nanoclusters at the nucleation sites. The kinetics of growth, morphology and distribution of the supported metal nanoparticles are not well understood. However, some groups have investigated the mechanisms governing the growth rate of deposited nanoparticles for some metals under specific conditions.[132,133]

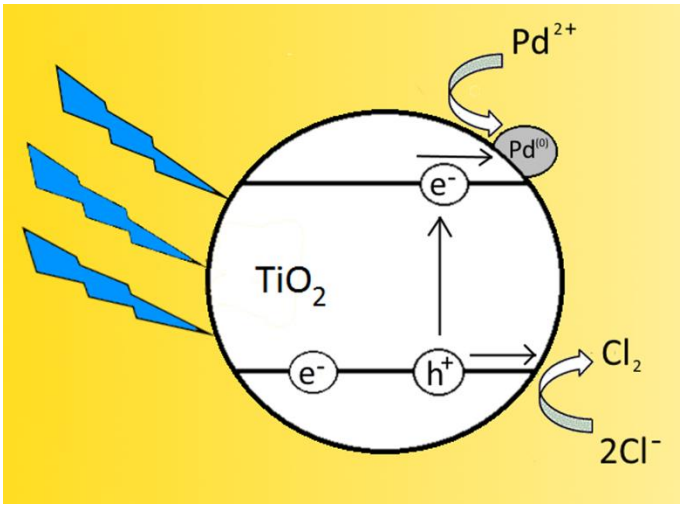

Figure 2.13 The photochemical reduction of Pd^{2+} cations onto a TiO_2 support under UV irradiation

Growth of Pt nanoclusters via the photochemical reduction of a $PtCl_6^{2-}$ precursor was observed by Curran et. al to be limited by the deactivation of the TiO_2 supports due to the saturation of metal deposited on the active surface states.[132] Similarities in morphology was observed for samples prepared at different irradiation times. They proposed a rate limiting mechanism due to the agglomeration of the particles in suspension. The rapid initial deposition rate of Pt on the TiO_2 was thought to correspond to the irradiation of particles on the outer part of the agglomerates, which are subjected

to most of the irradiation. Once Pt deposition on the outer TiO_2 particles has reached saturation, the rate of Pt deposition is then thought to become diffusion-limited, as the active TiO_2 surface states are now located on particles at the inner sections of the agglomerates.

Another study on the kinetics of growth for Pd and Rh nanoparticles suspended in poly(N-vinyl-2-pyrrolidone) (PVP) solutions found that the initial reduction-nucleation of metal nanoparticles was rapid, and their subsequent growth was determined to be a much slower process dominated by Ostwald ripening.[133] It is likely that these processes are not mutually exclusive in the synthesis of metal/TiO_2 co-catalysts via the photochemical reduction procedure but further work is required to determine the kinetics of metal deposition for a broader range of metals.

The improvement in the photocatalytic activity of these modified TiO_2 co-catalysts has been observed to be dependent on the loading of the metal on the TiO_2 surface. Studies on the dehydrogenation of 2-propanol using Ag/TiO_2 photocatalysts found an optimum silver loading of 0.45 wt%.[134] Similarly, optimum metal loading amounts for the production of H_2 from aliphatic alcohols were observed for Pt modified TiO_2[135] and for the photo-oxidation of dye for Pd deposited onto TiO_2.[108] The decrease in photocatalytic activity of the catalyst for high metal loading values were attributed to the blocking of active sites on the TiO_2.[108]

The enhanced efficiency of the metal/TiO_2 heterostructures is thought to arise predominantly from the formation of a thermodynamic energy barrier between the metal and the semiconductor when the two materials make contact. This is known as a

Schottky barrier and this concept can be used to explain some of the mechanisms responsible for the increase in photocatalytic efficiency of these systems.

2.6.2 Schottky barrier formation

When a metal and semiconductor come into contact, a redistribution of electric charge occurs and the Fermi levels of the two materials align until a thermodynamic equilibrium is reached at the metal-semiconductor interface, forming a type of junction. This equilibrium is dependent on the values of the electron affinity of the semiconductor and the work function of the metal, where the CB and VB of the semiconductor bend to reach equilibrium with the Fermi level of the metal.[17] As the materials come into contact, electrons are transferred from the semiconductor to the metal. This migration of electrons results in a net negative charge on the metal surface and a net positive charge at the semiconductor. A space charge layer is thus formed at the point of electrical contact known as the depletion region, since the semiconductor now has an electron deficit in this region. This electron migration away from the junction results in the CB and VB of the semiconductor bending upwards forming a Schottky barrier. The band bending occurs through the space charge layer of the semiconductor and it is the degree of bending that determines the height of the Schottky barrier. This phenomenon is illustrated in Figure 2.14. In the case of the TiO_2, its Fermi level is often higher than the Fermi level of the deposited metals and thus the alignment results in an upward bending. The formation of the Schottky barrier at the metal-support interface is a parameter that indicates whether the metal nanoparticle can efficiently inhibit the recombination of excited carriers by acting as an electron trap site. The barrier height, ϕ_B can be calculated using Equation 2.4:

$$\phi_B = \phi_M - \chi \quad \textbf{(2.3)}$$

where ϕ_M is the work function of the metal and χ is the electron affinity of the supporting material.

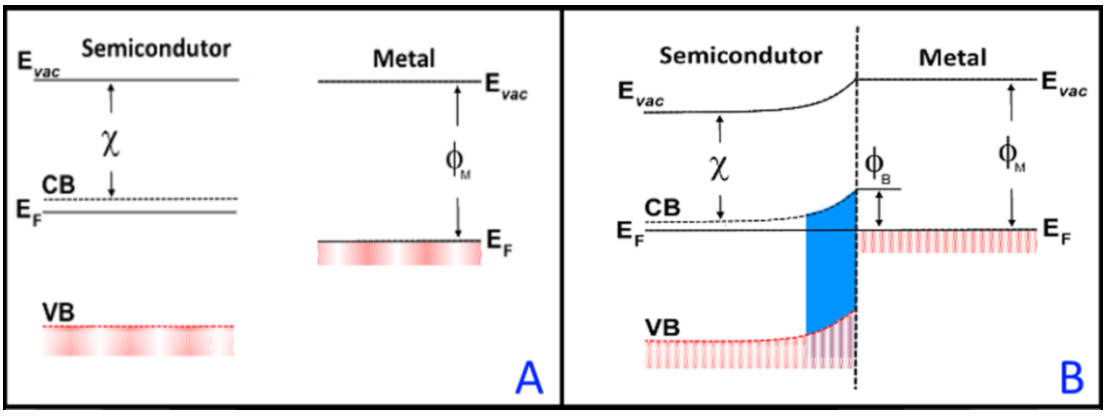

Figure 2.14 The formation of a Schottky barrier at the semiconductor/ metal interface as the materials come into contact with each other. A metal with a Fermi level lower than the semiconductor (A) contact is made between the metal and semiconductor and upward band bending occurs at the interface through the space charge region (B) χ is the electron affinity of the semiconductor, ϕ_B is the barrier height and ϕ_M is the work function of the metal

The migration of electrons from the semiconductor to the metal has been studied for Pt/TiO_2 systems where the process was confirmed via a reduction in the photo-conductance of the co-catalyst compared to TiO_2 only.[135] The trapping of electrons in the metal nanoparticles is an effective prevention of charge recombination and results in the remaining holes in the TiO_2 migrating to the surface to oxidise adsorbed organic species. Furthermore, the presence of the metal can have a profound effect on the photocatalytic properties of the semiconductor due to the redistribution of electron density, affecting the nature of the photocatalytic processes occurring on the surface. The reduction in electron density at the TiO_2 due to electron migration to the metal has been shown to increase the surface hydroxyl group acidity.[136]

It has already been shown that the supported metal nanoparticles can function as electron traps as discussed above. However, it has also been proposed that some metal

oxides can act as hole trap sites, which also prevent the recombination of charge carriers.[137] Uddin et al. synthesised a photocatalyst composed of RuO_2 nanoparticles on TiO_2 powders and suggested that the internal electric field due to the Schottky barrier formed at the RuO_2/TiO_2 interface promoted the transfer of hole to the RuO_2. The increase in the number of hole traps was later confirmed via electron spin resonance (ESR) spectroscopy for RuO_2/TiO_2 photocatalysts compared with unmodified TiO_2.[126]

The formation of a Schottky barrier at the metal-semiconductor interface has been shown to significantly improve the photocatalytic activity of these co-catalyst systems in terms of inhibiting the recombination of the photogenerated charge carriers. Furthermore, the use of some noble metals as co-catalysts improves the photocatalytic efficiency of metal/TiO_2 co-catalysts by taking advantage of another phenomenon known to occur on metallic nanoparticles, this process is called surface plasmon resonance.

2.7 Surface Plasmon Resonance

Surface plasmon resonance (SPR) is the induced collective oscillation of free electrons on the surface of a metal by an electromagnetic wave of appropriate wavelength. The alternating electric field of an electromagnetic wave incident on the surface of a metal displaces weakly bound electrons from their equilibrium positions relative to the crystal lattice, which in turn experience a restoring force due to the positive ions within the lattice. This leads to an oscillation about their relative equilibrium positions; a quantum of which is known as a plasmon. Plasmon resonance is achieved when the frequency of the incident wave is equal to the resonance frequency of the surface electron oscillation.

As the penetration depth of an electromagnetic wave in a metal is approximately 50 nm, only surface electrons have a significant contribution to the plasmon resonance.

SPR can occur in bulk metals, where it is known as a propagating surface plasmon (PSPR), or in metal nanoparticles, where it is manifested as a localised surface plasmon resonance (LSPR). PSPR occurs in an extended length of metal where the propagation of electron density waves causes alternating positive and negative charges along the metal surface due to the plasmonic effect.[138]

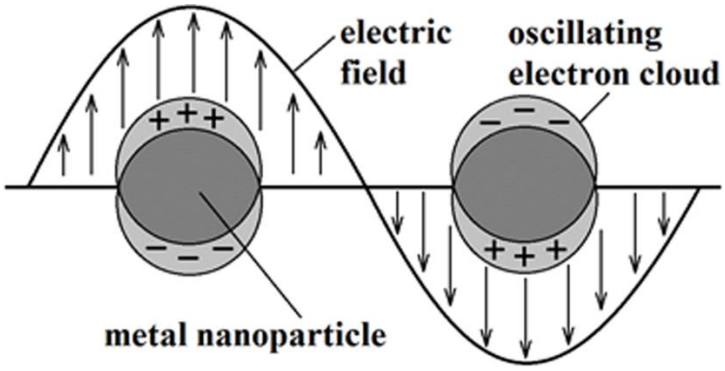

Figure 2.15 The origin of surface plasmon resonance in a metal due to the oscillation of the free electron cloud around a positive ion centre

LSPR is associated with nano-sized metal particles where the oscillation is confined to a finite volume. For a metal nanoparticle, when the wavelength of incident light is larger than the particle itself the electric field across it can be considered uniform, driving the free electrons collectively in one direction creating a dipole. It is the alternating electric field that produces the oscillation of electrons giving rise to a plasmon state. The resonance condition is reached when the frequency of incident light is equal to the plasmon frequency.

The deposition of metal nanoparticles exhibiting LSPR onto supporting structures has been investigated and it was reported that the plasmonic properties of the metals are

highly dependent on the shape and size of the nanoparticles, as well as their local environment.[139]

The most investigated noble metals to date exhibiting the LSPR effect have been Ag and Au.[140–146] Both metals have LSPR peaks in the UV region however, this may be red-shifted to the visible region by reducing the size of the nanoparticles. This is a desirable effect in terms of being able to sensitise TiO_2 photocatalysts to the visible region. Indeed, the increased photocatalytic activity of TiO_2 co-catalysts loaded with Ag or Au nanoparticles in the degradation of organic compounds has been reported both under UV and visible light irradiation.[116,147–150] The improvement in efficiency of these photocatalysts has been attributed to the increased visible light harvesting potential due to the LSPR effect. In the case of Au, it has been shown that plasmonic Au nanoparticles can transfer hot electrons into the TiO_2 under visible light irradiation.[151]

The mechanism is explained via the non-radiative decay of surface plasmons where excited electrons in the Au nanoparticle, having sufficient energy to overcome the Schottky barrier, are transferred to the semiconductor in a mechanism known as resonant energy transfer (RET). This means that photons with energies significantly lower than the band gap of the semiconductor may be absorbed thus increasing the energy harvesting potential of the co-catalyst system, provided that the position of the plasmon peak lies within the visible region. The RET mechanism is shown in Figure 2.16. While the plasmonic effects of Ag and Au nanoparticles have been well documented, these effects have remained more elusive for PGM such as Pt and Pd. This is due to the nature of the shape and intensity of the plasmon peaks of these metals compared to those of Ag and Au. It is known that the position of the plasmon peaks for Pt and Pd lie

in UV region and Langhammer et al. have characterised the plasmonic properties of unsupported Pt and Pd nanostructures ranging in size from 38 nm to 530 nm.[152,153]

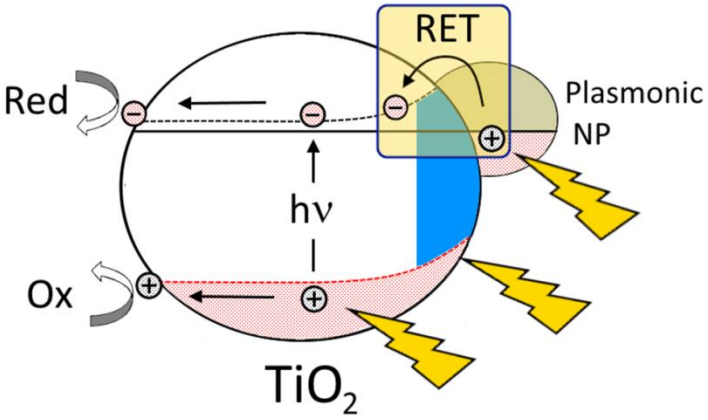

Figure 2.16 The mechanism of RET and hot electron injection form plasmonic metal nanoparticle to the TiO_2 support.

The characteristics of the plasmon peaks for Pt and Pd were notably different from those of Ag and Au in that the shape of the resonance peaks for the PGMs were observed to be much broader compared to Ag or Au. However, they did confirm the observation of tuneable plasmonic properties of Pd and Pt nanostructures similar to that of the other metals.

Another contributing aspect of the noble metal/TiO_2 co-catalyst system that plays a part in the red-shift of the plasmon peak into the visible region is the strong metal-semiconductor interaction (SMSI). Kelly et al. investigated the optical properties of Ag nanoparticles and reported that the position of the plasmon peak for supported Ag nanoparticles shifted up to 100 nm compared with the free standing Ag nanoparticles.[60] Their work adds support to the possibility of tuning the plasmonic properties of other noble metals such as Pt and Pd to be sensitive to visible light irradiation, thus further enhancing the photocatalytic efficiency of noble metal/TiO_2 co-catalysts.

The benefits of these systems would not only be in the reduction of the photogenerated charge carrier recombination rate, but also in improving the light harvesting capability and the rate of photocatalytic reactions via the RET mechanism due to the surface plasmon resonance of the supported metals.

The enhanced properties of noble metal/ TiO_2 co-catalysts have proven particularly useful in increasing the activity of such catalysts in a number of UV and visible light driven applications such as the degradation of organic compounds,[56,79,154–158] water splitting,[29,39,40,142,159–162] antimicrobial applications[46,61–63,163] and hydrogen generation from the reforming of biofuels.[107,121,164–167] The following section will review some of these applications and discuss the current understanding of the photocatalytic mechanisms, along with a general overview of the current state of modified TiO_2 photocatalysts in these applications.

2.8 TiO_2 photocatalysts for the degradation of organic pollutants

One of the most frequent applications of TiO_2 based photocatalysts has been in the degradation of organic compounds, with particular focus being directed at photocatalytic reactions in aqueous environments for water treatment purposes. Initial interest in this area of research was based on the observation by Carey et al. that TiO_2 was capable of oxidising dissolved solutes in aqueous suspensions.[168] Subsequent studies by other groups[131,169–173] reported a number of other oxidation reactions under UV and visible light irradiation of compounds in aqueous TiO_2 suspensions.

The oxidation process is attributed to the generation of highly oxidising radicals on the surface of TiO_2 via the photo-induced redox reactions, which have the potential to destroy the molecular structure of adsorbed species. Modified TiO_2 photocatalysts are

particularly attractive in this application due to their ability to harvest a greater proportion of the incident solar energy and are thus not confined to operation under UV irradiation only. The kinetics for the photocatalytic oxidation (PCO) of pollutants is a highly complex mechanism that can follow several different pathways, each of which is dependent on the nature of the target compound, the physical properties of the photocatalyst and the conditions of the reaction. PCO reactions have been observed to follow Langmuir-Hinshelwood kinetics, suggesting that the reactions take place on the catalyst surface, or in the close vicinity of the photocatalyst, rather than in the solution.[44] The degradation of dyes is widely used as a benchmark for determining the photocatalytic activity of novel photocatalysts. This is because the measurement of the decrease in concentration of dyes can be easily monitored via UV-vis spectroscopy and this can in turn be used as a measure of the activity of the photocatalyst. However, the use of dyes as target compounds has attracted some criticism.[90,174] The main argument against the use of dyes as a measure of photocatalytic activity is that dyes absorb in the visible region and as such, measuring the visible light activity of a new photocatalyst can pose some difficulties when using dyes as the target compounds. This is because the dyes themselves can act as visible light sensitizers in photo-assisted oxidation reactions (PAO) and it is necessary therefore, to carry out further experiments to prove that the enhancement in the photocatalytic activity of any new catalyst is also independent of the PAO process.

2.8.1 General mechanism of degradation of pollutants on TiO_2 catalysts

The initial step for the degradation of organic compounds follows from the generation of a photo-induced electron-hole pair, which migrates to the catalyst surface. Electrons

can reduce the organic compounds or react with surface-adsorbed O_2 and reduce it to a superoxide radical anion, $O_2^{-\bullet}$. Holes can oxidise the organic compounds or react with OH^- or H_2O, oxidising these to $OH^\bullet$ radical species. The generation of these highly reactive radicals, as well as other oxidative species such as peroxide radicals, are reported to be responsible for the degradation of organic compounds by heterogeneous TiO_2 photocatalysts.[155] The different steps of the mechanism are:

$$TiO_2 + h\nu \rightarrow e^- + h^+ \quad \textbf{(2.4)}$$

$$h^+ + H_2O \rightarrow H^+ + OH^\bullet \quad \textbf{(2.5)}$$

$$h^+ + OH^- \rightarrow OH^\bullet \quad \textbf{(2.6)}$$

$$e^- + O_2 \rightarrow O_2^{-\bullet} \quad \textbf{(2.7)}$$

$$O_2^{-\bullet} + H^+ \rightarrow HOO^\bullet \quad \textbf{(2.8)}$$

The reactive radicals can mineralise organic compounds to CO_2 and H_2O. The overall mechanism on TiO_2 photocatalysts can be described by Equation 2.10:

$$\text{Organic pollutant} + TiO_2 + h\nu \rightarrow \text{intermediates} \rightarrow CO_2 + H_2O \quad \textbf{(2.9)}$$

The methods used to measure the degradation of the pollutants depend on the nature of the compound itself. As mentioned previously, the degradation of dye is easily measured via the destruction of the dye chromophore, which can be measured via UV-vis spectroscopy based on the reduction in intensity of the absorption peak of the dye as a function of time. For other compounds such as benzoic acids that do not show absorption in the visible region, the degradation is usually followed via gas chromatography (GC) analysis or mass spectrometry.

The results of photocatalytic degradation reactions are usually presented in terms of the decrease in concentration of the pollutant as a function of time, in the presence of the photocatalyst under UV or visible light irradiation.

Much of the focus of the research in this field has been to improve the response of TiO_2 into the visible region, while increasing its photocatalytic activity in the degradation of the target pollutant. Some of the target compounds widely tested in TiO_2 photocatalysis are presented in Table 2.3.

Table 2.3 Common substrates used in TiO_2 photocatalysis

Substrates		References
Aromatics	Phenol	79,112,175,176
	4-chlorophenol (4-CP)	177–179
	Benzene	180
Organic acids	Acetic acid	94,181–183
	Benzoic acid	84
	Formic acid	169
Dyes	Acid black 1	184,185
	Acid blue 40	47
	Acid orange II	113
	Acid red 3B	48
	Eosin	186
	Rhodamine-B	104,106,187–189
	Methylene blue	190
Alcohols	Methanol	191–193
	Ethanol	194,195
	2-propanol	196,197

In addition to the compounds listed in Table 2.3, Gaya and Abdullah compiled a comprehensive list of organic compounds successfully decomposed by TiO_2 catalysts under UV irradiation.[56] Konstantinou and Albanis also published a summary of a number of dyes that were degraded over TiO_2 photocatalysts under UV and visible light irradiation.[155]

2.8.2 Parameters affecting the degradation of pollutants

The photocatalytic reactions occurring on the surface of photocatalysts remain dependent on a number of factors that determine the kinetic pathways to complete mineralisation of the pollutant. One of the most important parameters affecting the rate of reaction is the available surface area of the catalyst. Since the photocatalytic reactions take place on the surface of the catalysts it is desirable to have the largest surface area possible in order to maximise the number of reactions occurring simultaneously on the catalyst surface.[198] In this sense, nano-sized TiO_2 photocatalysts are more desirable than TiO_2 supported on substrates such as glass, ceramic tiles, etc. However, the drawback of using powders is that they are difficult to separate from the reaction solution. Other parameters that can affect the rate of reaction are the concentration of pollutant, the concentration of catalyst, the pH and the temperature.

The effect of the concentration of the pollutant on the rate of reactions is that at high concentrations the surface of the photocatalyst becomes saturated. Depending on the nature of the target molecules, the catalyst may even be deactivated if the adsorption coefficient is high.[199] The loading of the catalyst is also important as the efficiency of the reaction has been shown to be dependent on the catalyst concentration up to an optimum loading.[200] Beyond this value the reaction rate does not improve and may actually decrease. This is thought to be due to agglomeration of the photocatalyst and increased scattering. The value of the pH of the solution in which the photocatalyst is dispersed was also found to affect the reaction rate.[201] The pH can affect the adsorption of the pollutants to the catalyst surface. The point of zero charge (PZC) of the catalyst surface is determined by the value of pH at which there is no net charge on the catalysts'

surface. At higher or lower levels of pH the catalyst surface will become negatively or positively charged due to the excess of hydroxide anions or protons adsorbed to the surface. This then affects the adsorption coefficient of the pollutants depending whether they are cationic or anionic.

The dependence of temperature on the reaction rate has also been investigated.[56] It was observed that desorption of reactants off the surface of the catalyst and the rate of charge carrier recombination increased with increasing temperature.

It is clear from the body of work focussed on the photocatalytic degradation of pollutants that careful consideration of the nature of the target compound and the conditions of the reaction is necessary in order to use the best combination of materials to synthesise a photocatalyst specific to those conditions.

2.9 Solar H_2 generation with TiO_2 based photocatalysts

2.9.1 Photolysis of water

The generation of hydrogen as source fuel from solar energy has been an intensive field of research in TiO_2 photocatalysis over the last four decades. Photocatalytic H_2 generation is usually carried via the photolysis of water into its constituents or from the reforming of biofuels, such as alcohols or carbohydrates with the primary products being H_2 and CO_2. For the photolysis of water the process can be summarised as given by Equation 2.10:

$$2H_2O \xrightarrow[TiO_2]{hv} 2H_2 + O_2 \qquad \textbf{(2.10)}$$

The reaction shown in Equation 2.11 is really made up of two half reactions where reduction and oxidation occur to form H_2 and O_2, respectively. For overall water splitting the products of the reaction must be only H_2 and O_2 in a stoichiometric ratio of 2:1.

In principle, all semiconductor photocatalysts that can satisfy the following condition should be able to be used for overall water splitting: the lowest edge of the CB must be more negative than the reduction potential of hydrogen generation (H^+/H_2) and the highest edge of the VB must be more positive than the oxidation potential of oxygen (H_2O/O_2). Figure 2.17 illustrates this thermodynamic requirement with the energy bands of TiO_2.

Although there are a number of semiconductors that are theoretically suitable for this reaction, effects such as photo-corrosion can be a problem making them unsuitable in these applications.[3,202] TiO_2 remains one of the most studied photocatalysts in this field but the photo-efficiency of TiO_2 photocatalysts is still relatively low. The problem is that the overall photolysis of water requires an energy input, making it an uphill reaction. The backward reaction where evolved H_2 and O_2 recombine to form water easily proceeds. Methods to evaluate the feasibility of the overall photolysis of water generally make use of sacrificial donors to suppress the backward reaction and measure the evolution of only H_2 or O_2. The sacrificial donors are typically alcohols, which are consumed irreversibly during the reaction.

Relatively high rates of H_2 evolution have been achieved using sacrificial donors for a number of different photocatalyst systems, a comprehensive list of which can be found in a review by Mao et al.[3] Similar challenges are faced by photocatalysts used in these reactions as in the degradation of organic pollutants, such as enhancing the optical response of the photocatalyst and increasing the lifetime of the charge carriers.

As such, similar strategies have been employed when addressing these issues, which are discussed in section 2.5. In addition, there are a number of comprehensive reviews that

discuss more specific, novel approaches to visible light responsive photocatalyst design.[203–206]

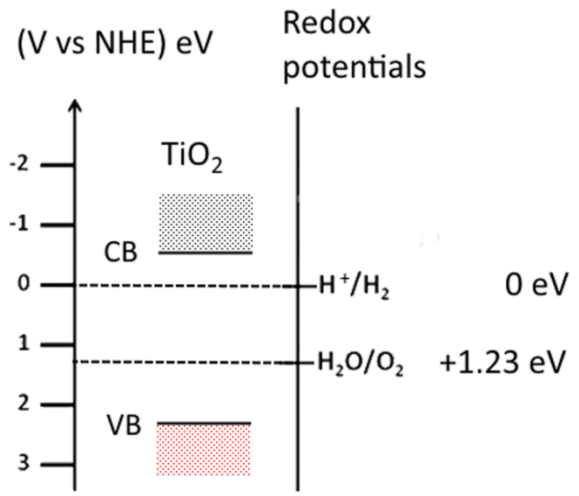

Figure 2.17 Redox potentials of H_2 and O_2 relative to the CB and VB of TiO_2 demonstrating that TiO_2 satisfies the thermodynamic requirement for overall water splitting

It is important to note that the most efficient TiO_2 based photocatalyst in terms of H_2 production has been modified with Pt nanoparticles and was observed to produce stoichiometric amounts of H_2 and O_2 using $NaCO_2$ as a sacrificial donor.[207] However, this was achieved under UV light irradiation only. Other approaches to generating stoichiometric amounts of H_2 and O_2 have depended on spatially separating the oxidation and reduction reactions on the surface of the photocatalyst. The archetypal example of this process is the combination of Pt and RuO_2 nanoparticles deposited onto a TiO_2 support. As Pt is considered to be an electron trap, and RuO_2 facilitates hole transfer,[17] the redox reactions are separated and occur at different metal nanoparticles; reduction occurs on the Pt and oxidation on RuO_2 nanostructures. This process was reported by Gratzel et al.[127] and separately by Kawai and Sakata[5] under visible light irradiation in the presence of sacrificial donors.

More recently, heterojunctions with TiO_2 and other metal oxides such as $BiVO_4$ and IrO_2 have been reported to show excellent photocatalytic water splitting capabilities via improving charge transport mechanisms and increasing the lifetime of photogenerated carriers.[110,111]

2.9.2 Reforming of biofuels

The conversion of biofuels in the presence of a suitable photocatalyst aims to produce H_2 and CO_2 as products under UV or visible irradiation and is an important aspect of sustainable solar fuel production. The most investigated biofuels have been primary and secondary alcohols such as methanol or ethanol[194,208,209] and 2-propanol or butan-2-ol,[166,197] respectively. It has been observed that the nature of the photocatalyst can affect the kinetic pathway of reactions as exemplified by the case of methanol photo-reforming on Au and Pd modified TiO_2 and also RuO_2 modified TiO_2 photocatalysts.[210,211] The generation of H_2 via the water photo-reforming of methanol is possibly the most investigated reaction with respect to the reforming of biofuels since the primary products are H_2 and CO_2 in a stoichiometric ratio of 3:1, Equation 2.11.

$$CH_3OH + H_2O \xrightarrow[TiO_2]{hv} 3H_2 + CO_2 \qquad \textbf{(2.11)}$$

Other alcohols typically produce H_2 and CO_2 also, but intermediate and other primary products with a dependence on longer chain alcohols can affect the rate of H_2 evolution.[166,197] As a result the rate of H_2 production for these alcohols was found to be lower compared with the rate of H_2 production of methanol. The production of H_2 has also been confirmed to be dependent on its concentration.[118]

The production of H_2 via reforming of biofuels is usually carried out via the steam reforming of natural gas.[212] However, high temperatures are required under these

conventional systems making it a very energy intensive process. The ability to photocatalytically produce H_2 under mild operating conditions via the reforming of biofuels presents an attractive alternative.

2.9.3 Conversion efficiency measurement

The solar to hydrogen conversion efficiency (STH) of photocatalysts is often a useful value for comparing the efficiency of photocatalytic systems used in solar harvesting applications. The STH can be calculated using following a method described by Ghosh and Maruska[78] and using Equation 2.12:

$$\mathrm{STH} = \frac{\mathrm{E_{out}}}{\mathrm{E_{in}}} \times 100 \qquad \textbf{(2.12)}$$

where E_{out} is the energy content of the total rate of production of H_2 in kJ/h and E_{in} is the total energy input from the light source incident at the reactor window and also in kJ/h. This equation uses the enthalpy of combustion of H_2, ΔH_c, given as 286 kJ/mol as the energy output of the reaction. This method is a rather simplistic approach to calculating the efficiency of the system as it does not take the actual energetics involved in the conversion of different compounds into their constituents into account. For example, consider the solar production of hydrogen via the photo-reforming of methanol in an aqueous environment, in the presence of a photocatalyst as shown in Equation 2.11. The STH as calculated using the method proposed by Ghosh et al. would use the total energy of the hydrogen produced rather than considering the Gibbs free energy of the formation (ΔG^0) of MeOH and H_2O, since two separate reactions are occurring simultaneously in this instance. It would be therefore be necessary to compute the total energy output of the reaction as the sum of ΔG^0 of H_2 for each of the two mechanisms by considering the mole fraction of each reaction. According to Equation

2.11, the photo-reforming of MeOH in H_2O produces three moles of H_2. Two moles of H_2 can be attributed to the dissociation of MeOH while the remaining mole is attributed to the photolysis of H_2O. The energy output can then be calculated using the mole fraction of the volume of H_2 production by the MeOH, in this case 0.67, and multiplying by ΔG^0 of MeOH to give the energy associated with this reaction and adding this to the energy associated with the photolysis of water reaction, which is given by the mole fraction of the volume of H_2 produced (0.33) and multiplying by ΔG^0 of H_2O. The sum of these two reactions gives the amount of energy required to produce the amount of H_2 measured over the period of the reaction. Therefore, the E_{out} can be taken as the sum of the mole fractions of the Gibbs free energy of formation of MeOH and H_2O, rather than ΔH_c of H_2, to give a more accurate representation of the STH. In this respect, one can also take the value of E_{in} as the percentage of energy absorbed through the solution in the reactor rather than the total amount incident on the reactor window. Measuring the E_{in} using this method, gives a more accurate representation of the efficiency of the system in terms of the energy absorbed by the catalyst.

Research into the photocatalytic reforming of biofuels, is still in its infancy compared with the photolysis of water. Most photocatalysts investigated are TiO_2 based systems modified with single noble metals, although the use of bimetallic Au -Pd supported on TiO_2, as well as Pt-Ru on TiO_2 have also been reported.[210,213] The photolysis of water in the presence of sacrificial reagents can perhaps be viewed, for the case of methanol at least and at these small scales, as a photo-reforming reaction. In this respect, it can be assumed that many of the photocatalysts prepared for the photolysis of water would be also suitable for the photo-reforming of biofuels. As such, many of the strategies applied

to improve the performance of the photocatalysts in the photolysis of water are applicable. However, regarding the reforming of biofuels other than methanol, an investigation into the selectivity of the photocatalyst toward the target molecule is necessary to ensure complete mineralisation.

This review of the literature will have familiarised the reader with current trends in TiO_2 photocatalysis, emphasising it's applications in the degradation of pollutants for water purification and generation of H_2 as a sustainable fuel source under solar light irradiation.

3 Experimental Methods

3.1 Irradiation sources

3.1.1 UV lamp

The photo-reductive deposition of metal nanoparticles was carried out using a Honlé UVACube 100 compact UV radiation unit. The working dimensions inside the unit are 180 mm x 180 mm x 180 mm surrounded by a casing of aluminium with uniform irradiation of approximately +/- 10% at the base of the chamber. Samples were irradiated inside the chamber and the light source was operated via a manual shutter located on the side of the unit. A mercury bulb was used for all experiments. The wavelength of radiation emitted was approximately 350 nm – 750 nm and the output is shown in Figure 3.1.

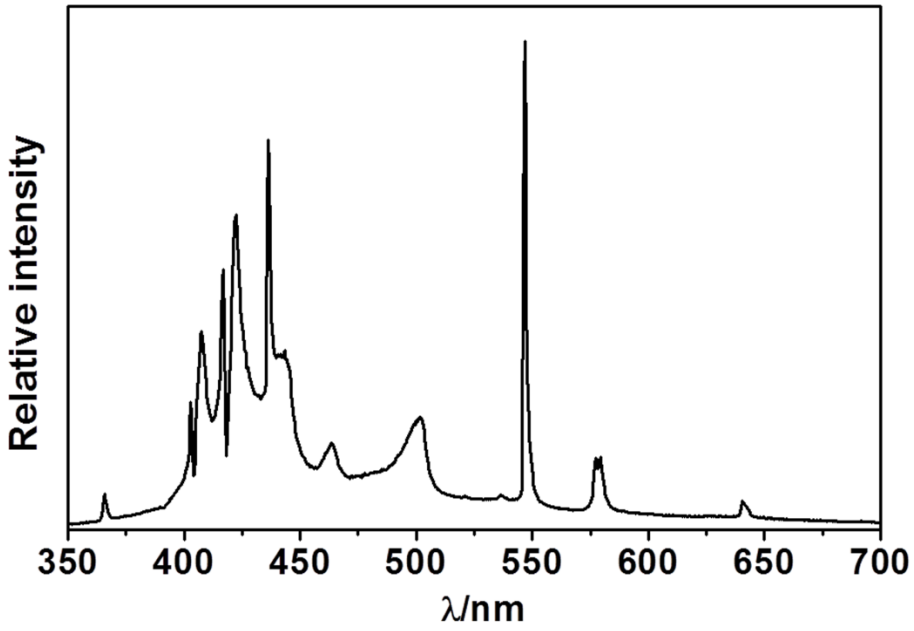

Figure 3.1 Spectral output of the UVACube lamp used for the photochemical deposition of metals

The samples were irradiated for different periods of time at different distances from the source corresponding to irradiance values of 9.54 mW/cm^2 at a distance of 2.2 cm and 2.05 mW/cm^2 at a distance of 18.5 cm.

The irradiance output of the UVAcube was measured using an International Light Technologies ILT1400 radiometer/photometer over a range of different distances inside the irradiation chamber. The measured values presented in Table 3.1 were plotted on a graph (Figure 3.2) where the relation between the irradiance and the distance from the source is approximately a power law.

Table 3.1 Irradiance measurements as a function of distance from UV source

Distance from source/ cm	Irradiance/ mW/cm^2
18.80	2.06
17.45	2.15
16.10	2.25
14.75	2.36
13.40	2.42
12.05	2.65
10.70	2.92
9.35	3.38
8.00	3.90
6.65	4.75
5.30	5.72
3.95	7.14
2.60	9.01
1.25	11.60

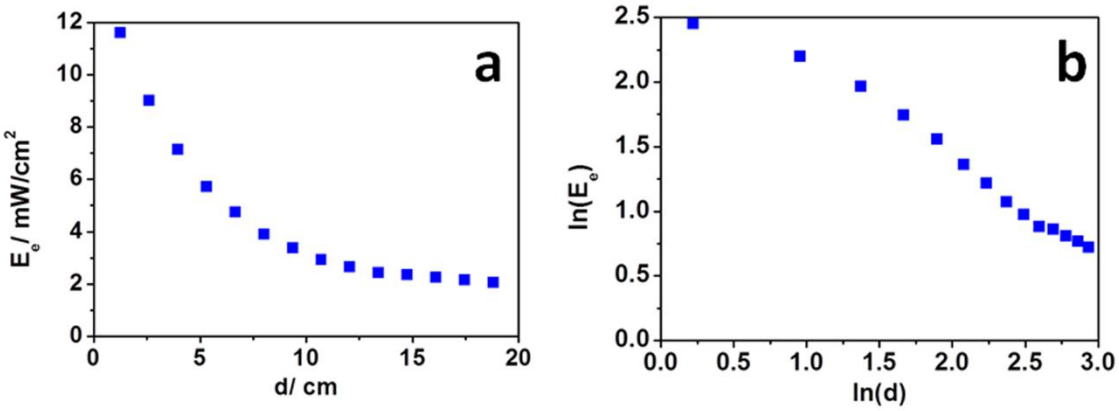

Figure 3.2 a) Output of the UV cube in terms of irradiance as a function of distance from the UV source and b) natural logarithm of the irradiance versus distance.

The irradiance value at any given distance from the source inside the irradiation chamber was calculated using a power law of the form:

$$E_e = kd^{-m} \quad \textbf{(3.1)}$$

where E_e is the irradiance value, d is the distance from the light source and k and m are constants. Figure 3.2 shows that the power law given in Equation 3.1 gives the best fit between the irradiance and the distance from the source. Also, Figure 3.2b indicates that the values of k and m change over sections of the graph and cannot strictly be considered as constants. Taking this into account, new values of k and m were obtained for each new calculation of the irradiance associated with a given distance from source. The constants were calculated by taking the natural logarithm of Equation 3.1 and rearranging to give:

$$\ln(k) = \ln(E_e) + m\ln(d) \quad \textbf{(3.2)}$$

The value of m was calculated by assuming it to be the gradient of a straight line passing through a known value of d. For instance, to find the irradiance at distance of 2.2 cm, the values of d and E_e from Table 3.1 were chosen such that x = 2.2 cm lies between the chosen d values. An example calculation of the unknown E_e value (for the irradiance at a known distance of 2.2 cm) is given below. First, the gradient of the straight line passing through d = 2.2 cm as shown in Equation 3.3:

$$m = -\frac{\ln E_{e2} - \ln E_{e1}}{\ln d_2 - \ln d_1} = -\frac{\ln 11.60 - \ln 9.01}{\ln 1.25 - \ln 2.60} = 0.345 \text{ mW/cm}^3 \quad \textbf{(3.3)}$$

The value of ln(k) is then calculated from Equation 3.2 by using m obtained from Equation 3.3. The values of E_e and d used in Equation 3.2 are the values of the midpoint between E_{e1} and E_{e2}, and d_1 and d_2 giving:

$$\ln(k) = \left(\frac{\ln(11.60) - \ln(9.01)}{2}\right) + 0.345\left(\frac{\ln(2.60) - \ln(1.25)}{2}\right) = 2.53 \quad \textbf{(3.4)}$$

The k value is then calculated by taking the exponent of ln(k) to give k = 12.53. Finally, E_e at d = 2.2 cm is calculated by using the values of m and k obtained from Equation 3.3 and Equation 3.4, respectively such that:

$$E_e = kd^{-m} = 12.53 \times 2.2^{-0.35} = 9.54 \text{ mW/cm}^2 \quad \textbf{(3.5)}$$

The values given in Table 3.1 were also used in similar calculations to approximate the irradiance at 18.5 cm from the source which was calculated to be 2.05 mW/cm^2.

3.1.2 Solar simulator

The irradiation of samples under simulated sunlight was carried out using a 300 W Newport solar simulator fitted with a Xe arc lamp and an AM 1.5G filter, with a collimated beam area of 50 mm x 50 mm. The spectrum of the lamp was measured to

be between 300 nm – 900 nm as shown in Figure 3.3 and have a working output of 1.00 Sun, corresponding to an irradiance value of 100 mW/cm^2.

The output of the solar simulator was measured using a Si reference solar cell (Oriel, P/N 91150V), where the reference cell was placed a distance equal to the distance from the light source to the top of the reaction vessel and the output measured. The irradiance value at the bottom of the reaction vessel was not measured since the incoming light would be partially absorbed by the photocatalyst and the target compound.

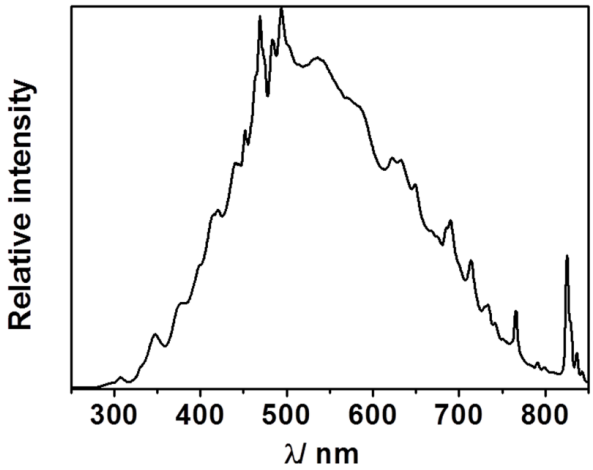

Figure 3.3 Spectral output of the Newport solar simulator fitted with AM 1.5 filter used for photocatalytic reactions

3.2 Solar to hydrogen conversion efficiency calculations

The solar to hydrogen conversion efficiency (STH) of the photocatalysts was calculated using Equation 2.12 where E_{out} is the sum of the energy content of the production of H_2 in kJ/h in terms of the Gibbs free energy of formation of MeOH and H_2O, and E_{in} is the energy input from the solar simulator as a function of the percentage of energy absorbed by the photocatalyst through the solution, also in kJ/h.

First, the value of E_{in} was taken as a percentage of the total output of the solar simulator incident over surface area of the bottom of the reaction vessel per hour, where the surface area was calculated to be:

$$S_A = \pi\left(\frac{d}{2}\right)^2 = \pi\left(\frac{4.5cm}{2}\right)^2 = 15.9cm^2 \quad \textbf{(3.6)}$$

The power incident at the reaction vessel was calculated using the irradiance value of the solar simulator (I_s) at 100 mW/cm^2 such that the power input was calculated to be:

$$P = I_s \times S_A = 100mW/cm^2 \times 15.9cm^2 \approx 1.6W \quad \textbf{(3.7)}$$

The power calculated using Equation 3.8 gives the power input of the solar simulator per second. This value was converted to give the output in terms of kJ/h using Equation 3.9:

$$E_{in} = Pt = 1.6W \times 3600s = 5.76kJ \quad \textbf{(3.8)}$$

where E_{in} is the energy incident at the reactor value in joules (kJ), P is the power output of the solar simulator in watts (W) and t is the time in seconds (s). To determine the percentage of energy absorbed by the catalyst, the spectra of the incident light was measured in the absence and presence of the catalyst in the reactor.

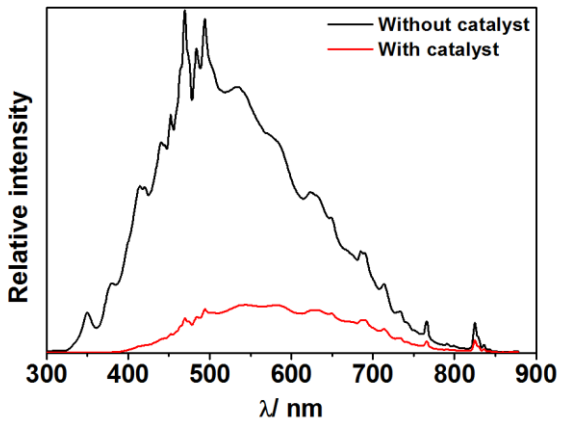

Figure 3.4 Absorption of light through the reactor measured via USB spectroscope at the bottom of the reaction vessel

The area under each of the curves was calculated using the integration function in the Originlab software and the percentage of energy absorbed determined using these values. The percentage of absorption was calculated to be 82.6%, where E_{in} was then adjusted to a value of 4.74 kJ/h. This was fixed for all the experiments conducted and no losses were assumed between the light source and the top of the reactor.

The E_{out} value was taken as the sum of the mole fractions of ΔG^0 of MeOH and H_2O relative to the average volume of H_2 generated by the catalyst per hour in moles as shown in Equation 3.9:

$$E_{out} = (0.67 \times V_{H_2} \times \Delta G^0_{MeOH}) + (0.33 \times V_{H_2} \times \Delta G^0_{H_2O}) \quad \textbf{(3.9)}$$

where V_H is the average volume of H_2 per hour converted to moles, ΔG^0_{MeOH} is 166.6 kJ/mol and ΔG^0_{H2O} is 237.1 kJ/mol. Equation 3.9 can be simplified to:

$$E_{out} = \frac{V_{H_2}}{3}\left[2\Delta G^0_{MeOH} + \Delta G^0_{H_2O}\right] \quad \textbf{(3.10)}$$

3.3 Preparation of the metal salt solutions

The palladium chloride ($PdCl_2$) stock solution was prepared by dissolving either (177.33 ± 0.50) mg or (354.65 ± 0.50) mg of $PdCl_2$ powder (Sigma, ≥ 99.9%) in 100 mL of an 0.01 M hydrogen chloride (HCl) solution to give $PdCl_2$ concentrations of 0.01 M or 0.02 M, respectively. $PdCl_2$ is poorly soluble in water and HCl must be added to facilitate the complete dissolution of the powder. First the powder and solution mixture was sonicated in a sonic bath for 30 min to deaggregate the powder and then the solution was placed on a hot plate and stirred at 300 rpm at 80 °C until the $PdCl_2$ was completely dissolved.

For the ruthenium chloride ($RuCl_3$) solution, a 0.01 M solution was prepared by dissolving (207.43 ± 0.50) mg of the powder ($RuCl_3 \cdot xH_2O$ Sigma, Reagent Plus) in 100 mL of deionised water on a stirring plate. The solution was then diluted to a final concentration of 0.001 M $RuCl_3$, which was used as the source of Ru ions for the photodeposition procedure. A concentration of 0.01 M was not used for the Ru photodeposition because the solution at 0.01 M was very dark and it was thought that this would prevent the effective absorption of irradiation by the TiO_2 and impede photoreduction.

3.4 Photochemical reduction

In a typical photoreduction procedure 10 mL of the prepared $PdCl_2$ or $RuCl_3$ solution and 1 g of TiO_2 powder (Aeroxide P25, Sigma Aldrich) were mixed in a glass reaction vessel; a 50 mm diameter (10 mm deep) glass petri dish containing a magnetic stir bar and sealed with a 50 mm x 50 mm x 1 mm quartz lid to minimise evaporation during the procedure. The contents inside the reactor were then stirred at 300 rpm under UV irradiation (UVAcube). The length of irradiation time varied for each synthesis but four values were used and repeated for each of the photoreduction conditions. Two different irradiance values were used throughout the syntheses; 9.54 mW/cm^2 and 2.05 mW/cm^2. A stirring platform was employed to achieve the higher value whilst maintaining the stirring of the contents inside the reaction vessel.

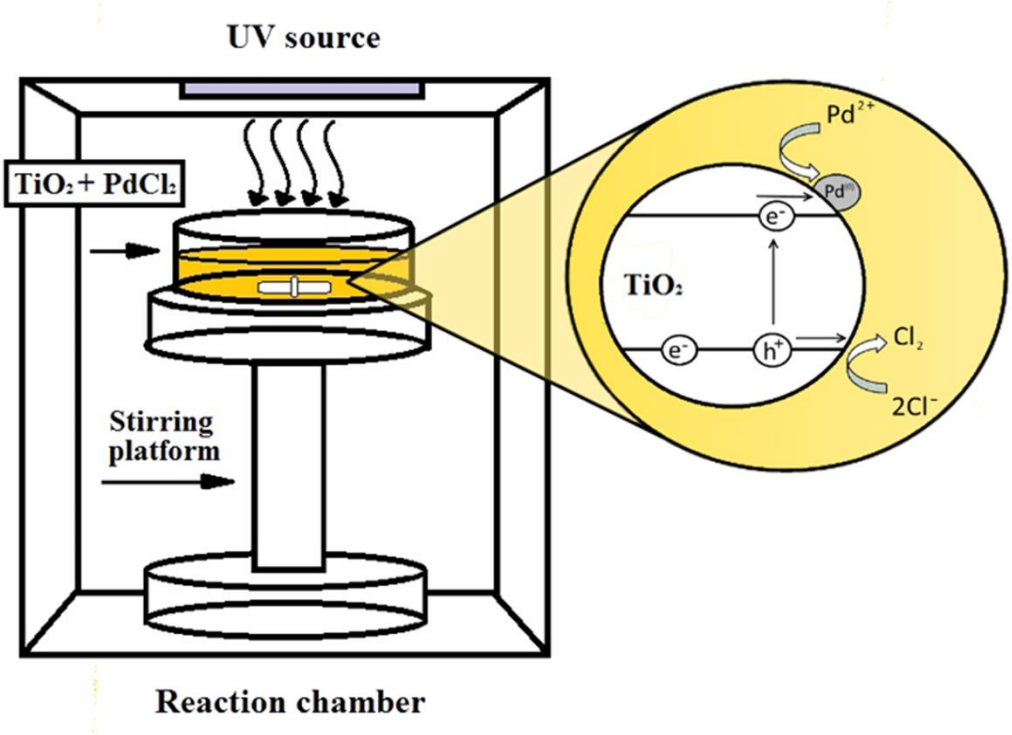

Figure 3.5 Schematic of photochemical deposition procedure

To achieve the irradiance value of 2.05 mW/cm^2, the reaction vessel was placed directly onto the stirring plate. After irradiation, the mixture was transferred to a centrifuge tube and centrifuged at 4000 rpm for 30 min to separate the powder from the solution. The metal salt solution was retained for ICP analysis in order to determine the concentration of metal ions present in the solution. By comparing this value with the concentration metal ions present in the stock solution, the amount of metal photochemically deposited onto the TiO_2 was calculated.

The powder was then washed with deionised water several times until the supernatant was clear and colourless.

The catalyst was then separated from the solution and dried at 27 °C. Once dry the powder was crushed using a mortar and pestle to de-aggregate the sample, and this was then ready for characterisation and testing.

3.4.1 Thermal treatment of Ru:TiO_2 photocatalyst

Subsequent to the photochemical reduction of Ru onto TiO_2, and the washing of the prepared catalyst, the sample was then further subjected to a thermal treatment. The Ru:TiO_2 was placed in an Al_2O_3 crucible and heated in air at 450 °C for 5 hours. This was done to oxidise the Ru nanoparticles to RuO_2.

3.5 Characterisation of photocatalysts

3.5.1 Transmission electron microscopy (TEM)

The size, distribution and morphology of the photodeposited nanoparticles was determined using a Jeol 2010 microscope operating at an accelerating voltage of 200 kV. The powdered samples were prepared by ultrasonic dispersion in ethanol. This solution was then added drop-wise onto a 200 mesh holey carbon copper grid for analysis. The average size of the nanoparticles was measured from the obtained images using the ImageJ software.

3.5.2 Ultraviolet/ visible spectrophotometry (UV-vis)

Absorbance and diffuse reflectance (DR) analyses were carried out using a PerkinElmer Lambda 950 UV-vis spectrophotometer. The change in the absorbance of dye from photodecolourisation experiments was monitored using the transmission module scanning at wavelengths from 400 nm – 600 nm. The volume of solution used for each analysis was 1 mL contained in polystyrene cuvettes with a 10 mm window and a spectral range of 340 nm – 800 nm.

The absorption of light by the dye is directly proportional to its concentration in solution, according to the Beer-Lambert law. Using this concept, the change in relative absorbance can be related to the change in concentration of the dye, which allows for a quantitative analysis of the photodecolourisation process.

The change in the optical response of the photocatalysts was investigated via DR measurements using 50 mg of each catalyst in the sample holder containing a potassium bromide (KBr) window and scanning at wavelengths from 300 nm – 700 nm. The measured DR values were converted to and expressed as absorbance values automatically via the Kubelka-Munk function in the PerkinElmer UV-vis software package.

3.5.3 Inductively coupled plasm- atomic absorption spectroscopy (ICP)

The concentration of metal ions in the initial stock solutions and in the recovered metal salt solutions after photodeposition was analysed using a Spectra AA 220FS ICP unit. Prior to ICP analysis, the solutions were first diluted 100 times to conform to the detection limits of the machine. This was done by preparing a solution containing 10 µL of the recovered metal salt solution in 10 mL of a 0.01 M aqueous solution of HCl to prevent precipitation of the Pd nanoparticles. The concentration of metal, measured in mg/L deposited onto the TiO_2 substrate, was calculated as the difference between the concentration of the stock solution and the concentration of the solution after UV irradiation according to Equation 3.11.

$$C_0 - C_{MS} = C_f \quad \textbf{(3.11)}$$

C_0 is the measured concentration of the initial stock solution, C_{MS} is the measured concentration of the solution recovered after irradiation and C_f is the difference in concentration and is equal to the concentration of deposited metal. The weight percentage of metal nanoparticles was calculated using Equation 3.12 where the number 1000 is the mass of the substrate in milligrams.

$$\text{wt}\% = \left({}^{C_f}\!/_{1000} \right) \times 100 \quad \textbf{(3.12)}$$

3.5.4 X-ray diffraction (XRD)

The analysis of the crystal phase of the substrate and of the deposited nanoparticles was conducted via XRD at the X-ray diffraction facility using a Panalytical Xpert Pro diffractometer.

3.5.5 X-ray photoelectron spectroscopy (XPS)

The oxidation state of the photodeposited metal nanoparticles was determined via XPS analysis at the NEXUS facility, University of Newcastle using a Thermo Scientific K-Alpha XPS unit. The binding energy values of Pd were obtained by referencing the Cs1 peak for each measurement using the CasaXPS software and taking the value of the peaks for the $3d_{3/2}$ and $3d_{5/2}$ spin orbits for Pd. The chemical state of Ru could only be ascertained via the $3d_{5/2}$ spin orbit component because the $3d_{3/2}$ component could not be observed due to the overlap with the adventitious carbon C1s peak.

3.5.6 Gas chromatography

Gas samples were analysed using an SRI 310 gas chromatography (GC) unit fitted with a thermal conductivity detector (TCD) and using N_2 as the carrier gas. The analysis of gases was conducted using the PeakSimple software version 4.35. The flow rate was set at 10 mL/min and 0.1 mL volume samples were manually directly injected into the column.

For the analysis of H_2 and O_2 an MS 5A 1 m column was used at an oven temperature of 50°C. The analysis of H_2 and CO_2 was carried out using a 1 metre silica gel packed column at an oven temperature of 80°C. The silica gel column did not provide sufficient resolution for the H_2 and O_2 peaks and thus the MS 5A column was used when analysing for O_2 and H_2.

Column conditioning was carried out each time the columns were swapped out to remove traces of O_2 or other gases that may have leached in whilst being stored. The columns were condition by running the GC from 110°C to 290°C, ramping at 5°C per min. The GC was maintained at 290°C for 180 min to complete the conditioning process.

The H_2, O_2 and CO_2 peaks were identified at the operating conditions using a calibration standard where the concentration of each gas was 1 mol%. The calibration standard was used as a reference with which to calibrate the instrument using pure H_2 and O_2. The height of the H_2 peaks was measured 3 times for 5 different concentration levels of pure H_2 to obtain an average value for each concentration. These values were then normalised to the known calibration standard concentrations and used to plot a calibration curve saved into the software program (Details of the calibration procedure can be found in Appendix A).

3.6 Photocatalytic activity measurements

3.6.1 Aqueous dye solution preparation

A concentrated stock solution of dye was prepared by dissolving 10 mg of dye powder in 1 mL of H_2O to produce a solution with a concentration of 10,000 ppm. Each dye degradation experiment used a standard concentration of dye solution of 10 ppm by diluting an appropriate amount of the stock solution in H_2O. In a typical test, 50 μL of

the concentrated stock solution would be diluted in 50 mL of H_2O. The mixture was then stirred vigorously to ensure complete dissolution of the dye particulates.

Tests carried out to investigate the effect of the change in the concentration of dye on the photocatalytic activity of the catalyst used the same preparation method for the stock solution but with initial dye concentrations of 20 ppm, 30 ppm, 40 ppm and 50 ppm. This was achieved by diluting a larger volume of stock solution in H_2O to produce the more concentrated dye solutions.

3.6.2 Dye adsorption/ desorption equilibrium reactions

As the dye molecules come into contact with the photocatalyst, the molecules adsorb to and desorb from the surface of the catalyst until an equilibrium is established. The amount of adsorption of dye to the powdered photocatalyst surface prior to irradation was monitored by comparing the concentration of dye before the introduction of the catalyst to the concentration of dye 30 min after introducing the catalyst. Typically, a 10 ppm dye solution was prepared and an aliquot was taken before addition of the photocatalyst to the reaction vessel to measure the initial value of dye concentration. The slurry was then magnetically stirred for 30 min under dark conditions after which time another aliquot was taken. This sample was centrifuged at 4000 rpm for 30 min to remove any photocatalyst particulates. The collected dye sample was then analysed using UV-vis to measure the change in the peak absorption wavelength (λ_{peak}) of the dye corresponding to a change in concentration. The percentage of dye adsorption was calculated according to Equation 3.13.

$$(1 - C/C_o) \times 100 = \%\text{adsorption} \quad \textbf{(3.13)}$$

where C_0 is the initial concentration of dye before the addition of the catalyst and C is the concentration of dye after 30 min of stirring in the dark.

3.6.3 Dye decolourisation reactions

A standard procedure for the photodecolourisation of dye was established to compare the photocatalytic activity of the synthesised catalysts. The standard procedure used 50 ml of dye solution at a catalyst loading of 2 g/L at the natural pH of the solution. The solution was irradiated under simulated sunlight and 1.5 mL aliquots were taken at 1 min intervals for the duration of the reaction. Aliquots were then centrifuged twice at 4000 rpm for 30 min to remove the photocatalyst before measuring the change in λ_{peak} of the dye via UV-vis analysis. The activity of the photocatalyst was measured in terms of the half-life of decolourisation of dye.

The change in concentration of dye over time was measured by analysing aliquots via UV-vis spectroscopy and using the Beer-Lambert law relating the absorbance measurement to the concentration of dye at its peak absorption value. In the case of RhB, the peak absorption value, λ_{max}, is 554 nm as shown in Figure 3.5.

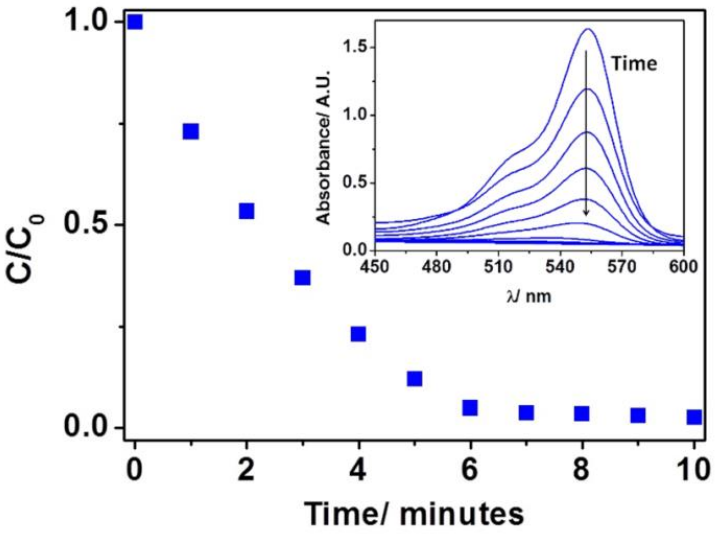

Figure 3.6 Photodecolourisation profile of dye represented by the decrease in normalised absorbance over time

The initial concentration of dye for each experiment was taken as the absorbance value obtained after 30 min of stirring the prepared catalyst and dye solution in the dark to allow for the adsorption/desorption equilibrium.

The decrease in initial dye concentration time, as obtained via UV-vis measurements, was used to calculate the rate of reaction and half-life of dye decolourisation values ($t_{1/2}$). The reaction mechanism is generally accepted to follow Langmuir-Hinshelwood (L-H) kinetics,[21,214] which is commonly used in heterogeneous catalysis to model the degradation of organic compounds in aqueous solutions and is given by Equation 3.14:

$$r = -\frac{dC}{dt} = \frac{k_r K_a C}{1 + K_a C} \quad \textbf{(3.14)}$$

where r is the reaction rate, C is the concentration of dye, k_r is the reaction rate constant and K_a is the adsorption/desorption equilibrium constant. Typically, the concentrations used in photocatalytic experiments are considered to be low where the value $K_aC << 1$ and k_rK_a can be taken as an apparent rate constant, k_{app} (min^{-1}). Equation 3.15 can therefore be simplified to:

$$-\frac{dC}{dt} = k_{app} C \quad \textbf{(3.15)}$$

The degradation of dye is assumed to follow pseudo-first order kinetics and the apparent rate constants for all experiments were calculated using Equation 3.16:

$$\ln \frac{C_0}{C} = k_{app} t \quad \textbf{(3.16)}$$

where C_0 is the initial concentration of the dye and C is its concentration at time t. Equation 3.16 can be viewed as the equation of a straight line where $\ln(C_0/C) = y$, $t = x$

and k_{app} = m. This was how the rate constants for all catalysts were calculated. The $t_{1/2}$ values were calculated in terms k_{app} according to exponential decay using Equation 3.17:

$$C = C_0 e^{(-k_{app}t)} \quad \textbf{(3.17)}$$

Exponential decay can also be expressed using two other equivalent equations in terms of the mean lifetime of the substance, τ and also the half-life. These are necessary to relate the $t_{1/2}$ to the rate constant and simplify the calculation of the $t_{1/2}$ values. The equivalent expressions are given in Equation 3.18:

$$C_0 e^{(-k_{app}t)} \equiv C_0 e^{\frac{-t}{\tau}} \equiv C_0 \left(\frac{1}{2}\right)^{\frac{t}{t_{1/2}}} \quad \textbf{(3.18)}$$

Cancelling the factor of C_0 and taking natural logarithm gives:

$$-k_{app}t \equiv -\frac{t}{\tau} \equiv \frac{t}{t_{1/2}} \ln\left(\frac{1}{2}\right) \quad \textbf{(3.19)}$$

Now cancelling the factor of t and since ln(1/2) = -ln(2), Equation 3.19 becomes:

$$-k_{app} \equiv -\frac{1}{\tau} \equiv -\frac{1}{t_{1/2}} \ln(2) \quad \textbf{(3.20)}$$

Cancelling the negative factor, dividing through by ln(2) and rearranging gives:

$$t_{1/2} \equiv \tau \ln(2) \equiv \frac{\ln(2)}{k_{app}} \quad \textbf{(3.21)}$$

Equation 3.21 was used to calculate the $t_{1/2}$ values in terms of the k_{app} value for all the synthesised catalysts. These values were used as the key parameters in determining and comparing the photocatalytic activity of the Pd:TiO_2 catalysts, depending on the synthesis procedure and under different experimental conditions.

3.7 Photocatalytic hydrogen generation

3.7.1 MeOH reforming reactions

For the generation of H_2, a standard procedure was established to compare the activity of the photocatalysts in terms of evolution of gas. Methanol (MeOH) was used as the electron donating species. Each standard reaction was prepared with 100 mL of an aqueous solution containing 20% MeOH at a catalyst loading of 0.33 g/L. The solution and photocatalyst were inserted into a glass reaction vessel fitted with a gas tight quartz lid for top down irradiation. The reaction vessel was purged with N_2 through the solution for 30 min in the dark to remove any dissolved O_2. The reaction vessel was then placed in a circulating water bath and an inverted burette was used to measure the volume expansion of gases over time via water displacement. The inverted burette was positioned in a container filled with H_2O where a pipe from the reaction vessel was inserted into the submerged opening of the burette as shown in Figure 3.6. This method allowed for the direct measurement of the total volume of gas evolved during irradiation.

The evolution of gases was monitored on an hourly basis by measuring the volume increase of gas collected inside the inverted burette. Gas samples from inside the reaction vessel were analysed via gas chromatography on an offline GC unit to determine the composition of evolved gases inside the vessel.

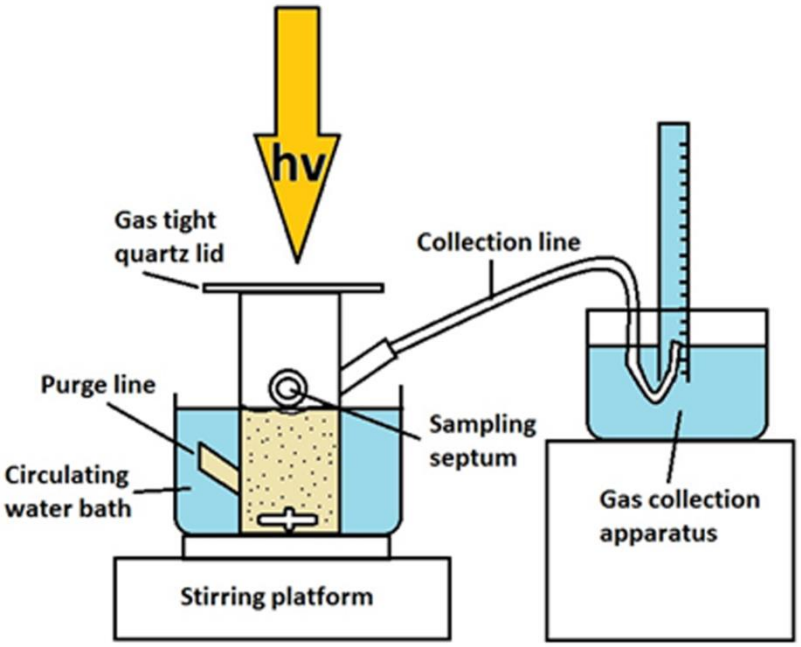

Figure 3.7 Schematic of the experimental apparatus for the hydrogen generation tests

4 Photocatalyst synthesis and optimisation

The ability to tune the optical properties of the photocatalyst based on the modification of certain aspects of the synthesis procedure was investigated. This chapter discusses the synthesis and optimisation of the surface modified TiO_2 catalyst in terms of its physical properties and resultant photocatalytic activity in the degradation of rhodamine b (RhB) dye. The effect of the intensity and length of UV irradiation, as well as the concentration of the metal salt solution on the physical characteristics of the photochemically deposited nanoparticles was examined in order to improve the optical response and photocatalytic efficiency of the photocatalyst.

4.1 Photocatalyst synthesis

An experimental method designed to serve as a standard operating procedure for the photochemical deposition of metal nanoparticles on TiO_2 is described in section 3.4 where certain parameters could be manipulated. The method was intended to take the fewest steps of preparation while producing an efficient and stable photocatalyst. $PdCl_2$ was used as the source of metal ions for Pd photoreduction.

Four parameters were selected to be altered during the photochemical reduction procedure. These were: the concentration of metal in solution; the volume of the solution; the irradiance value and the length of irradiation time. Based on these four parameters, six different experimental conditions were established and organised into 3 groups. Each group contained two sets of differing parameters and a total of 8 catalysts as shown in Table 4.1. Four catalysts were synthesised per set corresponding to four different lengths of UV irradiation time. A total of 24 catalysts were prepared for this study.

Table 4.1 Catalyst matrix showing the changes applied to the parameters in question

	Group 1		Group 2		Group 3	
Set	1	2	1	2	1	2
$PdCl_2$ concentration/ mol/L	0.01	0.01	0.02	0.02	0.02	0.02
Solution volume/ mL	10	10	5	5	10	10
Irradiance value/ mW/cm^2	2.05	9.54	9.54	2.05	9.54	2.05

4.1.1 Effect of metal salt concentration

The concentration of the $PdCl_2$ solutions were altered to establish how this affected the amount of Pd photochemically reduced onto the TiO_2 and the effects on the activity of the catalyst. The concentration values of the metal precursors were chosen for the investigation based on the photochemical reduction of Al described elsewhere.[215] Other precursor concentration values were also prepared and tested but the photocatalytic activity of those resultant catalysts was not significantly improved. Briefly, a 10 fold increase in the concentration of $PdCl_2$ did not increase the activity of the catalyst, while a 10 fold decrease in concentration reduced the activity considerably. Therefore, the two values of 0.01 M and 0.02 M were chosen for the optimisation investigation.

4.1.2 Effect of solution volume

The volume of the metal salt solution was also subject to a change but only at a concentration of 0.02 M. The volume was reduced by half, corresponding to the same amount of Pd present in the 0.01 M solutions at 10 mL. This was done to try and minimise the volume of solution used during the procedure and it was found that a further reduction in volume was not suitable due to the amount of TiO_2 powder used. At 1 g of TiO_2, any further reduction in the solution volume resulted in a very viscous mixture in the reaction vessel that made it difficult to stir effectively during irradiation.

4.1.3 Effect of irradiance value

The irradiance values established for the photoreduction were limited to the maximum and minimum values of the irradiation source, which corresponded to the largest and smallest distance between the light source and the top of the reaction vessel. Intermediate irradiance values were not easy to obtain since the output of the UV lamp was fixed and the only method to alter the irradiance was by changing the distance. The geometry of the irradiation chamber also made the practicality of maintaining the solution stirring during the photoreduction procedure a problematic task. To solve the problem of stirring the solution at the maximum irradiance value, an improvised stirring platform was constructed to raise the reaction vessel as close to the UV source as possible.

4.1.4 Comparison of synthesis on photocatalytic activity

Having established the sets of experimental parameters to vary it was possible to investigate the effect of the changes in each of these factors on the physical properties of the deposited nanoparticles through a range of characterisation techniques. The photocatalytic activity of the synthesised catalysts was compared in terms of a quantifiable parameter, which in this study was the half-life of photodecolourisation ($t_{1/2}$) of RhB dye under AM 1.5 irradiation.

The $t_{1/2}$ value obtained for each catalyst was attributed to the synthesis procedure of that catalyst to try and determine a relation between the catalyst synthesis and its photocatalytic activity. The aim was to try and optimise the physical properties of the photocatalyst in terms of the characteristics of the photochemically reduced

nanoparticles to obtain the highest activity for this catalyst as measured via dye degradation experiments.

The catalysts were individually examined for differences in nanoparticle size, distribution, morphology and loading.

TEM analysis revealed the size, distribution and morphology of the supported nanoparticles while ICP determined the Pd loading on theTiO_2. XPS experiments confirmed the oxidation state of the metal and UV-vis showed the difference in the optical response of the catalysts.

The adsorption coefficient of the dye to the catalyst surface was also measured. The adsorption coefficient is the quantity of dye removed from the solution through adsorption to the surface of the catalyst at equilibrium. It depends on the nature of the solute, the surface properties of the photocatalyst, pH of the solution and temperature of the reaction. The dye degradation reactions are reported to occur at the surface of the catalyst and thus the adsorption coefficient is another parameter that can be compared between photocatalysts.

This characterisation data, along with the results of the dye decolourisation experiments allowed for a quantitative comparison of the physical properties of the catalysts, to their resultant photocatalytic activities. The proceeding pages of this chapter will present and compare the results gathered from the characterisation of the catalysts.

4.2 Group 1

4.2.1 G1 - Set 1

Photocatalysts in set 1 of group 1 (G1-S1) were irradiated with UV light at an irradiance value of 2.05 mW/cm^2. A summary of the characterisation findings and results of the

RhB photodecolourisation experiments are shown in Table 4.2. The key parameters that are quantifiable and make for a meaningful comparison between the synthesis procedure and physical properties of the photocatalyst are: the loading of Pd on the TiO_2 support; the average Pd nanoparticle size; the position of the plasmon peak; the adsorption coefficient of dye to the catalyst surface and the half-life of photodecolourisation of RhB. The direct comparison of these physical properties of the photocatalyst will serve as indicators for the best combination of synthesis conditions in order to produce the most active catalyst in these reactions.

Table 4.2 Summary of the key comparable parameters of catalysts prepared in G1-S1

Catalyst	Pd per gram of catalyst/ mg	dye adsorption/ %	$t_{1/2}$/ min	Irradiation time/ min	Plasmon peak/ nm	Average Pd particle size/ nm
AL091	5.2	7.4	1.00	30	379	2.6 ± 0.6
AL093	4.2	9.4	1.01	3	437	1.9 ± 0.4
AL094	5.3	18.3	0.53	1	446	2.1 ± 0.5
AL095	5.2	12.1	1.40	0.167	437	1.8 ± 0.3

The only parameter that was changed for catalysts shown in Table 4.2 was the irradiation time. The data shows that the length of photodeposition time did not significantly affect the rate of deposition of Pd on the surface of TiO_2. The initial nucleation/deposition of Pd clearly occurs in less than 10 s. After this time, there is no significant increase in the amount of Pd reduced onto the TiO_2 even after an irradiation time of 30 min. This is supported by the ICP data.

The average nanoparticle size was measured to be smallest for sample AL095, which was subjected to the shortest irradiation period. AL091, which had the longest

irradiation exposure, was found to support relatively larger Pd nanoparticles but at a similar overall loading of Pd. The nucleation of metal nanoparticles on semiconductor supports are known to occur primarily on structural defect or electron trap sites. Upon irradiation these active surface states are rapidly occupied by reduced metal ions in contact with the support and the subsequent growth of the nanoclusters is thought to become diffusion-limited since it is observed to proceed at a much slower rate. This effect was reported by Philippe et al.[132] while investigating the kinetics of photochemical deposition of platinum onto TiO_2 particles.

The similarity in size and loading of Pd on the TiO_2 supports suggests that the initial nucleation and subsequent growth of the Pd nanoclusters are indeed governed by two different rates of reaction. This observation is supported by the TEM micrographs in Figure 4.1 showing a similar distribution and morphology of Pd on the TiO_2 where the Pd nanoparticles can be distinguished from the TiO_2 support by density and size. As Pd is denser than the TiO_2 it appears as the darker structures in the micrographs and ranging in size from 1.5 nm to 4.4 nm. No similar structures were observed when comparing TEM micrographs with untreated TiO_2.

The deposited nanoparticles were found to be hemispherical in shape for all samples and generally not evenly distributed on the surface of the TiO_2. Some areas are more densely populated than others as is most clearly visible from catalyst AL093, Figure 4.1. Most of the samples in G1-S1 exhibit a small variation in the particle sizes between the Pd nanoparticles on the same support. However, there was a greater difference in particle size observed between the Pd particles deposited on AL091 than of those deposited on the other samples of the same set. AL091 was irradiated for the longest

period of time out of this set. As the rate of particle growth post the initial nucleation phase becomes much slower and diffusion-limited, catalysts synthesised under the longest irradiation times would be expected exhibit the largest nanoparticle sizes.

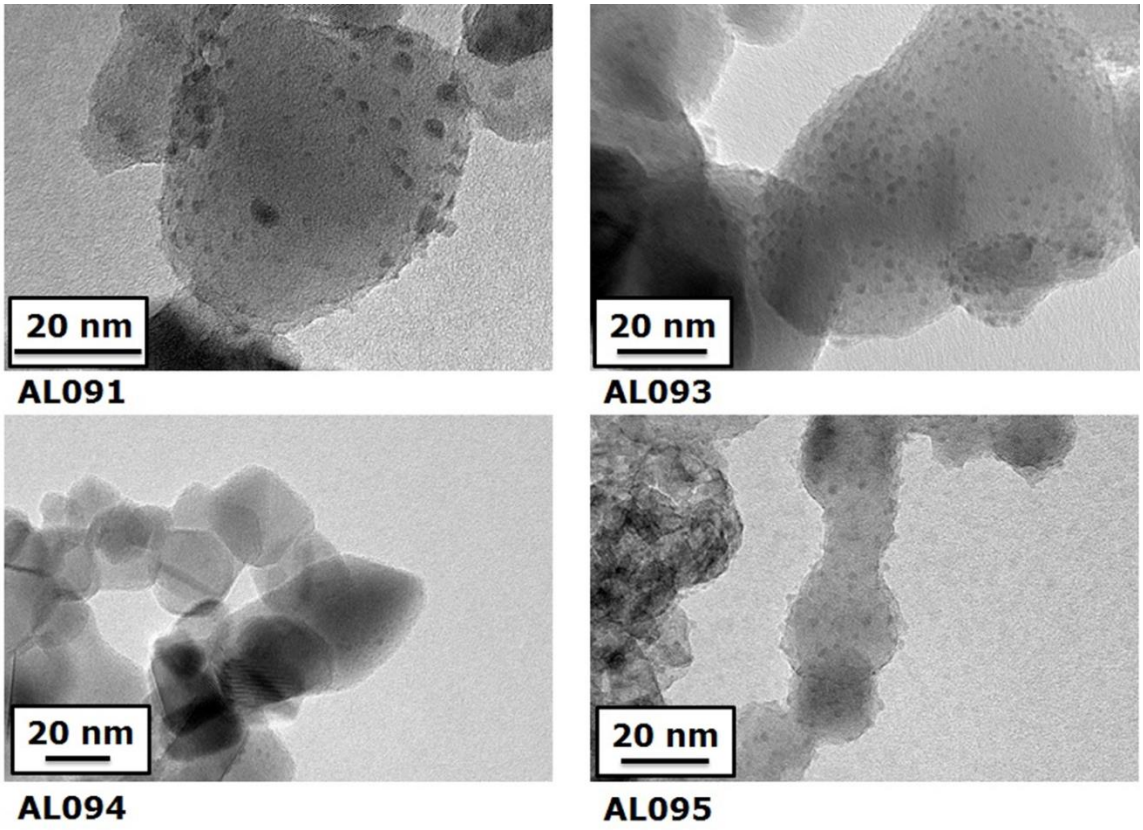

Figure 4.1 Photocatalysts in set 1 of group 1 synthesised using 10 ml of a $PdCl_2$ solution at a concentration of 0.01 M and an irradiation value of 2.05 mW/cm^2. The time of irradiation was the parameter altered for the above samples and is listed as such: AL091, 30 min; AL093, 3 min; AL094, 1 min; AL095, 10 s.

It is important to note that AL091 and AL094 were found to contain the largest average sizes of Pd nanoparticles. However, the $t_{1/2}$ value for AL091 was double compared with AL094. This can be explained by observing the position of the plasmon peak for these two samples.

The plasmon absorption peak for AL091 was measured to be in the near UV region whereas the plasmon peak for AL094 was found to be in the visible region at 446 nm. Given the similar size of average nanoparticles for these samples, the red shift in the

plasmon peak for AL094 is thought to be due to subtle differences in relative size and distribution of the Pd nanoparticles resulting in an enhancement in the physical properties of this sample compared to AL091.

The difference between AL091 and the other catalysts of the same set is highlighted in the DR measurements of the powdered samples shown in Figure 4.2. The most striking difference between the obtained spectra shown in Figure 4.2 is the intensity of the plasmon peak in the absorption profile of catalyst AL091 compared with the other catalysts in G1-S1. It is clear that under these synthesis conditions, the length of irradiation time had a significant impact on the optical response of this catalyst. An increase in absorption in the visible region was observed for all the catalysts when compared to TiO_2. The samples prepared with irradiation times of up to 3 min exhibited similar increases in optical response. However, AL091 which was synthesised with a length of irradiation time of 30 min showed the largest increase in absorption.

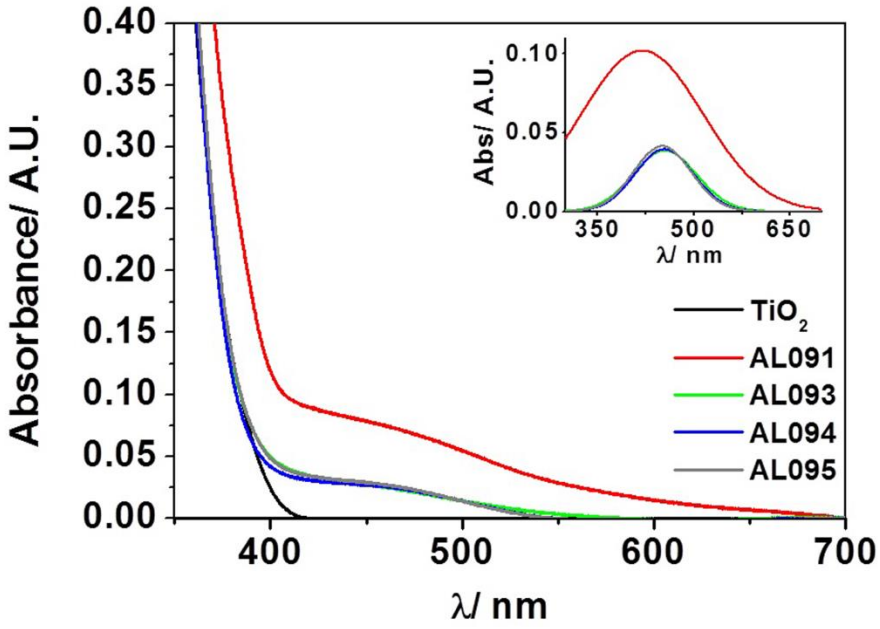

Figure 4.2 DR measurements of the absorption profiles of catalysts in G1-S1 compared with TiO_2

This increase in the optical response for the photocatalysts is attributed to the presence of the Pd nanoparticles and the associated LSPR of the Pd. The inset in Figure 4.2 shows a fit of the plasmon absorption peak associated with the photocatalysts (See Appendix B for calculations of the plasmon fit). From this fit, the peak positions of the Pd plasmons are centred on an average at position of 440 nm, with the exception of catalyst AL091, which has its peak centred at 379 nm. It is not clear why this blue-shift in the plasmon peak was observed. However, as the position of the plasmon peak is known to be highly sensitive to the local environment,[60,139] it is likely that the relative distribution of the Pd nanoparticles on the support, as well as their relative sizes, has influenced the position and intensity of the plasmon for this catalyst.

4.2.2 G1 - Set 2

Photocatalysts in set 2 of group 1 (G1-S2) were irradiated with UV light at an irradiance value of 9.54 mW/cm^2. The physical properties and photocatalytic activity of the catalysts are summarised in Table 4.3.

Table 4.3 Summary of the key comparable parameters of catalysts prepared in G1-S2

Catalyst	Pd per gram of catalyst/ mg	dye adsorption/ %	$t_{1/2}$/ min	irradiation time/ min	Plasmon peak/ nm	Average Pd particle size/ nm
AL092	5.4	12.3	3.28	30	477	1.6 ± 0.4
AL112	4.9	-	1.17	3	409	1.7 ± 0.4
AL096	5.5	20.5	0.63	1	442	1.4 ± 0.4
AL097	4.9	10.1	0.43	0.167	438	2.0 ± 0.7

From the values presented in Table 4.3, there is a clear correlation for photocatalysts in this group between the length of irradiation time and photocatalytic activity such that the $t_{1/2}$ value of RhB increased with increasing catalyst synthesis irradiation time. However, other key parameters do not show any obvious trends related to the increase in the length of irradiation time. For example, the catalyst loading varies by ± 0.6 mg successively. The loading of Pd was observed to be highest at irradiation times of 30 min and 1 min and lowest for the irradiation times of 3 min and of 10 s. Also, the peak of the plasmon shifted to the red by 4 nm for AL096, which was synthesised at a UV exposure period of 1 min compared to AL097, which had a UV exposure of 10 sec. A blue-shift of 33 nm then occurs for sample AL112 followed by a red-shift of 68 nm for AL092.

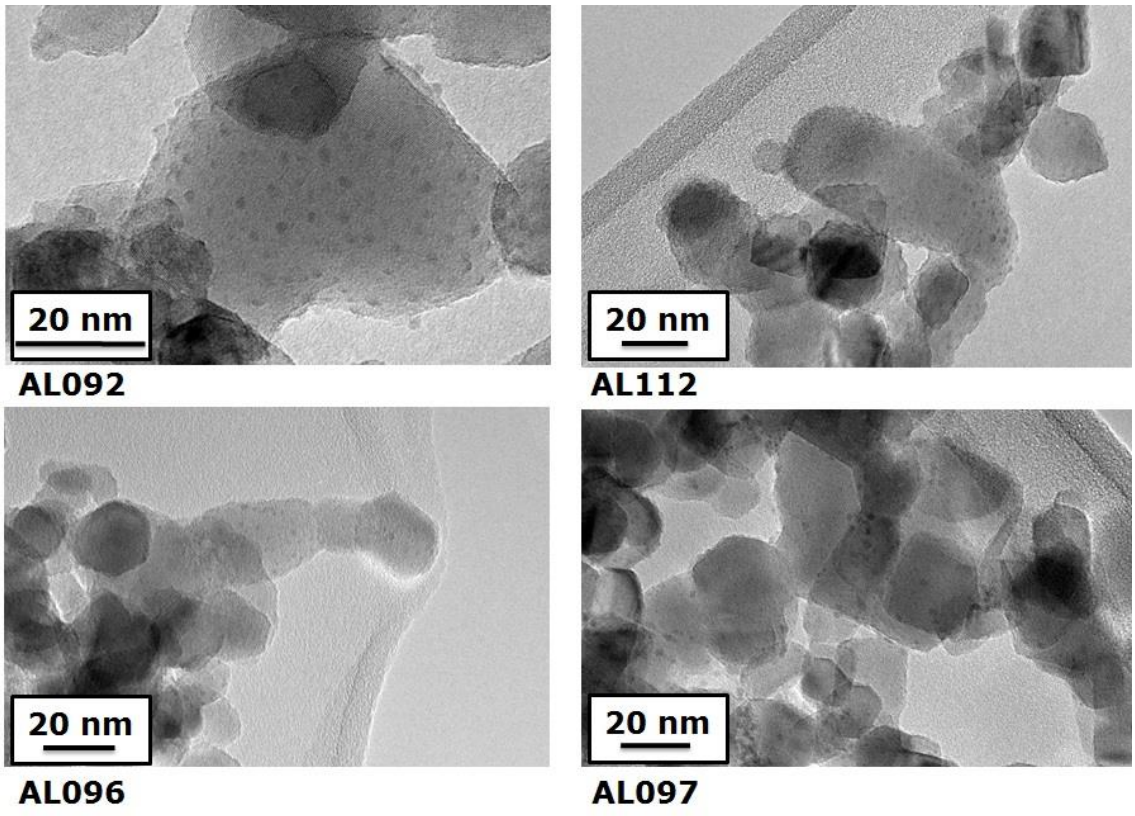

Figure 4.3 Photocatalysts in set 2 of group 1 synthesised using 10 ml of a $PdCl_2$ solution at a concentration of 0.01 M and an irradiation value of 9.54 mW/cm^2. The time of irradiation was for each sample was AL092 = 30 min; AL112 = 3 min; AL096 = 1 min; AL097 = 10 s.0

Figure 4.3 shows that distribution and morphology of the Pd nanostructures on all of the samples in this set are similar. Again, the Pd nanoparticles are shown to be hemispherical and relatively well distributed across the particle surface. One notable difference between the deposited Pd nanoparticles of this set compared with those of G1-S1 is the overall average size of the nanoclusters. The supported nanoparticles in G1-S2 are on average 0.4 nm smaller than those in G1-S1. Furthermore, the length of irradiation period for the catalysts synthesised in this group (G1-S2) was observed to have had a greater influence on their optical properties compared with the catalysts in G1-S1. Figure 4.4 shows the DR measurements of photocatalysts synthesised in G1-S2.

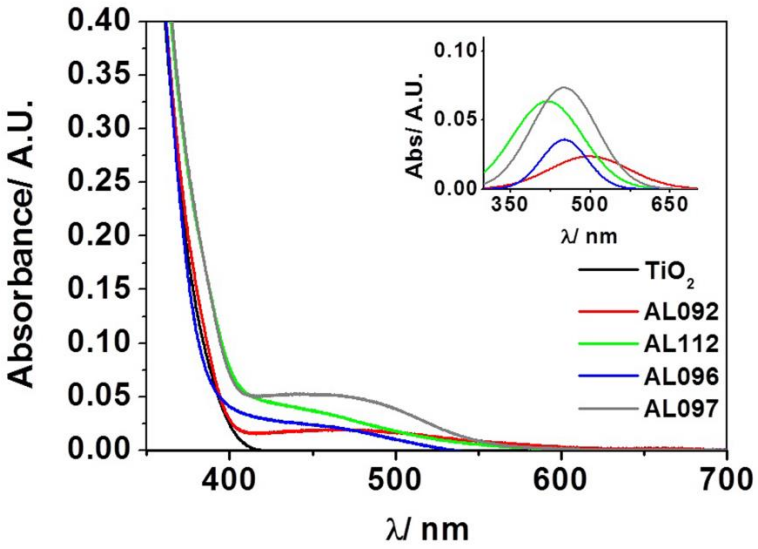

Figure 4.4 DR measurements of the absorption profiles of catalysts in G1-S1 compared with TiO_2

The photocatalyst exhibiting the highest relative intensity of optical response, AL097 was found to photodecolourise RhB at the highest rate, while the photocatalyst with the lowest relative intensity of optical response (AL092) decolourised the dye at the lowest rate. However, AL112 and AL096, the two photocatalysts synthesised using the intermediate irradiation times, did not follow this trend. AL112 shows a higher relative

intensity in terms of its optical response but a slower rate of photodecolourisation of RhB compared with AL096. Figure 4.4 shows that there is a greater difference between the absorption profiles of the catalysts in this set compared with those in G1-S1, which may be a result of the increase in irradiance value of the light source for the photochemical deposition of these nanoparticles.

4.2.3 G1 discussion

All of the photocatalysts in G1 exhibited an increase in absorption over the visible region. This increase in absorption is attributed to the LSPR effect of Pd. XPS confirmed the presence of metallic Pd on the TiO_2, which adds support to the plasmonic effect of Pd (See chapter 5 for XPS results). It is known that Pd exhibits a plasmon resonance in the UV region however, there is a growing body of work indicating that the plasmonic properties of Pd nanoparticles may be influenced by particle size and local environment as discussed in section 2.7 of chapter 2.

The photocatalytic activity of catalysts in G1-S1 appeared to be dependent a number of factors including the loading of Pd, nanoparticle size and on the position of the plasmon peak. The length of irradiation time did not appear to have a significant effect on the properties of catalysts in this group. In contrast, the length of UV exposure for catalysts in G1-S2 influenced the photocatalytic activities such that longer irradiation periods resulted in an increase in $t_{1/2}$ value of RhB and therefore a reduction in catalytic activity. The wider range in activity observed for samples in G1-S2 as a function of photochemical deposition time, compared with samples in G1-S1, indicates a larger influence of the intensity of the irradiation on the physical properties of the catalysts. There was little

influence of the irradiance value and exposure period on the total amount of metal deposited for all catalysts in G1.

It was observed that the average size of nanoparticles deposited on G1-S2 catalysts were overall smaller than those of G1-S1 catalysts. It has been reported that the intensity of UV exposure influences the density of metal nucleation sites on the TiO_2 such that irradiation of higher intensity values results in an increase in the distribution of photochemically deposited nanoparticles over the surface of the support.[216] The results of the analysis of the catalysts in this group adds weight to this theory. For this group, relatively higher intensity of UV during photochemical reduction of metal was found to be produce Pd nanoparticles that were on average smaller than those produced using lower intensity UV.

Group 2 photocatalysts

4.2.4 G2 - Set 1

Photocatalysts in set 1 of group 2 (G2-S1) were irradiated with UV light at an irradiance value of 9.54 mW/cm^2. The physical properties and photocatalytic activity of the catalysts are summarised in Table 4.4. The synthesis of catalysts in G2 used half the volume of solution, but double the concentration of $PdCl_2$ used in the synthesis of catalysts in G1. The $PdCl_2$ solution used in G2 contained the same molar amount of Pd as the solution used for the synthesis of catalysts in G1. The aim was to investigate the effect of this difference on the photodeposition of the Pd compared with those in G1.

Characterisation of the catalysts in G2-S1 showed a correlation between the length of irradiation time of the catalysts and the position of the Pd plasmon peak, and to some extent the average nanoparticle size. The optical response peaks of these catalysts were

observed to red-shift with increasing irradiation time. The value of the change in red-shift was also found to correspond to an increase in irradiation time.

Table 4.4 Summary of the key comparable parameters of catalysts prepared in G2-S1

Catalyst	Pd per gram of catalyst/ mg	dye adsorption/ %	$t_{1/2}$/ min	irradiation time/ min	Plasmon peak/ nm	Average Pd particle size/ nm
AL098	5.8	11.4	0.66	30	453	2.5 ± 0.8
AL099	5.9	18.6	0.55	3	438	2.8 ± 0.5
AL100	5.8	12.0	0.83	1	432	2.2 ± 0.5
AL101	5.9	16.0	0.95	0.167	430	1.8 ± 0.3

The loading amount of Pd on catalysts in G2-S1 was consistent and independent of the length of irradiation time. In general, the Pd loading amounts were 0.5 mg – 1.0 mg higher than those of catalysts in G1. This consistency in the value of the photodeposited Pd supports the theory of a rapid initial nucleation followed by a slow diffusion-limited growth mechanism. The Pd nanoparticles were observed to grow in size with increasing UV exposure up to a photodeposition time of 3 min. Another correlation observed up to this point was the increase in the rate of photodecolourisation of RhB. However, no similar trend was detected for the adsorption coefficient.

In this group, an increase in nanoparticle size corresponded to an increase in the optical response of the photocatalysts in the visible region, which in turn corresponded to an increase in photocatalytic activity. This correlation between the increased visible absorption of the photocatalyst and its improved photocatalytic efficiency shows that the activity of the catalysts is directly related to its visible light harvesting potential. Figure 4.5 contains the TEM micrographs of the G2-S1 catalysts where the size and

distribution of the Pd nanoparticles are shown. The TEM micrographs clearly demonstrate the increase in particle size with a longer period of UV irradiation time.

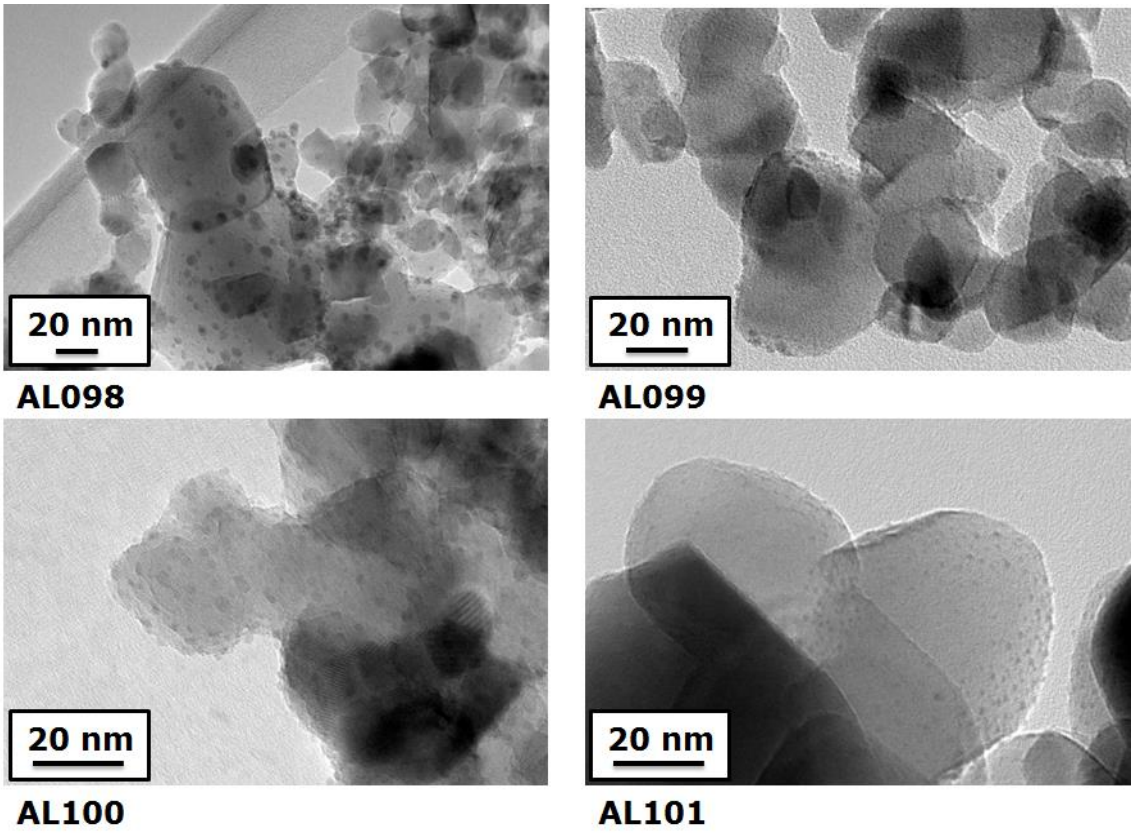

gure 4.5 Photocatalysts in set 1 of group 2 synthesised using 5 ml of a $PdCl_2$ solution at a concentration of 0.02 M and an irradiation value of 9.54 mW/cm^2. The time of irradiation was for each sample was AL098 = 30 min; AL099 = 3 min; AL100 = 1 min; AL101 = 10 s.

Close inspection of Figure 4.5 also revealed that the distribution density of nanoparticles on the surface of the catalysts varies as a function of UV exposure, while the size of the nanoparticles gradually increases over the time. The difference in the distribution of nanoparticles between photocatalysts is thought to be a consequence of the inherent discrepancies in the number of available active surface states between different samples. Particle size and standard deviation measurements, coupled with the ICP analysis of the loading of Pd confirmed the rapid initial nucleation and deposition of Pd followed by a slower nanocluster growth. This observation further supports the concept

of two separate reaction rates occurring; one dominated by the number of available active sites on the surface of the support (initial nucleation and growth) and the second dominated by diffusion of metal ions to established nanoclusters (nanocluster growth).

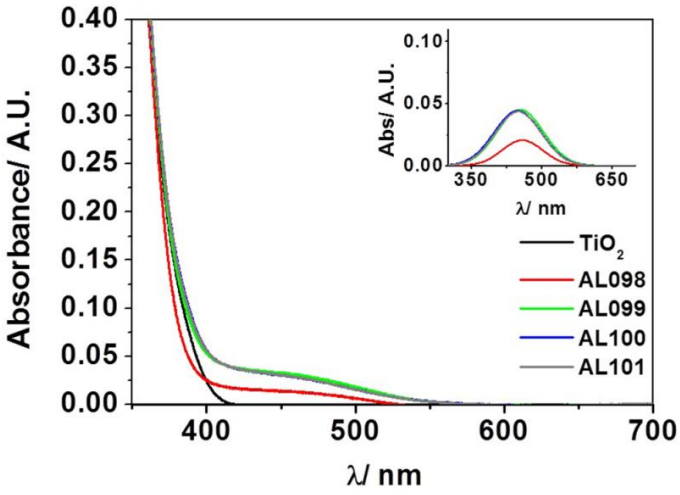

Figure 4.6 DR measurements of the absorption profiles of catalysts in G2-S1 compared with TiO_2

DR measurements of the absorption of catalysts in G2-S1 showed that the intensity of the optical response does not vary significantly for catalysts AL099, AL100 and AL101. However, the intensity of absorption plasmon peak for sample AL098 is significantly lower than the others.

4.2.5 G2 - Set 2

Photocatalysts in set 2 of group 2 (G2-S2) were irradiated with UV light at an irradiance value of 2.05 mW/cm^2. The physical properties and photocatalytic activity of the catalysts are summarised in Table 4.5.

A similar trend was observed for catalysts in G2-S2 compared with catalysts in G2-S1 for where the Pd loading as determined by ICP analysis showed a similar consistency that was independent of photodeposition time. The Pd loading values on TiO_2 were consistent with those of samples in G2-S1 and were also on average 0.5 mg – 1.0 mg

higher than catalysts in G1. Secondly, the $t_{1/2}$ value of RhB decreased with increasing photodeposition irradiation time up to and including AL103 where after this point, the $t_{1/2}$ value increased significantly.

Table 4.5 Summary of the key comparable parameters of catalysts prepared in G2-S2

Catalyst	Pd per gram of catalyst/ mg	dye adsorption/ %	$t_{1/2}$/ min	irradiation time/ min	Plasmon peak/ nm	Average Pd particle size/ nm
AL102	6.0	11.5	1.15	30	440	1.6 ± 0.3
AL103	5.9	15.1	0.58	3	448	3.0 ± 0.7
AL104	5.8	13.2	0.92	1	441	1.3 ± 0.3
AL105	5.9	12.7	1.19	0.167	435	1.7 ± 0.8

The increase in activity corresponded to a red-shift in the position of the plasmon peak, along with an increasing adsorption coefficient as a function of the photodeposition irradiation time. While for AL102, which was irradiated for a period of 30 minutes, the decrease in activity correlated to a blue-shift in the position of the plasmon peak as well as a decrease in the dye adsorption coefficient. It appears that the prolonged UV exposure had a negative effect on the photocatalytic activity for catalyst AL102, indicating that the conditions of the synthesis in this case were suboptimal.

The two most photocatalytically active samples out of the G2 catalysts were AL099 (G2-S1) and AL103 (G2-S2). Both were synthesised with a UV irradiation time of 3 min and show similar physical properties in terms of loading of Pd, average nanoparticle size, position of the Pd plasmon peak and adsorption coefficient. The similarity in the characteristics of the two catalysts suggests that there is an optimum length of UV

irradiation time irrespective of the irradiance value. Figure 4.7 shows the TEM micrographs obtained for the photocatalysts in G2-S2.

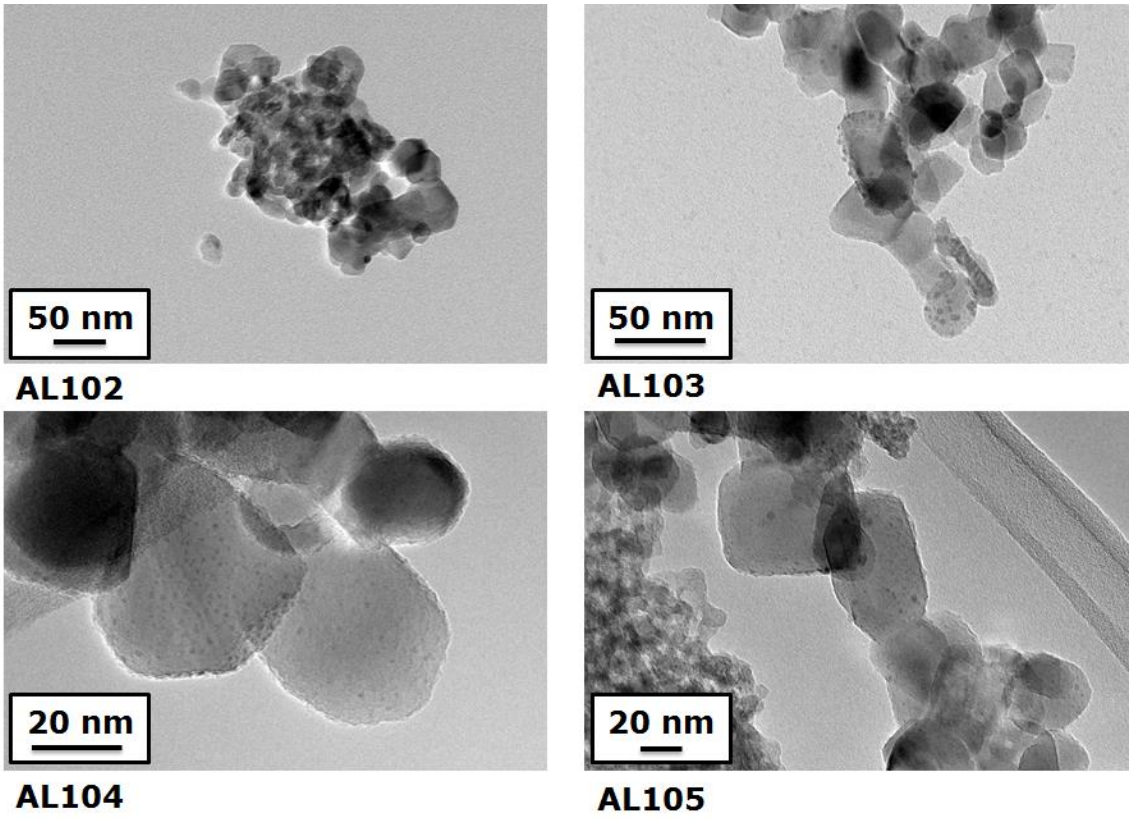

Figure 4.7 Photocatalysts in set 2 of group 2 synthesised using 5 ml of a $PdCl_2$ solution at a concentration of 0.02 M and an irradiation value of 2.05 mW/cm^2. The time of irradiation was for each sample was AL102 = 30 min; AL103 = 3 min; AL104 = 1 min; AL105 = 10 s.

Both catalysts in G2 synthesised with irradiation times of 30 min exhibited a lower intensity of absorption in DR measurements as well as a decrease in average nanoparticle size compared with catalysts synthesised at irradiation lengths of 3 min. In both sets, similar trends for catalysts synthesised with irradiation lengths up to and including 3 min of UV were observed. Figure 4.8 confirms the decrease in optical response intensity for AL102.

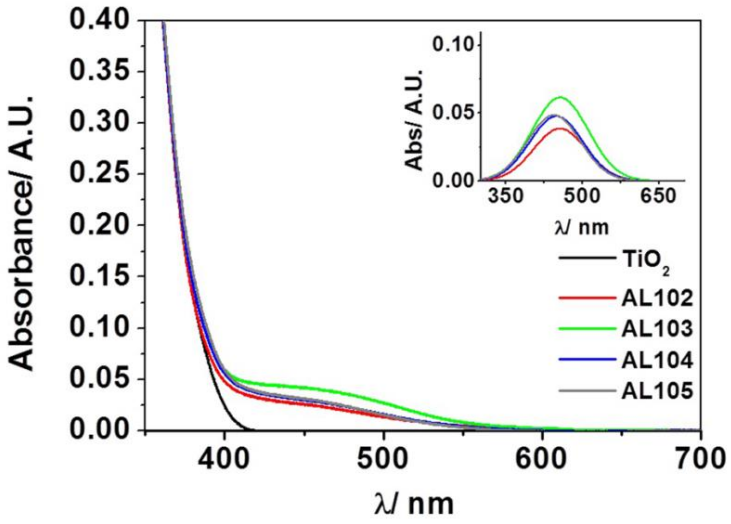

Figure 4.8 DR measurements of the absorption profiles of catalysts in G2-S2 compared with TiO_2

The standout feature of Figure 4.8 is the increase in absorption intensity for catalyst AL103 as shown in the inset. This is the sample with the lowest $t_{1/2}$ value, whereas catalyst AL105 which has among the lowest absorption intensity showed the highest $t_{1/2}$ value of G2-S2. This result is in line with the trend that photocatalysts exhibiting the highest increase in absorption intensity correspond to the most active photocatalysts. This is attributed to the increase in visible light harvesting potential of the catalyst.

4.2.6 G2 discussion

The reduction in volume, coupled with the higher concentration of the precursor solution for the synthesis of G2 catalysts, resulted in a small increase in the total amount of Pd photochemically deposited on the TiO_2 for these samples compared with catalysts in G1. The amount of Pd deposited was observed to be consistent and independent of the period of UV exposure for the timescales used during deposition.

Though the weight percent of the deposited Pd was consistent, the period of UV exposure was found to have a small effect on the position of the plasmon peak and the

average size of supported Pd nanoparticles. Both sets of catalysts in G2 exhibited a red-shift in position of the plasmon peak with increasing length of UV exposure, which corresponded to an increase in photocatalytic activity. Catalysts in G2-S1 were found to be overall more photocatalytic than samples in G2-S2. It was also observed that the average Pd nanoparticle sizes of the catalysts in G2-S1 increased as a function of irradiation time up to. This was not the case for catalysts in G2-S2 where the average size of the Pd nanoparticles were generally smaller than those in G2-S1.

For both sets of catalysts in G2, the photocatalytic activity of samples synthesised at a UV exposure period of 30 min was observed to decrease. A corresponding reduction in Pd nanoparticle size for these catalysts compared to those synthesised with 3 min UV irradiation time was also measured.

The result of the particle size analysis and Pd loading measurements of photocatalysts within this group highlights the influence of UV intensity on photochemically deposited particle size and therefore, the distribution. Catalysts in G2-S2 were found to contain Pd nanoparticles with smaller mean diameters than catalysts in G2-S1, while they both had similar Pd loading values. The average size of Pd nanoparticles in G2-S1 was calculated to be (2.3 ± 0.5) nm, whereas for G2-S2, the mean diameter of supported Pd was found to be (2.1 ± 0.5) nm. The mean loading content of catalysts in both sets in G2 was found to be 0.6 wt%. This result strongly indicates that irradiation of the semiconductor support with relatively higher intensity of UV light during the photochemical reduction procedure produces Pd nanoclusters with smaller mean diameters than those irradiated with a lower intensity UV light.

4.3 Group 3 photocatalysts

4.3.1 G3 - Set 1

Photocatalysts in set 1 of group 3 (G3-S1) were irradiated with UV light at an irradiance value of 9.54 mW/cm^2. The physical properties and photocatalytic activity of the catalysts are summarised in Table 4.6.

The change in the volume of the $PdCl_2$ solution for catalysts in G3 compared to those in G2 corresponded to an increase in the measured Pd loading. The concentration of Pd in the precursor solution for catalysts synthesised in G3 was double the concentration used in the synthesis of G1 and G2 catalysts. The increase in the overall Pd loading was observed to be moderate and resulted in an additional 1mg – 2 mg of Pd compared with catalysts in G1 and an additional amount of Pd of between 0.4 mg – 0.8 mg compared with catalysts in G2.

Table 4.6 Summary of the key comparable parameters of catalysts prepared in G3-S1

Catalyst	Pd per gram of catalyst/ mg	dye adsorption/ %	$t_{1/2}$/ min	irradiation time/ min	Plasmon peak/ nm	Average Pd particle size/ nm
AL106	6.1	14.2	0.46	30	454	2.2 ± 0.5
AL113	6.3	5.8	0.77	3	432	2.0 ± 0.5
AL107	5.9	17.3	0.92	1	419	2.3 ± 0.8
AL108	5.9	12.3	0.38	0.167	439	3.1 ± 0.5

The size and amount of photochemically deposited Pd nanoparticles measured from the samples in this G3-S1 was found to be a similar value to other catalysts within this set. However, it was observed to an extent that an increase in the red-shift of the plasmon peak corresponded to an increase in photocatalytic activity.

The adsorption coefficient did not appear to follow any obvious trend for catalysts in this group. Figure 4.9 shows the TEM micrographs for catalysts in G3-S1.

Again, the Pd loading on catalysts in G3-S1 does not depend on the UV irradiation time and adds weight to the rapid initial nucleation with subsequent growth of the Pd nanoclusters at a much slower rate. The distribution of Pd on all of the catalysts in G3-S1 appears to vary randomly with length of irradiation and is thought have an effect on the position of the plasmon peak.

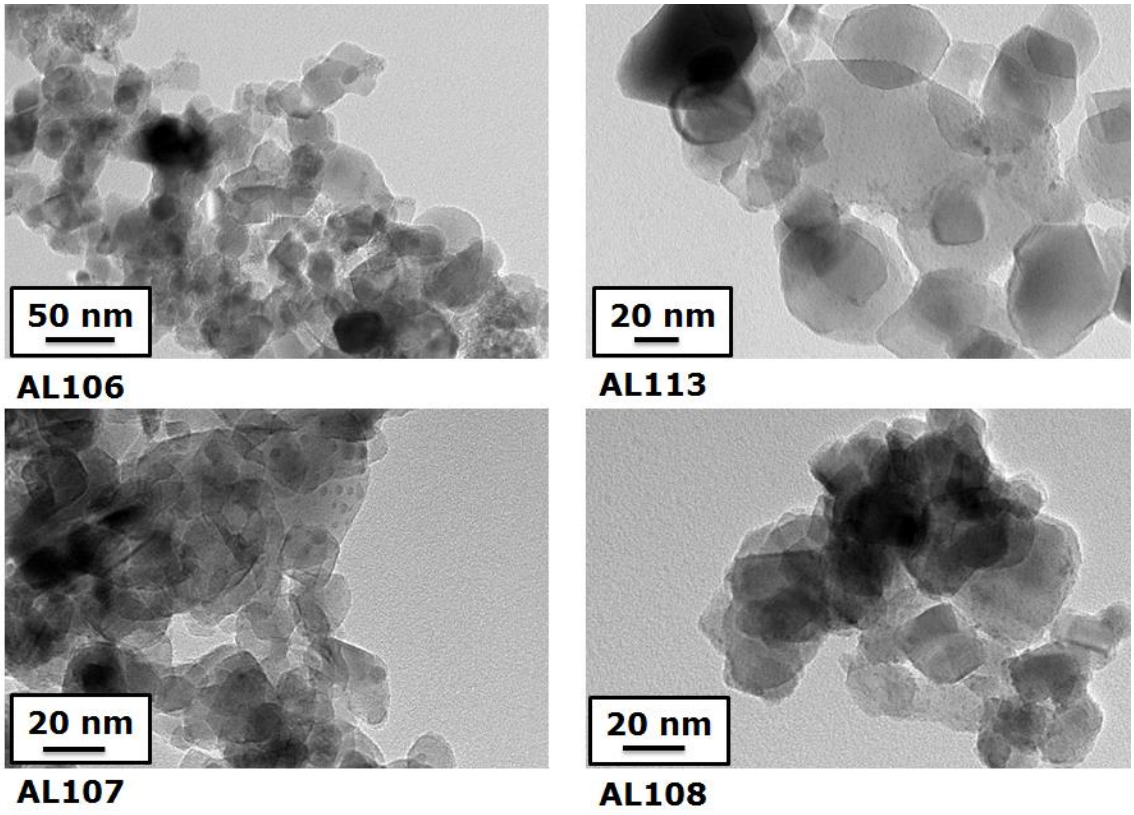

Figure 4.9 Photocatalysts in set 1 of group 3 synthesised using 10 ml of a $PdCl_2$ solution at a concentration of 0.02 M and an irradiation value of 9.54 mW/cm². The time of irradiation was for each sample was AL106 = 30 min; AL113 = 3 min; AL107 = 1 min; AL108 = 10 s.

The photocatalyst in G3-S1 with the highest activity was found to be AL108. This sample also had the highest measured average nanoparticle size and Pd loading for catalysts in G3-S1. The position of the plasmon peak of AL108 was significantly red-shifted

compared with that of AL107 and only slightly red-shifted compared AL113. Catalyst AL106 showed the largest red-shift of samples in this group.

The investigation into the optical response of the catalysts revealed that AL108 exhibited the largest relative intensity in absorption compared with other samples in this group. Furthermore, a reverse trend was observed for the remaining samples in G3-S1 where a higher intensity in the absorption spectrum actually corresponded to a lower photocatalytic activity. Figure 4.10 highlights this observation.

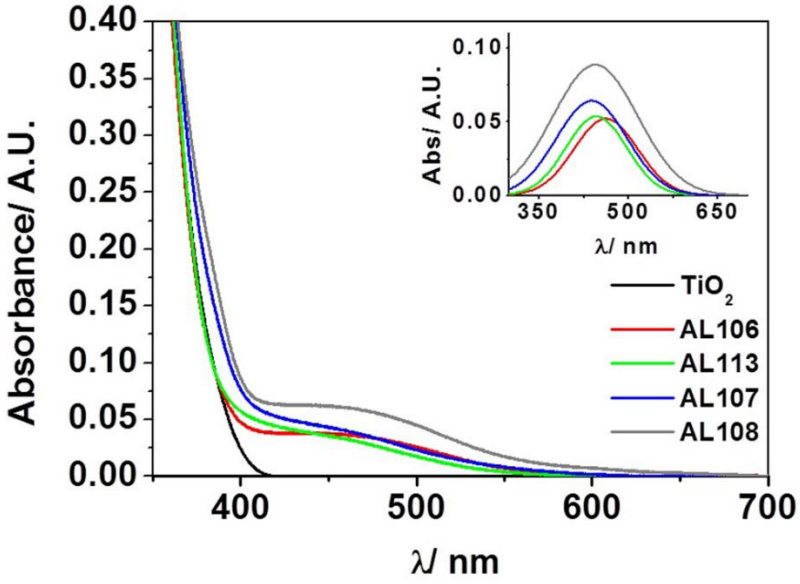

Figure 4.10 DR measurements of the absorption profiles of catalysts in G3-S1 compared with TiO_2

4.3.2 G3 - Set 2

Photocatalysts in set 2 of group 3 (G3-S1) were irradiated with UV light at an irradiance value of 2.05 mW/cm^2. The physical properties and photocatalytic activity of the catalysts are summarised in Table 4.7.

The Pd loading content for catalysts in this group was similar to the levels found for catalysts in G3-S1 but with a higher maximum loading of 6.5 mg for AL114 compared

with 6.3 mg for AL113, which was the highest Pd loading measured in G3-S1. No trend in the catalyst adsorption coefficient was observed related to the photocatalytic activity or any other measured physical property. However, other trends were observed for the activity of photocatalysts in this group that were dependent on the physical properties of the samples. For instance, both the position of the Pd plasmon peak and the catalytic activity of the photocatalysts were found to increase with longer UV irradiation times. Figure 4.11 shows the TEM micrographs of photocatalysts synthesised in G3-S2.

Table 4.7 Summary of the key comparable parameters of catalysts prepared in G3-S2

Catalyst	Pd per gram of catalyst/ mg	dye adsorption/ %	$t_{1/2}$/ min	irradiation time/ min	Plasmon peak/ nm	Average Pd particle size/ nm
AL109	6.3	13.9	0.36	30	454	2.9 ± 0.7
AL114	6.5	10.9	0.46	3	447	1.7 ± 0.5
AL110	5.4	14.6	0.52	1	428	2.3 ± 0.5
AL111	6.3	22.2	0.53	0.167	425	1.9 ± 0.5

The average loading of Pd was similar to that of G3-S1 samples and were overall higher than amounts measured for G1 and G2 catalysts. In this respect, the results show that increasing the loading of Pd n the TiO_2 support in turn increases the photocatalytic activity of the catalysts.

The sample with the lowest $t_{1/2}$ value of all the synthesised catalysts in any group was found to be AL109, which had one of the largest measured average Pd nanoparticle sizes and standard deviation. This catalyst was irradiated with UV for the longest period of time within the experimental conditions during the synthesis.

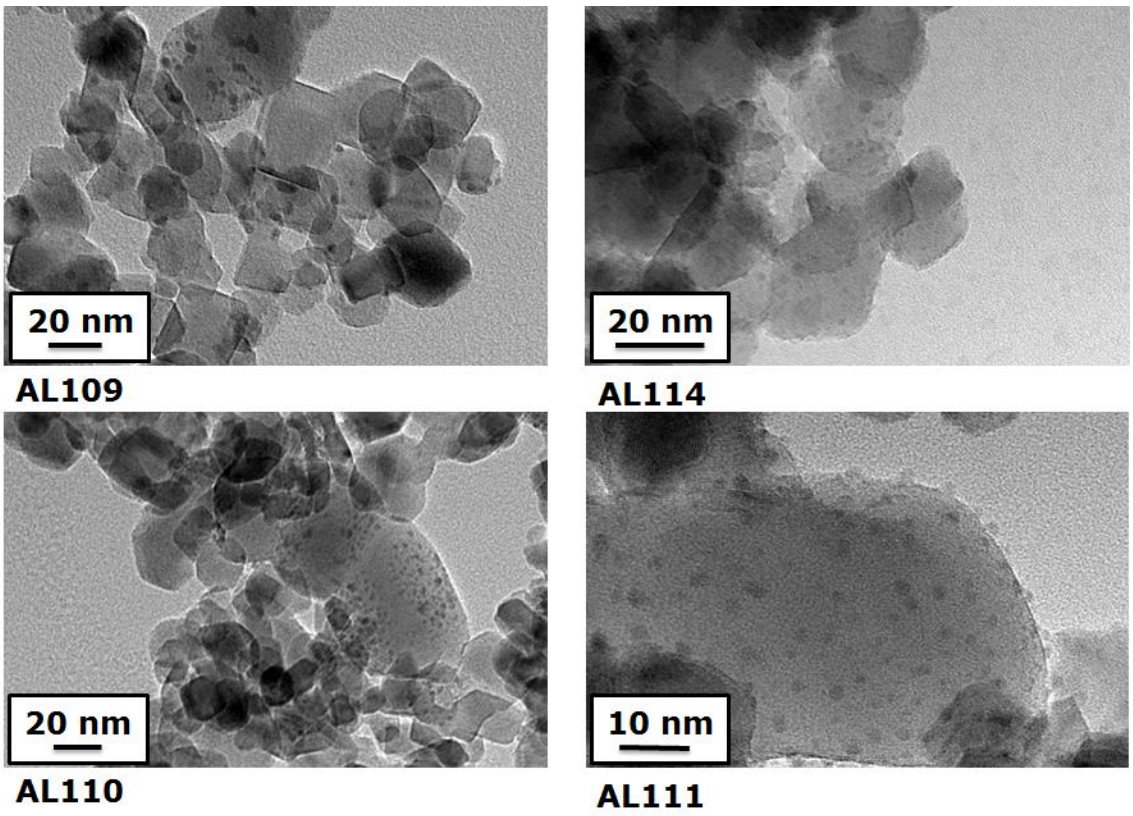

Figure 4.11 Photocatalysts in set 2 of group 3 synthesised using 10 ml of a $PdCl_2$ solution at a concentration of 0.02 M and an irradiation value of 2.05 mW/cm^2. The time of irradiation was for each sample was AL109 = 30 min; AL114 = 3 min; AL110 = 1 min; AL111 = 10 s.

DR analysis showed that higher absorption intensities observed in catalysts in this group did not correspond to the most active photocatalysts and there was no trend found relating to the absorption intensity of catalysts in G3-S2. Figure 4.12 shows the absorption spectra for catalysts in this group.

It was observed that the absorption intensity of the Pd plasmon was an indicator of the photocatalytic activity of the catalyst, such that samples exhibiting the highest intensities were found to be the most active in terms of the photodecolourisation of RhB. This was not the case for catalysts in G3-S2.

The main indicator for photocatalytic activity in this group was found to be the position of the Pd plasmon peak, which was found to be dependent on the UV irradiation time.

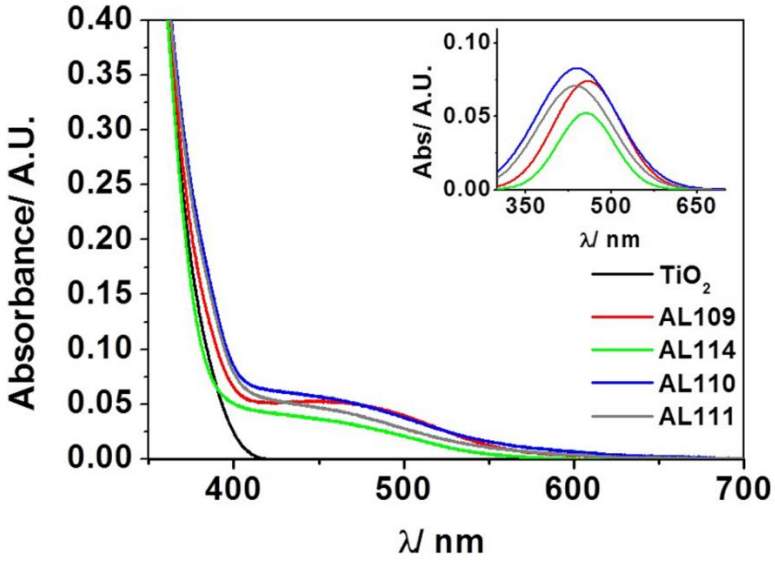

Figure 4.12 DR measurements of the absorption profiles of catalysts in G3-S2 compared with TiO_2

4.3.3 G3 discussion

The photocatalysts in G3 were found to have a higher loading of Pd compared with samples in G1 and G2. The increase in weight percent of Pd corresponded to an overall improvement in the photocatalytic performance of these catalysts, which showed similar red-shifts in the position of the plasmon peaks as previously observed.

For samples in G3 a reduction in nanoparticle size was not observed for catalysts synthesised with 30 min UV exposure. The size of the Pd nanoclusters of samples in G3 were observed to be overall larger than those in G2 and G1. It is evident that the higher volume and concentration of precursor solution for catalysts in G3 resulted in a higher total loading of Pd on these catalysts and highlighting the dependence of Pd nucleation on initial metal concentration in the precursor.

G3-S2 catalysts were on the whole more photocatalytically active than those in G3-S1, suggesting that a higher intensity of UV irradiation is more favourable under these

conditions to produce a more active photocatalyst. The average Pd nanoparticle sizes for G3-S2 were also on the whole relatively larger than those in G3-S1.

4.4 Summary of key findings

The physical properties of 24 different photocatalysts were investigated. Several parameters were altered to determine their effect on the physical characteristics of the catalysts and on the photocatalytic efficiency of these samples in the decolourisation of RhB dye.

The main findings of this study were:

- The initial nucleation and growth of the Pd nanoparticles is a rapid mechanism that is induced by the onset of UV irradiation and is dependent on the initial concentration of metal ions in the precursor
- Subsequent growth of the Pd nanocluster proceeds at a much slower rate as this now becomes diffusion limited once the surface states on the outer layer of powder become increasingly occupied by metal nanoclusters
- Maintaining the concentration of Pd within the precursor solution but decreasing the solution volume resulted in a small increase in the deposition of metal onto TiO_2. This also had the effect of increasing the photocatalytic efficiency of the photocatalysts
- Doubling the concentration of Pd in the precursor solution resulted in a further increase of the total photochemically deposited amount of Pd. At this concentration and volume, the period of UV exposure during the photochemical deposition procedure influenced the position of the plasmon peak such that longer irradiation times resulted in further red-shifted peaks

- Overall, the photocatalytic activity of the catalysts was found to be dependent on the loading and size of the Pd nanoparticles, as well as the position of the plasmon peak. Higher concentrations of Pd in the precursor solution resulted in a greater loading of Pd on the TiO_2 support, which in turn were found to be larger in average particle size and exhibited a relatively larger red-shift of the position of the Pd plasmon peak.

The analysis of the data relating to the physical properties of the synthesised catalysts revealed the correlations stated above. Figure 4.13 shows the correlation between the positions of the plasmon peaks and the length of UV irradiation during catalyst synthesis.

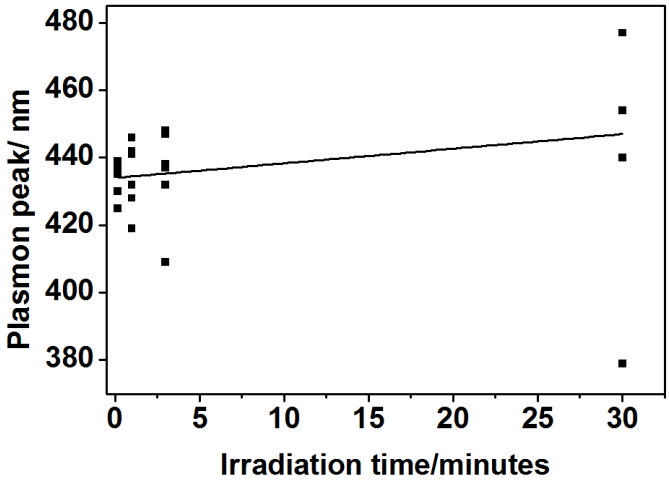

Figure 4.13 Correlation of average position of the Pd plasmon as a function of irradiation time of photochemical deposition

Compared with the unmodified TiO_2, all synthesised catalysts exhibited a response in the visible region that was attributed to the Pd nanoparticles on the surface. It was found that most of the synthesised catalysts had a plasmon peak position of between 430 nm and 455 nm. This trend is shown in Figure 4.14.

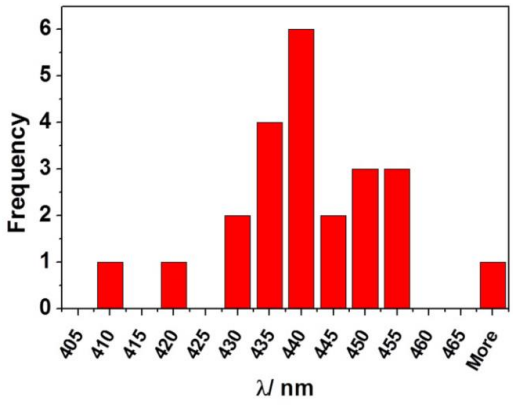

Figure 4.14 Histogram of the position of the plasmon peak and the number of photocatalysts with peaks at those positions

As experiments were carried out using simulated solar light, the red-shift of the position of the plasmon peak indicates that these catalysts are able to harvest a greater proportion of the incident visible light for photochemical reactions on their surfaces compared with catalysts that have less re-shifted plasmon peaks. Catalysts with the highest level of photocatalytic activity in terms of the $t_{1/2}$ value of RhB dye tended to have Pd nanoparticles with an overall larger mean particle size, Figure 4.15.

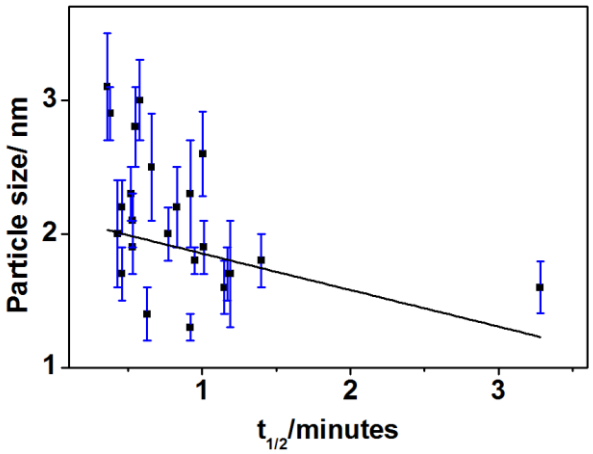

Figure 4.15 Trend of the increase in the photocatalytic activity of catalysts in terms of the $t_{1/2}$ value as a function of the mean Pd nanoparticle size

Figure 4.16 shows the trend of $t_{1/2}$ value as a function of the Pd wt%. The data point situated at a $t_{1/2}$ value of > 3 min belongs to catalyst AL092 and is thought to be an outlier in this data set. The results of the analysis of the physical properties of this catalyst do not lie within the general trend and it is thought that this particular catalyst represents an error in the data. Nevertheless, the correlations between Pd content, particle size, activity and position of the plasmon peak are such that the inclusion of this data point within the analysis does not significantly affect the trend of the results.

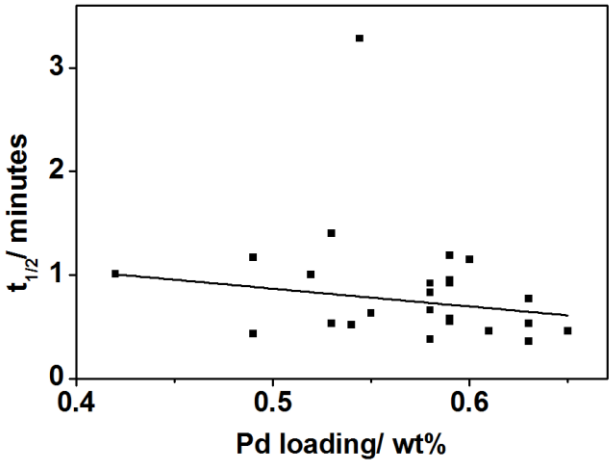

Figure 4.16 The photocatalytic activity of all the synthesised catalysts in this study as a function of the position of the Pd plasmon peak.

One of the most significant findings of this study was the observation of the kinetics of nucleation and growth of the Pd nanoparticles on the surface of TiO_2. These experiments showed that the initial nucleation and growth occurred according to two separate mechanisms upon the onset of irradiation with UV light. Firstly, nucleation and growth occurs rapidly upon irradiation. The actual initial nucleation/deposition time of Pd is believed to be in the order of milliseconds. These timescales were observed by Jacobs in 1986[216] when depositing Pd on TiO_2 based thin film substrates where nucleation occurs primarily in structural defect/ electron trap sites on the TiO_2 surface. Secondly,

growth of established Pd nanoclusters is occurs via a much slower diffusion-limited process. The process can be summarised via the following mechanisms:[217]

$$Pd^{2+} \xrightarrow{k_1} Pd^0 \quad \textbf{(4.1)}$$

where k_1 is rate of nucleation of Pd nanoclusters upon UV irradiation and is proceeded by the second mechanism:

$$Pd^{2+} + Pd^0 \xrightarrow{k_2} 2Pd^0 \quad \textbf{(4.2)}$$

where k_2 is the rate of diffusion limited nanocluster growth, which is much slower than k_1. The results of the particle size study support these two mechanisms where upon UV irradiation, the Pd nanoparticles nucleate and rapidly grow to an average size via the mechanism given in Equation 4.1. This step was found to be influenced by the initial concentration of Pd ions in the solution. The mean size for Pd nanoparticles in G1, G2 and G3 were measured to be (1.9 ± 0.5) nm, (2.1 ± 0.5) nm and (2.3 ± 0.5) nm, respectively. The second mechanism, (Equation 4.2) of growth of the established Pd nanoclusters via a diffusion limited process, was found to have a more significant effect on the physical properties of the catalysts.

It was found that the position of the plasmon peak and photocatalytic activity of the catalysts were influenced to some extent by the length of the UV irradiation period. Collisions between particles in the reaction vessel over time would also promote the coalescence of Pd growth centres, which would in turn affect the physical properties of the catalyst. Clearly this step is less controllable for powered photocatalysts in suspension and may account for some slight deviations found within the data.

It should be noted that photocatalysts were also synthesised at higher and lower concentrations of Pd than the amounts tested, as well as using UV irradiation for longer periods of time. However, no beneficial effect was observed and the photocatalytic activity of the samples was lower than those of G3. A full list of the synthesised catalysts can be found in Appendix D.

The most active photocatalyst in terms of the photodecolourisation of RhB was found to be AL109. Out of test parameters investigated, the combination of Pd concentration, UV irradiation time, solution volume and irradiance value at the specifications used for this sample resulted in a highly active photocatalyst in experiments measuring the photodecolourisation of RhB.

Subsequent investigations into the photocatalytic activity of the Pd:TiO_2 photocatalysts were carried out using this catalyst. Unless otherwise stated, references to Pd:TiO_2 photocatalysts in the context of those prepared by the author will refer to samples synthesised according to the specific synthesis procedure of AL109.

5 The photocatalytic activity of Pd:TiO_2 in the degradation of rhodamine b dye

The photochemical reduction of metals onto the surface of TiO_2 has been shown to alter the physical properties of the photocatalyst where improvements in the inhibition of charge carrier recombination, as well as an increase in the optical response into the visible region have been reported.[17,98] Changes in the metal loading, the distribution and size of the metal nanoparticles, were shown in the previous chapter to affect the reactivity of the photocatalyst. This chapter investigates the effect of the reaction conditions on the photocatalytic activity of the Pd:TiO_2 catalyst. In the photodecolourisation of RhB dye, the influence of the change in initial dye concentration, the catalyst loading and of pH on the reaction rate is investigated. The LSPR effect of the Pd nanoparticles is also investigated under visible and UV light irradiation where the increase in activity is described in terms of the Pd plasmons. The recyclability of the catalyst in dye degradation is also tested.

5.1 Effect of dye concentration

The change in the photodecolourisation rate of RhB as a function of its initial concentration (C_0) was investigated. The experiment was carried out by increasing C_0 for each test in incremental steps of 10 ppm up to 50 ppm and also at a concentration of 100 ppm. This was done to probe the effects of the drastic increase on the rate of reaction. Each experiment was allowed to run for a maximum of 10 min with aliquots taken every min for UV-vis analysis in order to monitor the decrease in dye concentration (C) over time. The results of the decolourisation reactions are shown in Figure 5.1.

The results show that the photodecolourisation rate of the dye is affected by the C_0 value. It was observed that as C_0 increases, the rate of photodecolourisation of dye decreases. This is illustrated by a change in the decay curve profiles as shown in Figure 5.1 where the $t_{1/2}$ value is observed to increase with increasing C_0.

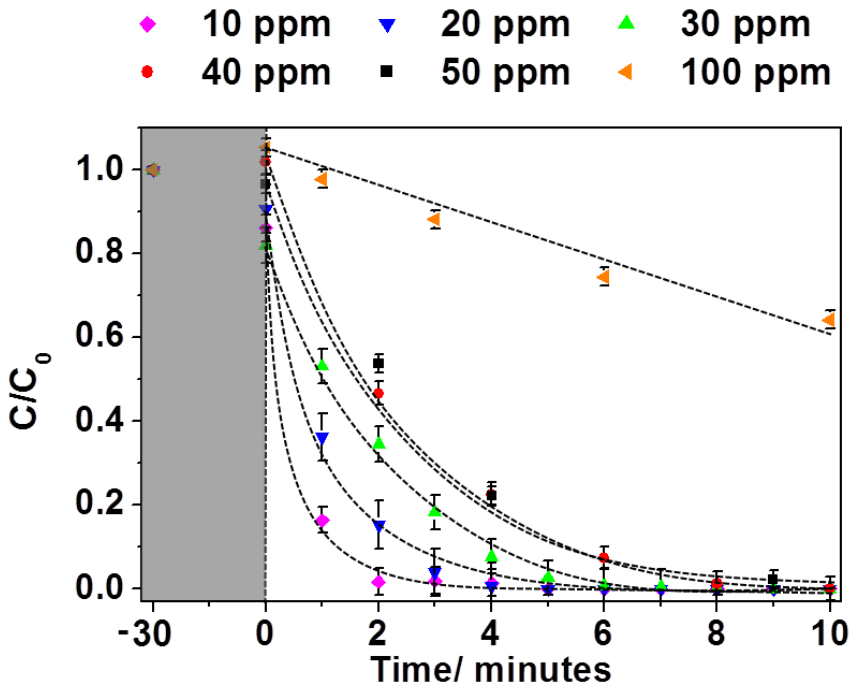

Figure 5.1 The normalised decolourisation curves of RhB at different initial dye concentrations are shown.

At lower concentrations (< 30 ppm) the reaction rate can be described by pseudo-first order decay kinetics where the rate is dependent on the initial concentration RhB. However, as the concentration of RhB increases, the reaction rate approaches zero order where at 100 ppm the degradation curve resembles a linear decay where the C/C_0 value is proportional to the time of reaction. At this concentration the surface of the photocatalyst will be almost saturated by the adsorbed RhB molecules. The rate of reaction at concentrations higher than 100 ppm are less dependent on the concentration of dye and at the point of catalyst surface saturation, the reaction rate

will follow zero order kinetics. There is a point at which the reaction rate changes depending on the concentration of dye in the solution. This effect is more clearly demonstrated in terms of the reaction constant, k_{app} as shown in Figure 5.2.

Table 5.1 Summary of the effect of RhB concentration on the photocatalytic activity of the Pd:TiO_2 catalyst in terms of the k_{app} and $t_{1/2}$ values.

Dye concentration/ ppm	100	50	40	30	20	10
k_{app}/ min^{-1}	0.059	0.353	0.417	0.476	0.989	1.899
$t_{1/2}$/ min	11.83	1.96	1.66	1.46	0.70	0.36

The rate of change of k_{app}, which can be taken as the slope of the straight line in Figure 5.2, was shown to decrease with increasing dye concentration and is consistent with the increase in the value of the associated $t_{1/2}$.

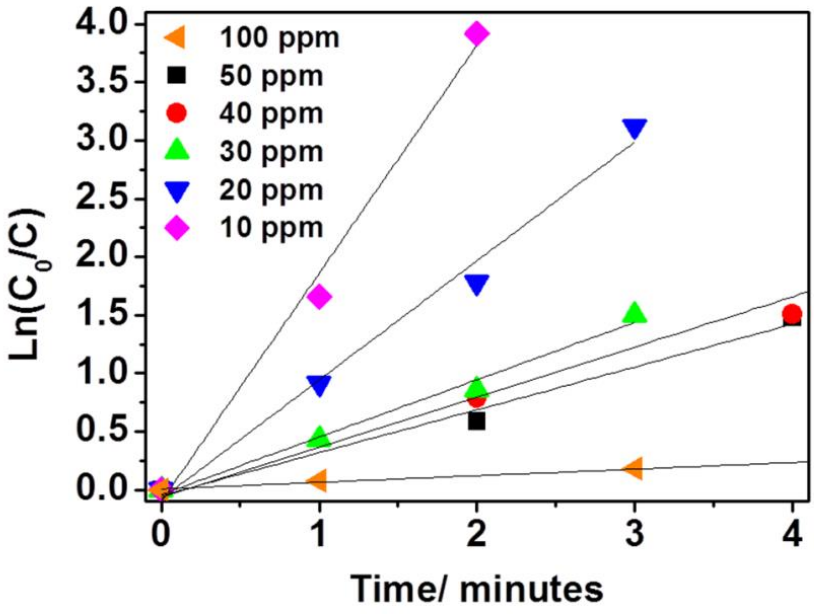

Figure 5.2 The rate constant of the decolourisation of RhB is the slope of the straight line of natural logarithm of the reciprocal of the normalised decolourisation values against time

It was observed that the largest difference in the k_{app} values occur between the concentrations of 10 ppm, 20 ppm and 30 ppm. At these concentrations the k_{app} values effectively halve with each successive increase in concentration. However, at 30 ppm, the change in k_{app} between higher concentrations decreases significantly, such that between concentration values of 30 ppm, 40 ppm and 50 ppm, the difference between the rate constants is an average of 0.06 min^{-1}.

These results suggest that there is a point at which the activity of the catalyst is less dependent on the C_0 value of dye. This is observed to occur at concentrations > 30 ppm as shown in Figure 5.3.

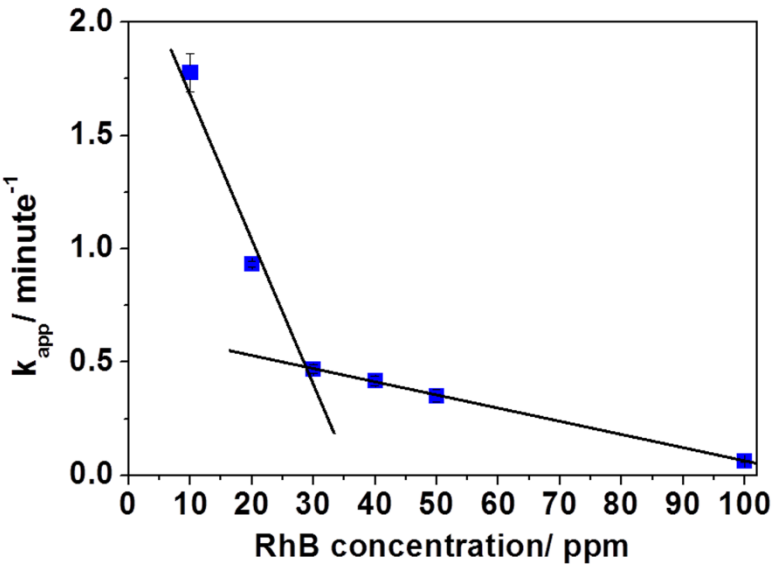

Figure 5.3 The dependence of the rate of photodecolourisation on the initial dye concentration

Figure 5.3 shows two distinct reaction rates for the decolourisation of dye as a function of C_0. For C_0 values up to 30 ppm the kinetics of the reaction are relatively low compared to the rate at C_0 values above 30 ppm. There are two main reasons for this change in the value of the reaction rate:

1. As the dye absorbs at 554 nm, the increase in its concentration in the solution will result in a decrease in optical path length of incident photons that will affect the absorption of photons by the catalyst.
2. As the surface of the catalyst becomes saturated in adsorbed dye molecules, the reaction will assume pseudo-zero order kinetics where the photodegradation rate of dye will be independent of its initial concentration and proportional to the time of reaction.

The interesting feature of this analysis is the point at which the difference in the k_{app} value changes significantly relative to the initial concentration RhB. This was identified to be at a concentration of 30 ppm. This was found to be the critical point where the concentration of dye begins to significantly affect the photocatalytic activity of the catalyst by reducing the photon path length within the solution, thus limiting reactions to the catalyst at the surface of the solution. At the same time, the catalyst surface approaches saturation with increasing C_0 and the reaction starts to become proportional to the time of reaction.

This investigation showed that the C_0 value of dye influences the photodecolourisation reaction rate up to a point. It was found that higher levels of the initial dye concentration results in a negative change in the rate of photodecolourisation from pseudo-first order to zero order kinetics. The critical point at which the rate of the reaction changes was observed to be at a dye concentration of 30 mg/L. RhB concentrations below this value showed first order reaction kinetics, while concentration values above were shown to approach zero order kinetics with increasing concentration.

5.2 Catalyst loading dependence

The catalyst loading was varied from 1 g/L to 7 g/L to investigate the effect on the rate of decolourisation of dye. The conditions for the experiments were maintained at 50 mL of 10 ppm RhB solution and irradiation equivalent to 1 Sun at 100 mW/cm^2 and AM 1.5. An adsorption/desorption equilibrium time of 30 min for each of the experiments was allowed prior to irradiation. The results of the photodecolourisation at the different loading levels are shown in Figure 5.4 in terms of the rate constant.

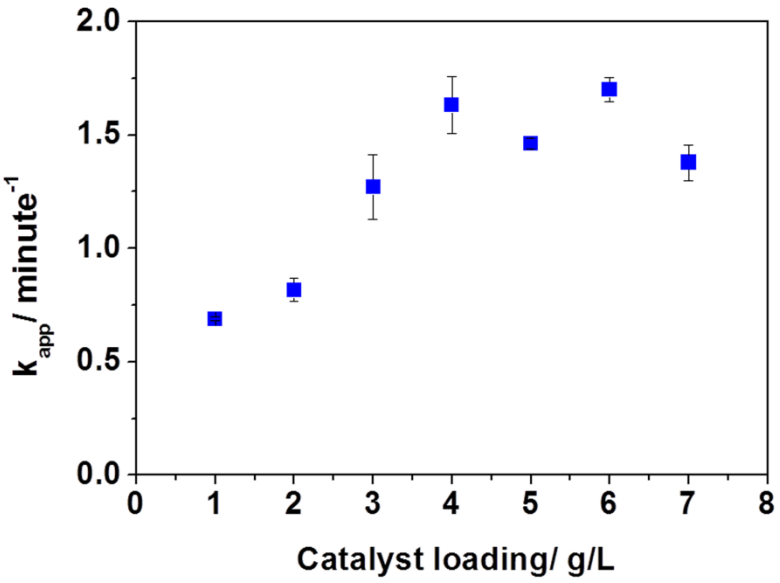

Figure 5.4 Photodecolourisation reaction rate constant as a function of the catalyst loading under simulated solar irradiation

Table 5.2 The reaction rate constant and half-life of photodecolourisation values at different catalyst loadings

Catalyst loading/ mg	**350**	**300**	**250**	**200**	**150**	**100**	**50**
k/ min^{-1}	1.389	1.700	1.462	1.632	1.272	0.817	0.690
$t_{1/2}$/ min	0.45	0.40	0.45	0.37	0.52	0.84	1.03

The results showed that an increase in the level of catalyst loading was found to rapidly increase the rate of photodecolourisation up to a maximum value of 4 g/L. Catalyst loadings at levels greater than this were observed to maintain this rate of photodecolourisation as shown in Figure 5.4. It could also be argued that the photocatalytic activity was found to decrease at higher loading levels however, further tests using higher catalyst loading levels would be required to confirm this. Either way, a balance clearly exists between the number of available active sites and the absorption of photons by the catalyst.

The loading dependence of the catalyst can be explained by considering that as the amount of catalyst in the solution increases, as does the number of available active sites for photon absorption and dye adsorption, resulting in an increase in the rate of reaction as observed in Figure 5.4. However, above a loading of 4 g/L, as in the case of Pd:TiO_2, the amount of catalyst in solution becomes so high that the opacity of the solution increases, as does the scattering of photons, which prevents the transmission of the photons through the solution and impedes further absorption of photons by the catalyst. It is a screening effect by the catalyst. Another reason for the levelling off of the reaction rate at higher catalyst loading levels is the agglomeration and sedimentation of catalyst, which will be significant and affects the efficiency of the reaction.

The optimum loading of Pd:TiO_2 was found to be 4 g/L in dye photodecolourisation experiments. However, the loading level used throughout this study was fixed at 2 g/L. This amount was chosen as it is similar to the value used in a wide range of publications,[15,59,80,104,106,218–220] which makes direct comparison of results more practical.

Another motivation for using the value of 2 g/L is the need to try and establish a standardised procedure for photocatalytic reactions. There has previously been a call to standardise experimental procedures of photocatalytic reactions for particulate photocatalysts in order to more easily compare results between research groups.[221] This would be a sensible approach to presenting the results, allowing for easier direct comparison with other research.

5.3 Effect of pH on the decolourisation reaction rate

The pH of the dye solution was altered from 2 to 12 in separate experiments using HCl or NaOH to determine the influence of the reaction pH on the photocatalytic activity of the catalyst. It is known that for particulate TiO_2 samples, the pH determines the surface charge of the catalyst which in turn affects the adsorption properties of chemical species in the solution.[18]

An important parameter in determining the surface charge properties of TiO_2 is its isoelectric point (IEP). The IEP is the value of the pH of the solution at which the zeta potential of the catalyst equals zero. In aqueous suspensions the surface of TiO_2 is largely covered by hydroxyl groups as shown in Equation 5.1 where the ionisation state of its surface can be altered under acidic or basic conditions as shown in Equations 5.2 and 5.3, respectively.

$$Ti^{4+} + H_2O \rightarrow Ti^{4+}OH + H^+ \quad \textbf{(5.1)}$$

$$TiOH + H^+ \rightarrow TiOH^{2+} \quad \textbf{(5.2)}$$

$$TiOH + OH^- \rightarrow TiO^- + H_2O \quad \textbf{(5.3)}$$

P25 is reported to have an IEP approximately at pH 6.[222] This means that in acidic solutions the surface will be positively charged, whereas in basic conditions its surface

will be negatively charged. As the metal loading of the Pd:TiO_2 is low (approximately 0.5 wt%), the IEP of the catalyst surface was assumed to be the same as that of P25. The adsorption behaviour of RhB on the catalyst is thus expected to depend on the ionisation state of the catalyst under different pH values as described above.

The dye adsorption to the catalyst surface was monitored for each experiment at a range of pH values, Figure 5.5.

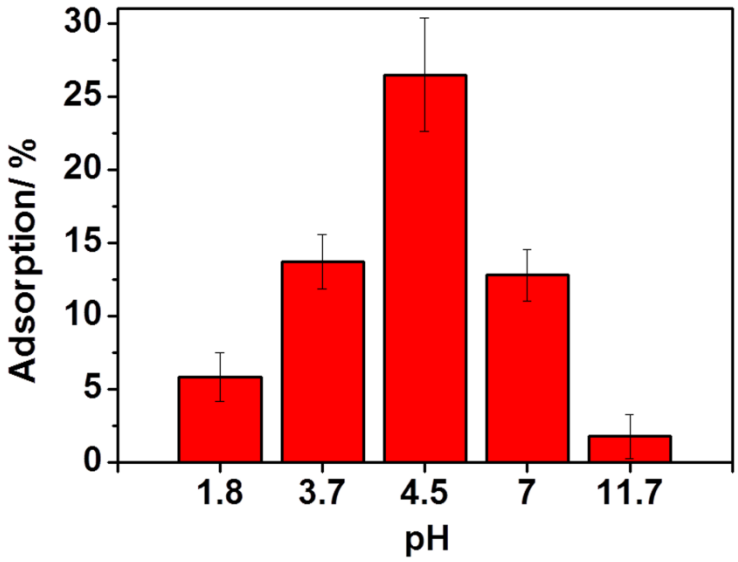

Figure 5.5 Percentage of RhB adsorption to the catalyst surface as a function of pH is shown. The adsorption/ desorption equilibrium period of stirring in the dark was 30 min

The study found the highest value of dye adsorption to be centred at a pH of 4.5 and was observed to decrease in lower, as well as higher pH values. According to the IEP of the photocatalyst and ionisation state of RhB, which is reported to be cationic, the adsorption coefficient is expected to increase as the solution tends to become more alkaline, if electrostatic considerations are taken into account. However, this straightforward dependence was not observed in this case. The reason for the measured

adsorption behaviour of RhB is likely to be the relation between its ionisation state and pH of the solution.

RhB has ionisable functional groups such that under acidic conditions at pH < 4, it is largely in its cationic form.[223] This suggests that Coulombic forces between the photocatalyst surface and the dye will produce a repulsive effect since the surface of the catalyst will have a net positive charge. It follows that the adsorption of dye to the catalyst will be relatively low under these conditions.

At pH > 4, RhB is mainly in the form of a zwitterion.[224] At these mildly acidic conditions, the adsorption of dye will likely be favoured due to the relatively low repulsive Coulombic forces in play. This could explain the high adsorption at a pH = 4.5 in Figure 5.5.

As the solution becomes more alkaline, the surface charge of the photocatalyst becomes more negative and this would result in a decrease in adsorption of dye, again due to Coulombic repulsion.

The photodecolourisation kinetics of dyes are known to be closely related to the surface adsorption coefficient, as the degradation reactions are thought to occur between adsorbed molecules and the surface of the semiconductor.[222] The rate of degradation of dye should then be dependent on the adsorption percentage of dye on the catalyst surface and therefore, directly related to the pH of the solution. The results of the degradation of RhB at different pH values are presented in Table 5.3 and the decolourisation profiles are shown in Figure 5.6

Table 5.3 Results of photodecolourisation of RhB under different pH conditions

pH	**1.8**	**3.7**	**4.5**	**7**	**11.7**
k_{app}/ min^{-1}	5.713	1.803	1.082	0.166	0.046
$t_{1/2}$/ min	0.12	0.38	0.64	4.18	15.07
Adsorption/ %	5.9	13.7	26.5	12.8	1.8

Figure 5.6 shows that there is a strong dependence between the value of the pH and the rate of RhB decolourisation such that the rate at pH 1.8 > pH 4.5 > pH 11.7. While the rate of reaction increased with increasing acidity of the solution, there did not appear to be a direct correlation between the adsorption of dye and the reaction rate.

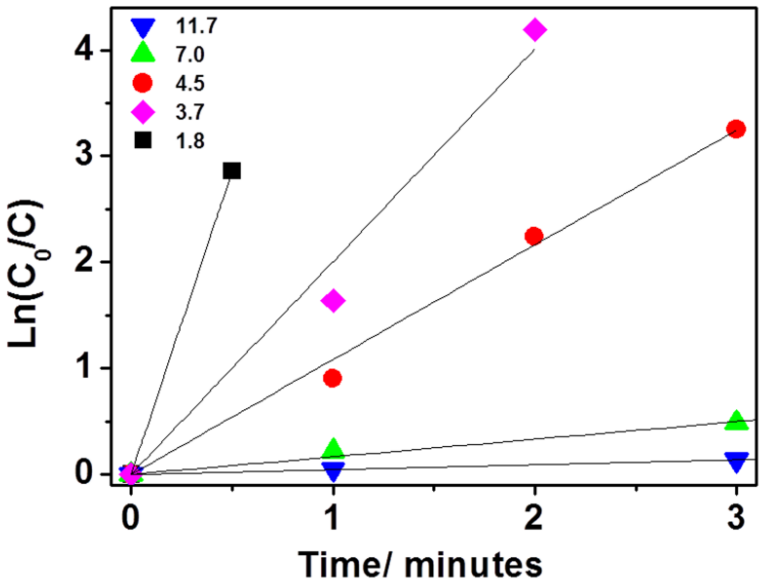

Figure 5.6 The photodecolourisation rate of RhB under different pH values is shown

This indicates that the adsorption of dye is not the rate determining step for this reaction, as the maximum rate of decolourisation did not correspond to the level of pH that showed the highest adsorption of dye. It follows that the photocatalytic

decolourisation reactions are not only limited to the surface of the catalyst but also occur in close proximity to its surface.

The main mechanism for the photocatalytic degradation of dye in the presence of TiO_2 relies on the reaction of free radicals initiated by irradiation of light on the catalyst surface. The photogenerated holes are highly oxidising species that can either directly oxidise the dye molecules or react with adsorbed hydroxide ions to form hydroxyl radicals, which go on to react with the dye molecules. At low pH values, the photogenerated holes are thought to be the predominant oxidative species, although electrons may also play an important role in the degradation reactions. At high pH the hydroxyl radicals are thought to be the main species responsible for the degradation.[155,177]

The decrease in the photodegradation efficiency of the catalyst observed in increasing alkaline conditions may be due to the Coulombic repulsion between the negatively charged catalyst surface and the hydroxide ions inhibiting the formation of the reactive hydroxyl radicals. Also, hydroxyl radicals are quickly scavenged by the photogenerated holes under these conditions and do not have the opportunity to react with the dye molecules. Both of these processes are thought to be contributing to the decrease in the rate of photodecolourisation under increasing basic conditions.[155]

The increase in activity of the photocatalyst as a function of decreasing pH in the degradation of dyes has been reported[103,225] and a number of factors may contribute to this observation. These include the pH dependence of the target compound, the ionisation states and properties of intermediary products, and the surface properties of the catalyst. The degradation pathway of the dye is likely affected by these parameters

leading to a number of possible complex mechanisms. This study found that for this particular combination of dye and photocatalyst, the optimal conditions for decolourisation were under acidic conditions. The effect of pH on the rate of reaction was found to be dependent not only on the surface properties of the catalyst but also on the nature of the target compound. Therefore, the effect of pH on these parameters should be thoroughly investigated in order to improve the photocatalytic efficiency of a given system.

5.4 Effect of UV and visible light irradiation

Optical filters were used in separate tests to inhibit regions of the spectrum in dye decolourisation reactions. The use of the filters was important because the band structure of TiO_2 is only photoactive under UV irradiation. If the photodecolourisation of the dye were to progress in the absence of UV irradiation, this would support the evidence in favour of the visible light enhancing properties of the supported Pd nanoparticles playing an important role in the reaction.

In order to investigate the effect of this improvement in the optical response, RhB photodecolourisation experiments were carried out using optical filters to block irradiation at $\lambda > 400$ nm (VIS block) and also at $\lambda < 400$ nm (UV block). The output of the solar simulator was adjusted to compensate for the loss of light transmission due to the use of the filters and ensured that the irradiance values for the transmitted regions were the same as when no filter was used.

The altered optical response profile of the Pd:TiO_2 catalyst represents a significant change to the photoactive properties of TiO_2; both in terms of the increase in visible light absorption and in the difference in the band gap. The results of the

photodecolourisation experiments show that these changes correspond to an increase in the photocatalytic activity of the new catalyst. It was observed that compared with TiO_2, the decolourisation rate of RhB in the presence of Pd:TiO_2 under solar conditions increased by a factor of 19. The photodecolourisation rates of RhB in the presence of TiO_2, and the new catalyst under different irradiation conditions are shown in Table 5.4. The $t_{1/2}$ value of RhB was observed to be lowest when no optical filter was used. Under visible light irradiation, the decolourisation rate of TiO_2 was the slowest of all the tested conditions and this was attributed to its deactivation since it is only active under UV irradiation.

Table 5.4 Catalytic activity under irradiation from different regions of the EM specrtrum

Photocatalyst	Filter used	$t_{1/2}$/ min	k_{app}/ min^{-1}
TiO_2	No filter	9.4	0.073
	VIS block	19.3	0.04
	UV block	63.6	0.011
Pd-TiO_2	No filter	0.5	1.410
	VIS block	3.1	0.226
	UV block	8.5	0.078

The decolourisation of RhB in the presence of Pd:TiO_2 was also reduced under visible light conditions however, there was still a significant activity associated with the catalyst under these conditions.

The RhB photodecolourisation rate under UV irradiation for both catalysts was found to be at an intermediate rate between full irradiation and visible irradiation only. The presence of the Pd nanoparticles was shown to increase the light harvesting potential of the catalyst and it is thought that the LSPR effect is responsible for the observed activity under visible light irradiation.

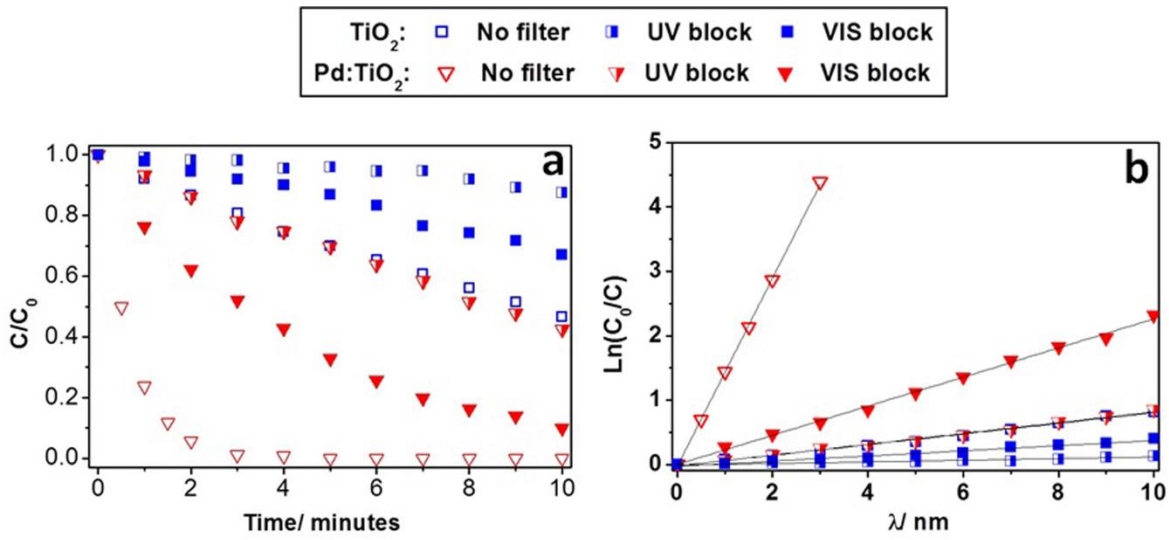

Figure 5.7 Photodecolourisation profile of RhB under different optical ranges in the presence of TiO_2 and Pd:TiO_2

In order to more easily visualise and understand the nature of the redox mechanisms occurring under different irradiation conditions, it is useful to separate each experiment in terms of the region of the spectrum that is being investigated. The results of the experiments, coupled with the spectrographic data obtained for the catalysts, help to explain the process responsible for the increase in activity of the catalyst. This process can be understood in terms of the LSPR of the Pd nanoparticles.

5.4.1 LSPR effect on the increased photocatalytic activity of Pd:TiO_2

To investigate the increase in activity of the new catalyst it is important to consider the different processes that are occurring under the different irradiation conditions. It will then be possible to determine the mechanism for each condition separately.

The formation of the Schottky barrier at the metal-support interface is a parameter that indicates whether the metal nanoparticle can inhibit the recombination of excited charge carriers by acting as an electron trap. The barrier height, Φ_B was calculated using Equation 2.4. The Φ_M of Pd used was 5.22 eV,[226] the χ of TiO_2 was estimated to be 4.21 eV[227,228] and so the Φ_B was calculated to be 1.01 eV (Figure 5.8). This value shows that

the Pd can effectively act as an electron trap site and reduce the recombination of charge carriers.

As well as acting as trap sites, the metallic nanoparticles can potentially be the source of hot carriers due to LSPR effects, which also increase the optical response of the semiconductor. The decay of plasmons can occur radiatively via emission of photons or non-radiatively through the generation of excited carriers known as hot carriers.

The hot carriers can be transferred to the semiconductor and drive redox reactions with adsorbed species on the surface, providing they have sufficient energy to overcome the Schottky barrier at the metal-support interface. This process can also increase the rate of reactions taking place on the surface of the catalyst.

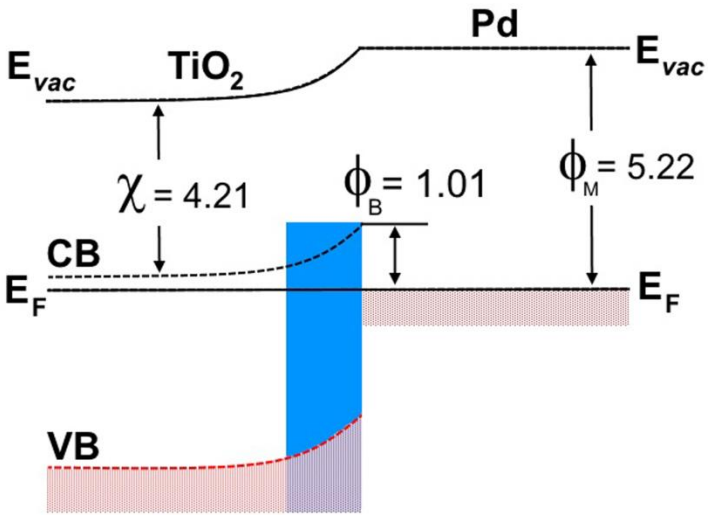

Figure 5.8 Schottky barrier formed at the inerface of the TiO_2 with a Pd nanoparticle. The barrier height, work function of Pd and the electron affinity of TiO_2 are given in terms of the vacuum energy and Femi level

Palladium nanostructures are known to exhibit LSPR at λ_{peak} above 300 nm for nanoparticles larger than 10 nm.[229] Below this value, unsupported Pd is not thought to exhibit LSPR above 300 nm. However, the LSPR properties of Pd are not as well

documented as that of Au and Ag. Also, the effect of the metal support interaction on the LSPR of Pd, as far as the author is aware, has not yet been reported.

It has been shown with Ag nanoparticles for example, that the substrate effects of supported plasmonic nanoparticles can significantly influence the plasmonic properties of the metal nanoparticle.[60] Kelly et al. found that the LSPR of Ag nanostructures are proportional to the index of refraction of the substrate and can exhibit a red-shift of up to 100 nm. This phenomenon has not been reported in the case of Pd but this process is believed to occur for the supported Pd nanoparticles on the TiO_2 substrate. This mechanism can explain the increase in activity of the Pd:TiO_2 catalyst in the degradation of RhB.

5.4.2 Visible light irradiation

Under visible light irradiation, charge separation in the TiO_2 support cannot occur since super band gap photons are not being transmitted due to the UV blocking optical filter. Figure 5.9a confirms that the absorption onset of TiO_2 is located in the UV region of the spectrum where the irradiation has been impeded. In these conditions, the decolourisation rate of RhB in the presence of TiO_2 was found to be the same as in the control test where RhB was irradiated under full solar light in the absence of catalyst. In the presence of the Pd:TiO_2, the decolourisation of RhB was observed at a rate comparable to that of untreated TiO_2 under full solar irradiation (Table 5.4). The increased activity of the Pd:TiO_2 catalyst is attributed to the LSPR effect of supported Pd nanoparticles. This effect is thought to be responsible for the change in the absorption profile of the new catalyst as shown in Figure 5.9a, where the increase in visible light absorption is due to the λ_{peak} of the Pd plasmon.

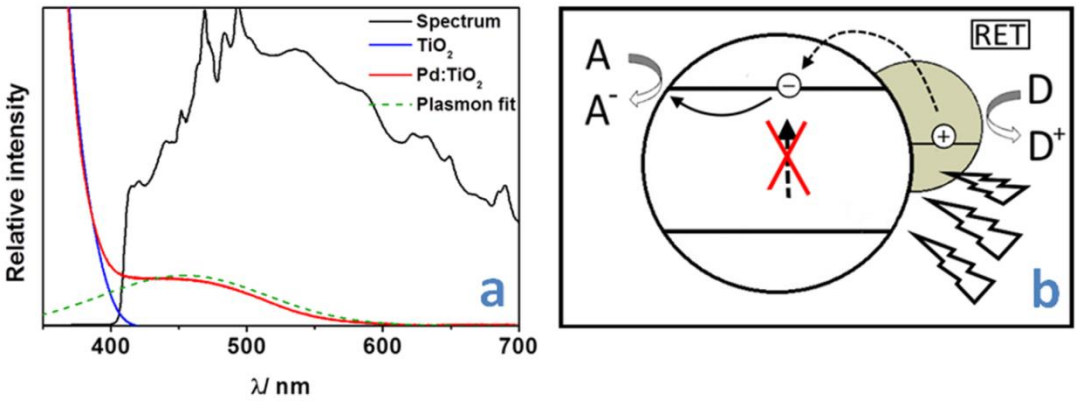

Figure 5.9 The absorption of P25 and the new catalyst is shown against the UV blocking filter profile a) the proposed mechanism responsible for the increase in activity of the catalyst under visible light irradiation b)

The decolourisation of RhB under visible light conditions is due to the transfer of hot electrons from the Pd nanoparticles to the TiO_2 via the non-radiative decay of the plasmon as shown in Figure 5.9b. Hot electrons which possess sufficient energy to overcome the Schottky barrier can transfer to the conduction band of TiO_2 where the reduction reactions occur, while the hot holes remaining in the Pd nanoparticle can react with adsorbed molecules in oxidation reactions.

5.4.3 UV light irradiation

In the case of UV light irradiation only, TiO_2 is photoactive and can absorb the super band gap photons to generate the excited charge carriers and participate in the decolourisation of dye. The rate of the decolourisation of RhB in the presence of TiO_2 was expected to be the same as for the same reaction under full irradiation.

However, the visible light cut-off point of the optical filter was found to block a significant proportion of the UV spectrum beyond the onset of absorption of TiO_2 (Figure 5.10a). Due to this effect, a corresponding reduction in reaction rate was observed.

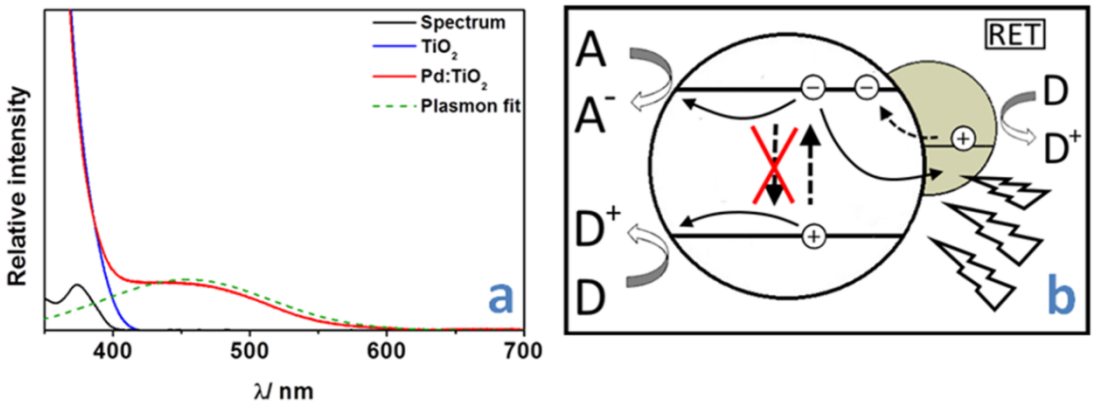

Figure 5.10 Absorption of P25 and Pd:TiO_2 is shown against the profile of the visible light blocking filter a) the proposed mechanism responsible for the increase in activity of the catalyst under UV light irradiation b)

The power output of the solar simulator was adjusted to match the output of this region under full irradiation but this could not be achieved at the highest power setting. Figure 5.10a illustrates this; it shows the onset of photon absorption of TiO_2 and the Pd:TiO_2 catalysts, which are represented by a sharp increase in absorption at approximately 410 nm versus the incident spectrum. There is a region between the onset of absorption and the incident irradiation that was blocked by the UV blocking filter and hence some super band gap photons were not transmitted and absorbed. The result of this was a 51% decrease in activity for TiO_2 under UV irradiation only, compared with its activity under full solar irradiation.

The decolourisation rate of RhB in the presence of Pd:TiO_2 comprised a 6 fold increase in activity compared with TiO_2 under the same conditions. Under UV irradiation, the Pd nanoparticles can act as an electron trap site preventing the recombination of excited charge carriers generated in the TiO_2. Furthermore, the Pd plasmon is shown to extend into the UV range indicating that hot electron transfer also occurs. Both these processes

can occur simultaneously under UV irradiation and increase the activity of the Pd:TiO_2 catalyst (Figure 5.10b).

5.4.4 Full spectrum irradiation

Under full solar irradiation the two mechanisms described are occurring simultaneously under visible light and UV irradiation. The increase in activity of the Pd:TiO_2 catalyst compared with TiO_2 under these conditions was a factor of 19. This enhancement is attributed to the presence of the supported Pd nanoparticles and the observed LSPR effect, which increased the light harvesting capability of the catalyst into the visible region where a significant level of activity in the decolourisation of RhB was observed. The position of the Pd plasmon is such that its influence on the catalytic activity of the Pd:TiO_2 catalyst is not confined only to the visible region; an increase in the activity of the catalyst was also observed under UV irradiation compared with TiO_2.

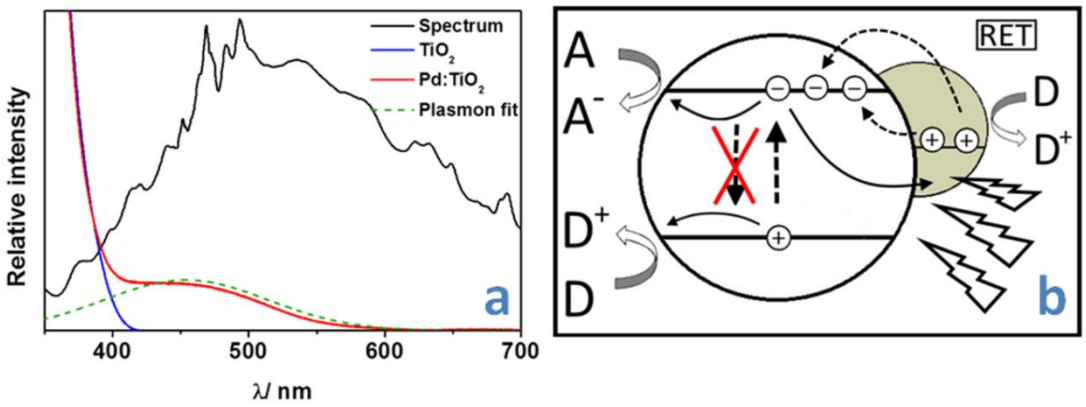

Figure 5.11 The absorption of P25 and Pd:TiO_2 is shown against the profile of full solar light irradiation a) the proposed mechanism responsible for the increase in activity of the catalyst under solar irradiation b)

It is the combination of the interaction of plasmonic effects of the Pd nanoparticles with the TiO_2 under UV and visible light irradiation, coupled with the activity of TiO_2 under

UV irradiation, that are thought to be the mechanisms responsible for the increase in activity of Pd:TiO_2.

5.5 Recyclability

The Pd:TiO_2 catalyst was tested in several runs to determine its recyclability. Tests were carried out using 300 ml of 10 ppm RhB and a catalyst loading of 2 g/L. The pH of the solution was maintained at a value of 1.8, which was the pH at which the highest photocatalytic activity was observed.

Five runs were carried out where 30 min of adsorption/desorption equilibrium was allowed prior to turning on irradiation. Each cycle comprised an irradiation time of 60 min. As the $t_{1/2}$ value for one cycle of Pd:TiO_2 was 0.5 min, 60 min was thought to be a sufficient period of time to allow for the complete decolourisation of the dye for each run. After this period the water level in the reactor was refilled to 300 ml and the dye concentration was replenished to 10 ppm.

The first 10 min of irradiation was monitored and aliquots were taken at 1 min intervals to determine the activity of the catalyst by comparing the $t_{1/2}$ and k_{app} value for each run. Figure 5.12 shows the first 10 min of 5 cycles using the same Pd:TiO_2 catalyst. Table 5.4 gives the $t_{1/2}$ and k_{app} values for each run.

Figure 5.12 shows the normalised photodecolourisation profiles of the 5 separate runs of the experiment. The activity of the catalyst in terms of the $t_{1/2}$ was found to increase with each successive run from 0.97 min for the first cycle to 5.03 min for the fifth cycle. The decrease in activity for the catalyst is also shown in terms of the k_{app} value in Figure 5.13.

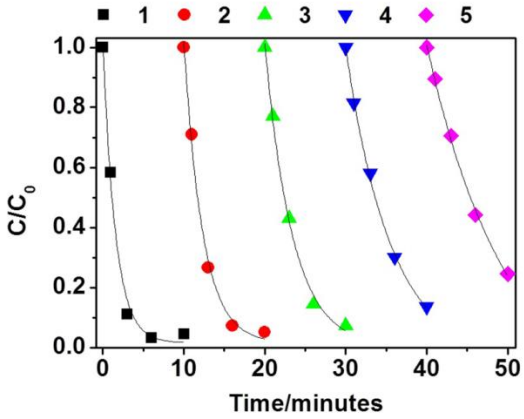

Figure 5.12 The normalised decay curves for the decolourisation of RhB for different irradiation cycles are shown. The recyclability of the Pd:TiO2 catalyst was tested in 5 separate decolourisation cycles where the first 10 min of each cycle were monitored by taking aliquots at determined time intervals. This 10 min period was used to calculate the t1/2 and kapp values from which the activity of the catalyst could be compared for each separate run

Table 5.5 Rate constant and $t_{1/2}$ values per reaction cyle

Cycle	1	2	3	4	5
k_{app}/ minute^{-1}	0.713	0.431	0.313	0.198	0.138
$t_{1/2}$/ minutes	0.97	1.61	2.215	3.50	5.03

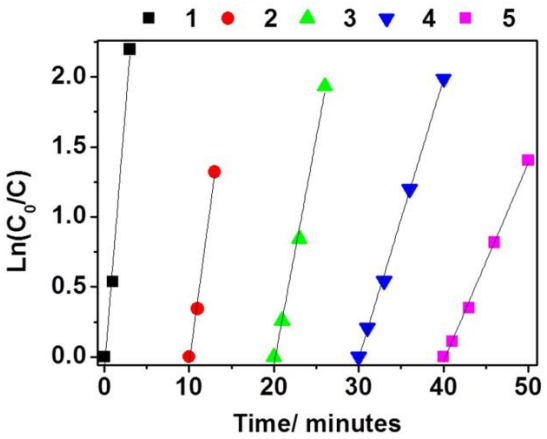

Figure 5.13 The k_{app} values obtained from the photodecolourisation of RhB curves show a reduction in activity over time for the catalyst.

The reason for the reduction in activity of the catalyst is thought to be due to the loss in the active sites on the surface of the catalyst. Adsorption/desorption studies showed that 15% of the dye was chemisorbed to the surface of the catalyst during the 30 min that it was stirred in the dark. Subsequent chemisorption of dye to the catalyst in the later runs was found to be reduced compared with the first cycle as shown in Figure 5.14.

Though the first run of the photodecolourisation experiment shows the fastest rate of decay of RhB, subsequent cycles exhibit a progressive loss in activity and in adsorption of dye to the catalyst surface. It was also observed that the surface of the catalyst grew darker with each successive addition of dye. This suggests that the chemisorbed dye molecules may not have been completely decomposed after the 60 min irradiation time whereby the remaining adsorbed species could be blocking active sites of the catalyst.

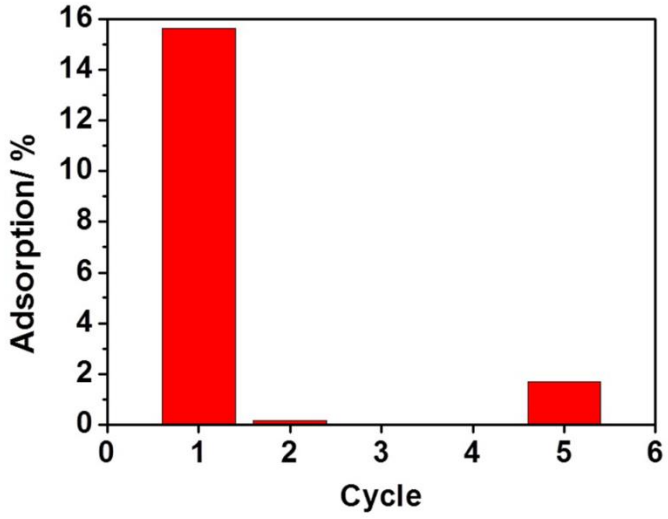

Figure 5.14 Adsorption of dye to the catalyst surface drastically decreases after the first cycle suggesting the dye has not been completely decomposed and remains on the surface after the experimental period thus preventing the same level of adsorption of dye in subsequent runs.

The accumulation of the adsorbed species progressively reduces the number of available active sites on the surface of the catalyst and therefore decreases its activity with each run. Several attempts were made to restore the activity of the catalyst back to its initial value by washing it with solvents such as acetone and ethanol. This was done to try and remove adsorbed species from its surface however, every attempt failed to re-activate the catalyst to its initial level of activity. It is also possible that reaction intermediates accumulated in the reaction vessel during the test. The degradation of dye was measured only via the destruction of the chromophore and so the build-up of intermediate compounds in the reaction vessel over time would reduce the activity of the photocatalyst to a pseudo-zero order reaction rate. This process coupled with the deactivation of active sites on the surface of the catalyst will significantly reduce the activity of the catalyst over time.

5.6 Summary

This chapter has outlined the investigation into the photodecolourisation of RhB dye using the Pd modified TiO_2 catalyst synthesised according to the procedure described in chapter 4. The previous chapter dealt with the synthesis of the catalysts and used the results of dye degradation experiments as a parameter to optimise the synthesis procedure in order to improve the photocatalytic activity. This chapter has taken the most efficient photocatalyst synthesised, in terms of the fastest half-life of decolourisation, and investigated the effects of the initial dye concentration, the catalyst loading, pH dependence, UV/ visible irradiation and recyclability on the rate of reaction. It was found that the initial dye concentration influenced the rate of reaction such that increasing the concentration of dye slows its rate of photodecolourisation. The change

in the reaction rate was more pronounced at lower concentrations of dye while at higher concentrations it was found that saturation of the surface of the catalyst with dye molecules and the reduction in optical path length of the photons reduced the rate of reaction considerably. At high concentrations, the reaction was thought to be following pseudo-zero order kinetics.

The catalyst loading was also observed to affect the rate of reaction up to an optimum value of 4 g/L. Beyond this point it is thought that the shielding of photons coupled with the agglomeration and settling of the catalyst reduced the photocatalytic efficiency of the reaction.

The pH dependence of the reaction was such that the reaction rate at pH 1.8 > pH 11. As the dye and catalyst surface are dependent on the pH, complex surface interactions and electrostatic forces determine the adsorption of dye and no direct correlation between the adsorption and photocatalytic activity was found.

The increase in activity of the catalyst was thought to be due to the LSPR of Pd, which was investigated using optical band pass filters. UV-vis analysis measured an increase of 10% in light harvesting capability which is thought to be a contributing factor to the increase in activity of the catalyst.

By using optical band pass filters to block UV or visible light during photodecolourisation experiments on RhB, an increase in activity for the Pd:TiO_2 photocatalyst was observed under all test conditions relative to TiO_2. Under solar conditions the activity of the synthesised catalyst was found to be a 19 fold improvement on the activity of commercially available TiO_2.

The recyclability of the catalyst was investigated and it was found that RhB strongly adsorbs to the photocatalyst surface such that at the time scales tested, it was not possible to completely mineralise the dye between each decolourisation cycle. This had the effect of reducing the activity of the catalyst with each successive run. Efforts were made to desorb the dye from the catalyst through immersing the catalyst in different solvents but it was not possible to restore the photocatalytic activity of catalyst to its initial value using this method. As such, it is recommended the reaction be maintained for a longer period of time to ensure complete mineralisation of the dye and avoid the build-up of reaction intermediates on the surface of the catalyst.

6 Hydrogen generation from TiO_2 supported Pd and RuO_2 nanoparticles

There have been studies based on the combination of Pt and RuO_2 on TiO_2 to form bimetallic heterostructured photocatalysts for the production of H_2 via the photolysis of water[127] and the reforming of biofuels such as alcohols and carbohydrates.[5,191] However, the combination of Pd and RuO_2 supported on TiO_2 reported herein is, to the best of the author's knowledge, the first reported example of solar H_2 evolution using this particular co-catalyst system and the first reported synthesis of RuO_2 nanoparticles photochemically reduced onto a TiO_2 support from a $RuCl_3$ solution. A hydrogen production rate of 5818 μmol per hour per gram of catalyst under AM 1.5 illumination for a combination of monometallic Pd:TiO_2 and RuO_2:TiO_2 has been achieved. This is a value higher than any other platinum group metal modified TiO_2 photocatalyst reported in the literature.

6.1 Pd and RuO_2 photocatalysts

Hydrogen generation experiments were carried out with four samples of catalysts, which comprised the Pd:TiO_2, the RuO_2:TiO_2, a catalyst containing a bimetallic distribution of Pd and RuO_2 nanoparticles (Pd:RuO_2:TiO_2) and a combination of the Pd:TiO_2 and RuO_2:TiO_2 catalysts. The samples were prepared via the photochemical reduction of Pd or RuO_2 from $PdCl_2$ or $RuCl_3$ as described in chapter 3. The loading of Pd on the TiO_2 support was measured at 0.5 wt% via ICP. The RuO_2 loading levels could not be determined since there was no lamp able to analyse the metal via the same ICP instrument. The theoretical maximum amount of RuO_2 that could be photochemically reduced onto the TiO_2 given the RuO_2 concentration level in the solution is 0.1 wt%

however, the actual amount is believed to be much less and is estimated at 0.025 wt% based on the values measured for the Pd:TiO_2 catalyst.

The oxidation state of the photochemically deposited Pd and Ru were analysed via XPS as shown in Figure 6.1. The chemical state of Pd was confirmed to be that of Pd^0. The binding energy values measured for the Pd:TiO_2 sample at the 3d spin orbit component region of the Pd transitions was found to correspond to that of metallic Pd. The values were measured at 334.9 eV and 340.2 eV for the $3d_{5/2}$ and $3d_{3/2}$ components.

The chemical state of the Ru nanoparticles was found to be RuO_2 based on the measured binding energy value of 280.9 eV obtained for the $3d_{5/2}$ spin orbit component, which is close to the reported value of 280.7 eV.[230] The $3d_{3/2}$ component could not be observed due to the overlap with the adventitious carbon C1s peak located at 284.7 eV as shown in Figure 6.1a.

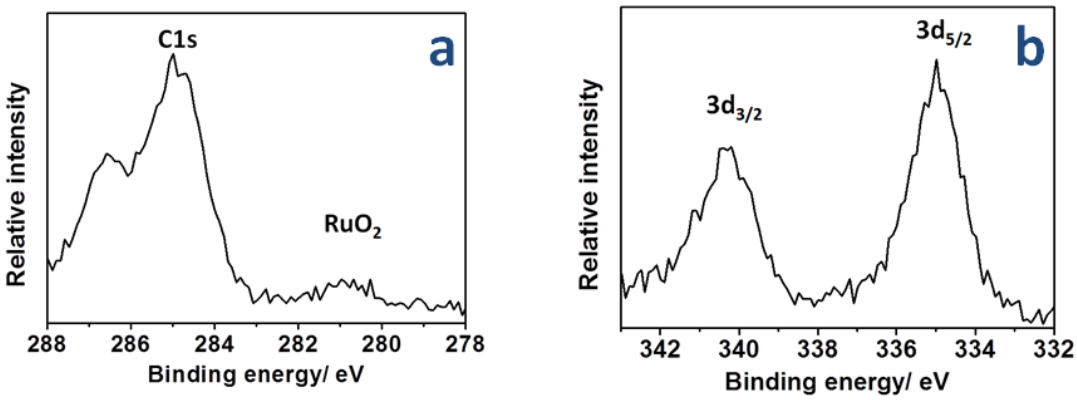

Figure 6.1 XPS analysis of the catalysts showing the binding energy values measured for the RuO_2:TiO_2 photocatalyst (a) and for the Pd:TiO_2 sample (b)

The RuO_2 peak is known to be asymmetric, with the $3d_{5/2}$ component showing a higher intensity than the $3d_{3/2}$ orbital. Furthermore, the intensity of the $3d_{5/2}$ spin orbit

component suggests an extremely low concentration of RuO_2 deposited on the TiO_2 when compared with the adventitious carbon peak.

A definite change in the morphology of the TiO_2 under UV irradiation in the presence of the $RuCl_3$ solution was observed, even though the data for the loading amount of Ru could not be obtained. However, this morphological change, coupled with the XPS results for RuO_2 adds support to the evidence for the photochemical deposition of Ru nanoparticles and their subsequent oxidation to RuO_2 via thermal treatment. Furthermore, it has been shown that the same photochemical treatment applied to a different metal salt solution, $PdCl_2$ in this case, has successfully photochemically deposited Pd nanoparticles onto TiO_2, which supports the efficacy of this technique.

Another indicator for the presence of RuO_2 on the surface of TiO_2 is given by the results of the TEM analysis, where the catalysts were characterised via TEM to determine the size, morphology and distribution of the photodeposited metal nanoparticles. The micrographs are shown in Figure 6.2. The morphology of the RuO_2:TiO_2 catalyst in Figure 6.2c is clearly different from that of the unmodified TiO_2 shown in Figure 6.2a. There are distinct, discrete artefacts on the surface of the sample in Figure 6.2c that are not present in the object in Figure 6.2a. These discrete particles on the surface of the support shown in Figure 6.2c are believed to be the Ru nanoparticles that were photochemically deposited onto the TiO_2 and then subjected to a thermal treatment to produce RuO_2.

For all the catalysts analysed via TEM, the morphology of the deposited nanoparticles were generally found to be hemispherical as shown in Figure 6.2b, Figure 6.2c and Figure 6.2d, with varying distribution density between each catalyst. The size of the

nanoparticles on the surface of TiO_2 ranges between 1.5 – 4 nm. The Pd nanoparticles measured an average diameter of 2.3 nm, while the RuO_2 nanoparticles had an average size of 3.1 nm. For the Pd:RuO_2:TiO_2 catalyst, the average particle size was measured at 2.1 nm.

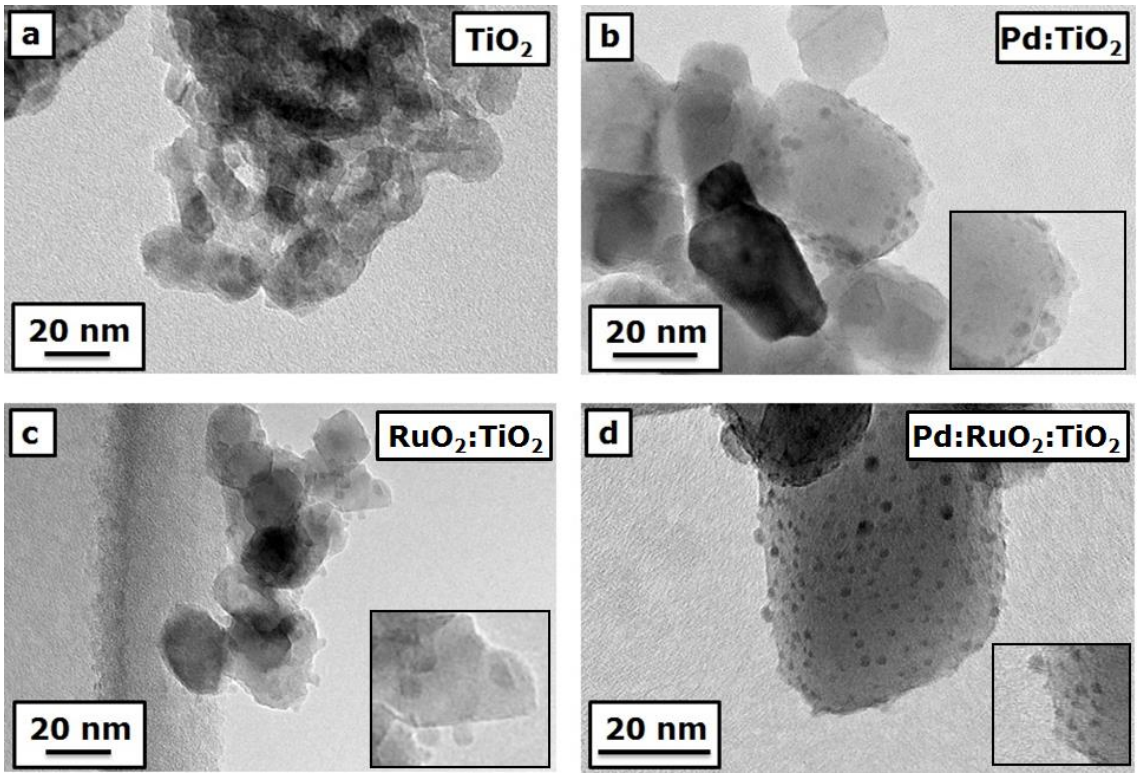

Figure 6.2 TEM micrographs of the catalysts used in H_2 generation experiments

There appears to be a larger distribution of smaller particles on the surface of Pd:RuO_2:TiO_2 catalyst with fewer larger particles. This catalyst (Figure 6.2d) demonstrates the highest overall density of nanoparticles on the surface of the TiO_2 compared with catalysts decorated with either Pd or RuO_2. As the Pd nanoparticles were photochemically deposited onto the already prepared RuO_2:TiO_2 catalyst to produce the Pd: RuO_2:TiO_2, the Pd nanoparticles are believed to have preferentially photo-reduced on the TiO_2 in the spaces between the RuO_2 nanoparticles. Since RuO_2 is thought to be

a hole capture site,[127] this can in effect reduce the electron-hole recombination rate of TiO_2 during the photochemical reduction procedure, resulting in a larger distribution of Pd nanoparticles due to the relative abundance of electrons to reduce Pd^{2+} ions in the solution. However, it was not possible to identify which of the metals constitute the larger or smaller particles, or what the relative distribution is among this sample, as it was not possible to distinguish between the Pd and RuO_2 nanoparticles on the Pd:RuO_2:TiO_2 catalyst. Also, at the levels of metal in this system, the crystal structure of either the Pd or RuO_2 could not be ascertained via XRD analysis as no change in the TiO_2 was observed after the photochemical reduction of metals.

DR measurements confirmed an increase in optical response across the visible region for all three catalysts compared with the TiO_2 as shown in Figure 6.3.

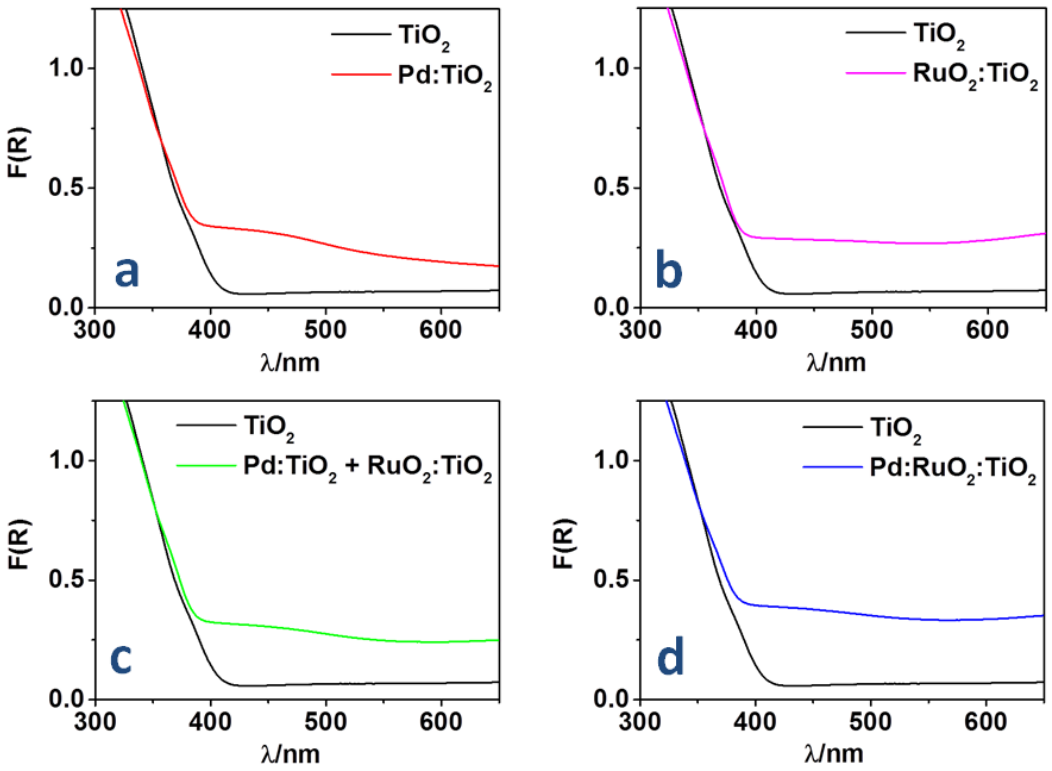

Figure 6.3 DR reflectance measurements of the absorption spectra of Pd:TiO_2 (a), RuO_2:TiO_2 (b), Pd:TiO_2 and RuO_2:TiO_2 (c) and Pd:RuO_2:TiO_2

The increase in the absorption was more pronounced for the Pd:RuO_2:TiO_2 catalyst, than for those containing only RuO_2 or Pd. However, this did not correspond to an improvement in the catalytic activity, since the highest rate of H_2 production was achieved by the Pd:TiO_2.

The absorption profile of the RuO_2:TiO_2 shows a uniform increase in optical response over the visible region compared with the Pd:TiO_2 photocatalyst, which exhibits a large optical response between 400 nm – 500 nm that decreases gradually with increasing wavelength. The spectral profile of the combination of the Pd:TiO_2 and RuO_2:TiO_2 catalysts is the sum of the spectra of the individual catalysts. The Pd: RuO_2:TiO_2 catalyst also exhibits aspects of the spectra of the individual Pd and Ru catalysts however, the combined effect on this sample results in a greater overall optical response throughout the visible region compared with that of the combination of the individual catalysts.

6.2 Evolution of H_2

The evolution of hydrogen by the photocatalysts was investigated under AM 1.5 irradiation in anaerobic conditions. In all tests 33 mg of catalyst was added to 100 mL of solution and TiO_2 was used as a reference catalyst. The levels of H_2 inside the reactor were monitored via GC fitted with a TCD and using N_2 as carrier. The volume expansion of gas was also monitored via water displacement. The evolution of O_2 was checked for all tested catalysts to confirm that O_2 was not being evolved via the photolysis of water in the absence of an additive. Once it was established that none of the synthesised catalysts could produce O_2 in the absence or presence of alcohol, O_2 was no longer monitored and the 3” SG column was used for all of the H_2 generation experiments to monitor the evolution of H_2 and the presence of CO_2.

6.2.1 Effect of type and concentration of alcohol

The type and concentration of alcohol used in the reaction solution was investigated to the alcohol that yielded the highest rate of H_2 production. MeOH, ethanol (EtOH) and 2-propanol (iPrOH) were used as the target compounds to promote the generation of H_2 on the synthesised catalysts. Organic molecules such as alcohols are added to the reaction solution to act as electron donating species, reacting irreversibly with the photo-generated charge carriers to produce H_2. It has been reported that MeOH gives the highest yield of H_2 when compared with EtOH and iPrOH.[202] This may be due to further reactions beyond the primary product as in the case of ethanol and 2-propanol, which are reported to also produce the corresponding aldehyde and ketone as primary products.[166] In this experiment, the reactivity of the alcohol in the presence of the photocatalyst was measured in terms of the rate of production of H_2 only and does not monitor further reactions beyond the primary product.

The Pd:TiO_2 catalyst was used to test the rate of H_2 production of MeOH at three different concentrations levels. These were at 5%, 10% and a maximum concentration of 20% of MeOH. The results show that the evolution of H_2 increased with an increase in the concentration of MeOH as shown in Figure 6.4.

The rate of H_2 generation due to the addition of EtOH and iPrOH was compared with that of MeOH. It was found that MeOH produced the highest amount of H_2 per hour compared to either additive where H_2 generation for MeOH > EtOH > iPrOH. Furthermore, MeOH at a concentration of 5% was observed to produce H_2 at a higher rate than EtOH and iPrOH at concentrations of 20%. These results confirmed that MeOH produces the highest rate of H_2 evolution under the experimental conditions tested.

Subsequent experiments investigating the rate of H_2 production all used MeOH as the additive at a fixed concentration of 20%.

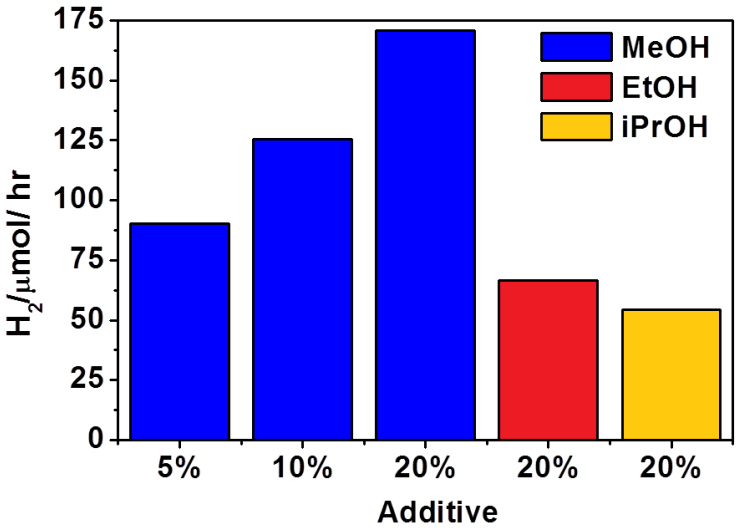

Figure 6.4 The rate of H_2 production at 3 different concentrations of MeOH is compared with the rate of H_2 production for EtOH and iPrOH at the concentration that yielded the highest rate of H_2 evolution for MeOH

6.2.2 Reusability of Pd:TiO_2 catalyst

The continued evolution of H_2 from the reforming of MeOH in the presence of the Pd:TiO_2 catalyst was investigated over a test period of 25 hours. Five cycles, each consisting of a five hour period of solar irradiation, were carried out where the reactor was purged with N_2 at the end of each cycle in order to ensure the next cycle started from a H_2 concentration of zero. The results of the 25 hour experiment are shown in Figure 6.5.

The production of H_2 is shown to gradually decrease over the 25 hour period. Over the first 10 hour period, a steady rate of H_2 generation was observed. After this 10 hour mark, there appeared to be a small reduction in the volume of overall H_2 produced. This decrease in H_2 production was also observed for each subsequent cycle until the end of

the 25 hour run. The results indicate that there is a loss of activity in the production of H_2 during the 25 hours of testing but it is not clear whether this is associated with a decrease in photocatalytic activity of the catalyst, or if it is due to the decrease in the abundance of MeOH in the solution due to its irreversible conversion.

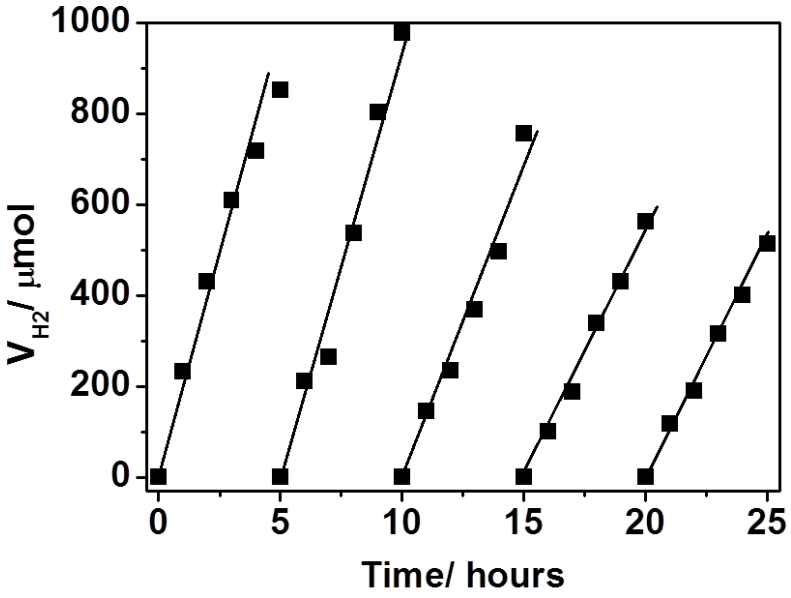

Figure 6.5 The reusability of the Pd:TiO_2 over a 25 hour period made up of five cycles each lasting for five hours. H_2 levels were monitored on an hourly basis and are given in micromoles

A similar reduction in the photocatalytic activity was observed during tests for the recyclability of the catalyst in the photodegradation of RhB dye described in section 5.5 of chapter 5. The reduction in activity was attributed to the deactivation of the catalyst by adsorbed dye or intermediate dye products that had not been completely mineralised within the test period. In the case of the reforming of MeOH, a similar effect was found to be taking place, possibly due to adsorbed CO progressively deactivating the Pd NPs on the surface of the catalyst.

The recyclability experiment was monitored on an hourly basis for a total of 25 hours. However, the test was allowed to run for a total time of 88 hours. During the following 63 hours the evolution of H_2 was observed to continue where the total amount of H_2 produced over the 88 hour period was 10.02 mmol. This gives an average rate of H_2 generation of 113.89 µmol/h for the Pd:TiO_2 catalyst over this time period. Compared with the initial rate of H_2 production for the first 5 hour cycle of 170.45 µmol/h, this constitutes a 33% reduction in activity over the total run time of 88 hours. At the end of the test, no other gases were detected via GC confirming that the only products of the reaction were H_2 and CO_2.

6.2.3 Effect of different catalysts on H_2 generation

A total of four catalysts were tested in the evolution of H_2 from the reforming of MeOH. GC analysis of the evolved gas confirmed the constituents to be H_2 and CO_2. The H_2 levels were monitored during the course of the experiments as a measure of the photocatalytic activity of the catalysts. Although CO_2 was detected, it was not possible to monitor its evolution. This was due to the set-up of the GC using N_2 as carrier where the thermal conductivity of CO_2 is close to that of N_2. As a result, the system was not sufficiently sensitive to monitor its hourly evolution at the levels produced. Figure 6.6 shows an example of the GC output where the H_2 and CO_2 (inset) peaks are given in terms of the detector signal as a function of time.

This data was obtained after an irradiation time of 17 hours to allow for the build-up of CO_2 inside the reactor in order to clearly illustrate the position and intensity of its peak compared to that of H_2. No other gases were detected for any of the reactions, and control experiments established that no H_2 was produced in the absence of solar

irradiation, of MeOH, or in the presence of TiO_2 only. This confirms that Pd and/or Ru as co-catalysts on the TiO_2 support, as well as illumination and MeOH, are all necessary for the H_2 generation reaction to proceed.

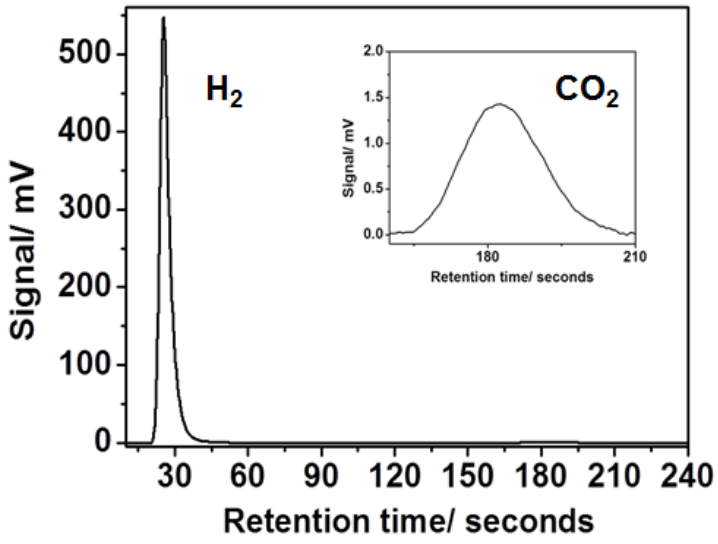

Figure 6.6 Output from GC showing the H_2 in the main window of the graph. The CO_2 peak is shown in the inset, illustrating the poor sensitivity of the GC towards CO_2 using the current setup

The results of the evolution of H_2 in the presence of the different Pd and RuO_2 catalysts are shown in Figure 6.7.

The combination of the monometallic Pd:TiO_2 and RuO_2:TiO_2 catalysts showed the highest rate of H_2 production out of the tested samples, with an average H_2 production rate of 192 µmol/h. This corresponds to a STH conversion efficiency of 0.77%. Conversely, the RuO_2:TiO_2 samples showed the lowest production of H_2 with an average rate of 33 µmol/h and an STH efficiency of 0.10%, while Pd:TiO_2 produced 171 µmol/h at an STH of 0.69%. The Pd:RuO_2:TiO_2 catalyst produced H_2 at a rate of 140 µmol/h and with an STH efficiency value of 0.56%. The STH conversion efficiencies and the H_2 evolution rates for the tested catalysts are given in Table 6.1.

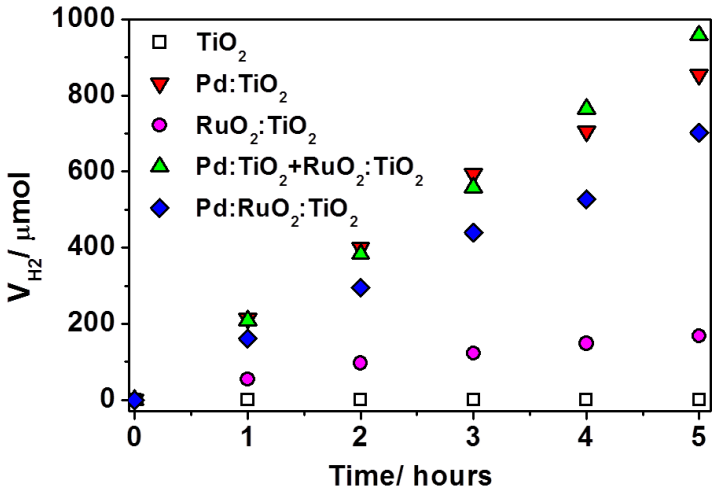

Figure 6.7 The production of H_2 by the synthesised catalysts via the reforming of MeOH under solar irradiation

The rate of H_2 production for the $Pd:TiO_2$ catalyst was found to be between that of the mixed $Pd:TiO_2$ + $RuO_2:TiO_2$ and the Pd: $RuO_2:TiO_2$ samples. Interestingly, the photocatalyst composed of both Pd and RuO_2 on the same support (Pd: $RuO_2:TiO_2$) shows a lower rate of H_2 production than when a mixture ($Pd:TiO_2$ + $RuO_2:TiO_2$) of two catalysts is used.

Table 6.1 Average production of H_2 per catalyst over 5 hours and corresponding STH conversion efficiency

Catalyst	H_2 production µmol/ h	STH Conversion efficiency/ %
$Pd:TiO_2$ (33 mg)	170.83	0.69
$RuO_2:TiO_2$ (33 mg)	33.46	0.10
$Pd:TiO_2$ + $RuO_2:TiO_2$ (16.5 mg + 16.5 mg)	191.72	0.77
$Pd:RuO_2:TiO_2$ (33 mg)	140.45	0.56

The efficiency increase of the mixed catalyst compared with the bimetallic sample is close to 27%. This represents almost a 8-fold increase in efficiency when compared to the $RuO_2:TiO_2$ on its own, and a 10% increase on the rate of H_2 production of $Pd:TiO_2$.

6.2.4 Effect of catalyst loading

In order to directly compare the results of the combination of $Pd:TiO_2$ + $RuO_2:TiO_2$ catalysts with the individual catalysts, an investigation into the effect of the catalyst loading values of the $Pd:TiO_2$ and $RuO_2:TiO_2$ samples was carried out. The results of the tests are shown in Figure 6.8.

The results showed that the $Pd:TiO_2$ catalyst at a loading of 0.165 g/L produced H_2 at a similar rate compared with the monometallic mixture of the $Pd:TiO_2$ + $RuO_2:TiO_2$ catalysts. This was a small increase in activity compared to $Pd:TiO_2$ loading at 0.330 g/L. A further decrease in the loading of the $Pd:TiO_2$ sample to 0.083 g/L led to a reduction in the rate of H_2 production compared with higher catalyst loadings This indicated that out of the tested loading values, 0.165 g/L was the optimum amount for the $Pd:TiO_2$.

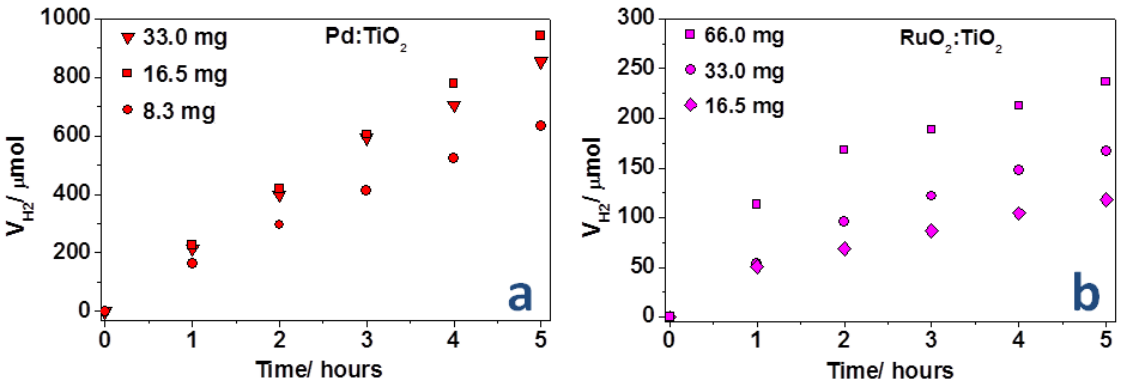

Figure 6.8 Results of tests carried out to investigate the effect of $Pd:TiO_2$ and $RuO_2:TiO_2$ catalyst loadings

In the case of the $RuO_2:TiO_2$ catalyst, H_2 production at a loading of 0.165 g/L was found to be the lowest of the tested values at 0.330 g/L and 0.660 g/L.

The results of the catalyst loading investigation indicate that the production of H_2 in tests using the $Pd:TiO_2$ + $RuO_2:TiO_2$ sample is due to the photocatalytic activity of the $Pd:TiO_2$ in the mixture since no summative effect of the two catalysts was observed. This is

confirmed by the fact that a cummulative production of H_2 by both the $Pd:TiO_2$ and $RuO_2:TiO_2$ samples would give a total H_2 generation rate of 212 µmol/h.

The observed decrease in the production of H_2 for the $RuO_2:TiO_2$ catalyst at the lower loading of 0.165 g/L compared with 0.330 g/L and 0.660 g/L is attributed to the reduction in available RuO_2 sites photochemically deposited on the TiO_2. This is estimated to be a factor of 20 less than the amount of supported Pd and is thought to be the limiting factor for these reactions.

Table 6.2 The effect of catalyst loading on H_2 production and comparison with previous results

Catalyst	Catalyst loading/ g/L	Average H_2/ µmol
$Pd:TiO_2$	0.083	126.37
$Pd:TiO_2$	0.165	188.42
$Pd:TiO_2$	0.330	170.83
$RuO_2:TiO_2$	0.165	22.47
$RuO_2:TiO_2$	0.330	32.34
$RuO_2:TiO_2$	0.660	47.36
$Pd:TiO_2 + RuO_2:TiO_2$	0.165 + 0.165	191.72
$Pd:RuO_2:TiO_2$	0.330	140.5

In the case of the $Pd:TiO_2$ catalyst, the generation of H_2 is only observed to decrease significantly when a loading of 0.083 mg/L is used compared with loadings of 0.165 g/L and at 0.330 g/L. At a loading of 0.330 g/L compared to 0.165 g/L, the number of Pd sites is effectively doubled without any increase in the generation of H_2.

This minimal difference in the production of H_2 between $Pd:TiO_2$ loadings of 0.165 g/L and 0.330 g/L shows that while the number of active sites at the loading of 0.330 g/L is double than at a loading of 0.165 g/L, there is no significant increase in the harvesting of super-band gap photons.

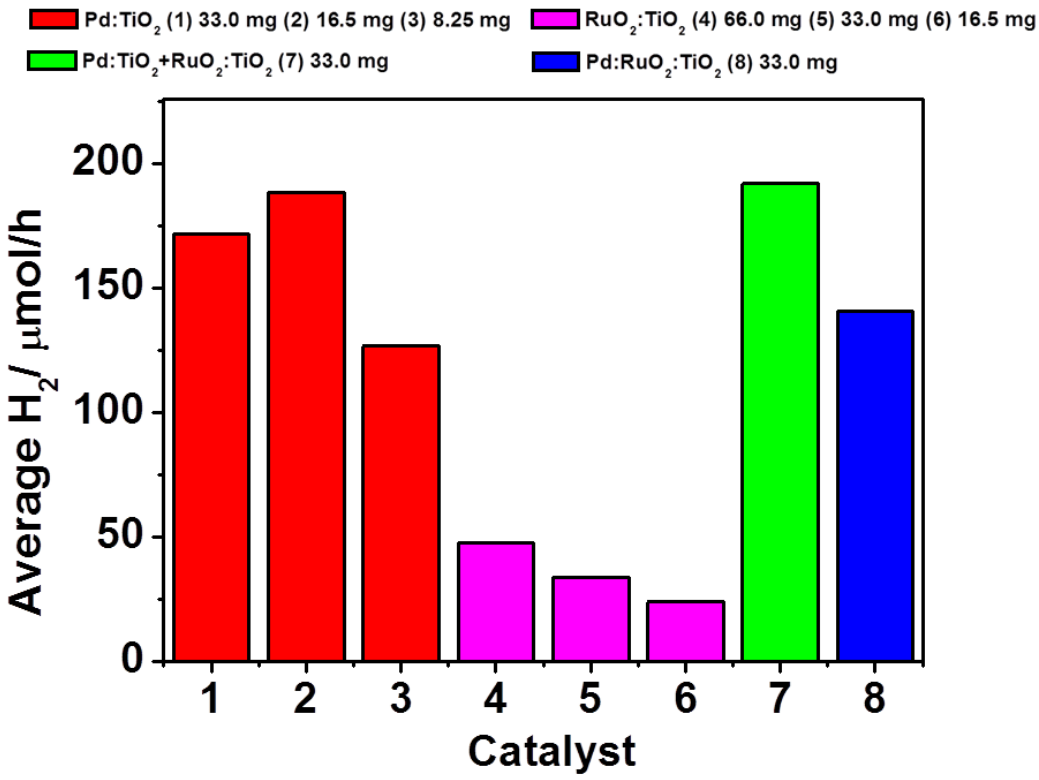

Figure 6.9 Comparison of the photocatalytic activity of the catalysts as a function of catalyst loading

An increase in the active sites for the harvesting of super-band gap photons should increase the rate of H_2 generation however, a negative effect was observed at a loading 0.330 g/L. At the higher loading level, the scattering of light is likely to be a factor in the absorption properties of the suspension, as well as the agglomeration of the catalyst, which in turn affects the photocatalytic activity of the system.

Figure 6.8 and Figure 6.9 show that the rate of H_2 production by the mixed Pd:TiO_2 + RuO_2:TiO_2 system is largely attributed to the activity of the Pd:TiO_2 catalyst. This is thought to be the case for the bimetallic sample also. Furthermore, the reduction in activity for the bimetallic catalyst is due to the loss of available TiO_2 active sites on the surface of the catalyst as a result of the increased distribution density of nanoparticles on the TiO_2.

It is possible to describe these observations regarding the rate of H_2 generation in terms of the reactions on the surface of the photocatalysts.

6.3 Mechanisms at Pd:TiO_2 and RuO_2:TiO_2 catalyst surfaces

In order to explain the difference in activity between each of the tested photocatalysts it is necessary first to understand the mechanisms of H_2 generation occurring on each of the monometallic catalysts. Consider separately the reported mechanism for the reaction on a TiO_2–supported Pd catalyst[210] and on a RuO_2 modified TiO_2 catalyst.[126,191] The reaction on each of the monometallic catalysts yields the same overall products as shown in Equation 6.1. However, the intermediate steps are reported to be different.

$$CH_3OH + H_2O \xrightarrow[Pd\text{-}TiO_2 / RuO_2\text{-}TiO_2]{hv} 3H_2 + CO_2 \quad \textbf{(6.1)}$$

The suggested reaction on the Pd modified catalyst comprises the adsorption and subsequent dehydrogenation of methanol on the supported Pd nanoparticles as shown in Equation 6.2.

$$CH_3OH \xrightarrow{Pd} CO + 2H_2 \quad \textbf{(6.2)}$$

A layer of CO is formed on the Pd and H_2 is released. Excitation of the catalyst via solar irradiation creates an electron-hole pair that forms a highly reactive O^- species in the TiO_2 lattice (Equation 6.3). This in turn oxidises the adsorbed CO on the Pd to liberate gaseous CO_2 creating a vacancy in the TiO_2 lattice at metal/ semiconductor interface (Equation 6.4). The anion vacancy is then filled via the oxidation with water to liberate H_2 on the TiO_2 surface (Equation 6.5).

$$Ti^{4+} + O^{2-} \xrightarrow{hv} Ti^{3+} + O^- \quad \textbf{(6.3)}$$

$$O^- + CO \longrightarrow CO_2 + V_O \quad \textbf{(6.4)}$$

$$Ti^{3+} + V_O + H_2O \longrightarrow Ti^{4+} + O^{2-} + H_2 \quad \textbf{(6.5)}$$

This mechanism can account for the observed generation of H_2 and CO_2 for the photo-induced reforming of MeOH reaction in the presence of the Pd:TiO_2 catalyst.

The reaction pathway is reported to follow different kinetics on the RuO_2:TiO_2 photocatalyst. RuO_2 is more oxidative than Pd and is thought to promote the capture of holes rather than electrons.[231]

When a metal and semiconductor come into contact, the Fermi level of the two materials aligns until a thermodynamic equilibrium is reached. In the case of the TiO_2 and the metals, the semiconductor Fermi level is higher than that of Pd or RuO_2. The alignment results in an upward bending of both the VB and the CB, and the formation of a Schottky barrier between the semiconductor and the metal, Figure 6.10.

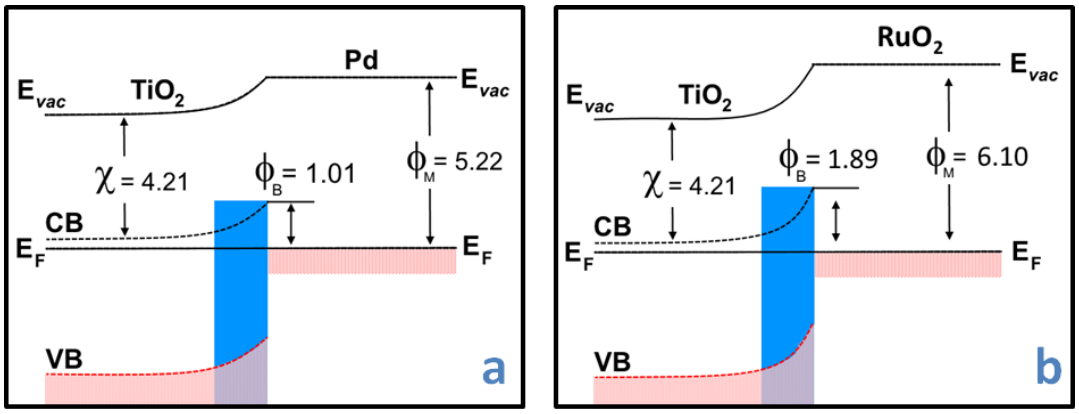

Figure 6.10 Formation of Schotty barrier at the Pd/TiO_2 interface (a) and at the RuO_2/TiO_2 interface (b) where χ is the electron affinity of TiO_2, ϕ_B is the barrier height and ϕ_M is the work function of the metal

The degree of band bending is dependent on the work function of the metal and the electron affinity of the semiconductor, and this determines the ultimate height of the barrier formed and indicates whether the metal nanoparticle can inhibit the recombination of excited charge carriers by acting as an electron or a hole traps. The barrier height, Φ_B was calculated using Equation 2.4. Using the value for the Φ_M of Pd of

5.22 eV,[226] of RuO_2 at 6.10 eV[137] and the χ of TiO_2 estimated at 4.21 eV,[227,228] the Φ_B was calculated to be 1.01 eV for Pd:TiO_2 and 1.89 eV for the RuO_2:TiO_2 photocatalyst as shown in Figure 6.10a and Figure 6.10b, respectively. The difference in the value of the Schottky barrier height for each catalyst suggests that electron transfer to the RuO_2 nanoparticles requires more energy to overcome the barrier than for the Pd nanoparticles. As such, the degree of band bending for the RuO_2:TiO_2 contact makes it more favourable towards hole capture. This is in agreement with reports that Pd nanoparticles act as electron traps,[231] while the RuO_2 nanoparticles facilitate hole transfer from the TiO_2 to the aqueous solution.

The mechanism for the photocatalytic reaction on the RuO_2:TiO_2 catalyst is reported to go via the following steps:

$$CH_3OH \xrightarrow[RuO_2:TiO_2]{hv} HCHO + H_2 \quad \textbf{(6.6)}$$

where a photogenerated hole reacts with MeOH to generate a $^{\bullet}CH_2OH$ radical that further reacts to produce formaldehyde as shown in Equation 6.6. Formaldehyde can then react further with the catalyst:

$$HCHO + H_2O \xrightarrow[RuO_2:TiO_2]{hv} HCOOH + H_2 \quad \textbf{(6.7)}$$

$$HCOOH \xrightarrow[RuO_2:TiO_2]{hv} CO_2 + H_2 \quad \textbf{(6.8)}$$

The main products of the reaction at the RuO_2:TiO_2 photocatalyst are formaldehyde and H_2 as shown in Equation 6.6. However, the formaldehyde can be further oxidised to formic acid and H_2 (Equation 6.7) and further again to yield CO_2 and H_2 (Equation 6.8). The overall reaction on RuO_2:TiO_2 can therefore ultimately be represented as shown in Equation 6.1.

The presence of formaldehyde or formic acid was not confirmed for the photocatalytic H_2 generation as the products of the reaction were only monitored in the gas phase. However, CO_2 was confirmed for all reactions where H_2 was produced adding support to the proposed mechanisms occurring on the Pd:TiO_2 and RuO_2:TiO_2 photocatalysts.

It is clear from the reaction pathways outlined above, that the excitation of TiO_2 and the generation of an electron-hole pair is necessary in order to propagate the production of H_2 in the presence of either photocatalyst. This process supports the observation of the decrease in photocatalytic activity of the Pd:RuO_2:TiO_2, where the increase in the distribution density of the supported nanoparticles resulted in the reduction of the active surface area of the TiO_2 support. The number of available reactive sites on the bimetallic catalyst is therefore relatively less than for the monometallic catalysts and hence an overall reduction in the rate of H_2 production was observed. It is also possible that under these conditions, since the metal nanoparticles are in much closer proximity to each other, that the deposited nanoparticles are acting as electron-hole recombination centres rather than charge carrier trap sites.[126]

In the case of the monometallic catalysts, the exposed surface area of TiO_2 remains relatively larger than the bimetallic sample. This is beneficial in terms of photon absorption and subsequent charge separation. Charge carrier capture on the deposited nanoparticles may also be more effective under these conditions.

The rate of H_2 production of the synthesised catalysts was compared with similar systems from the literature where Pt, Pd or RuO_2 nanoparticles were used as co-catalysts supported on TiO_2. Due to lack of data in terms of irradiation sources and vessel geometry, the STH conversion efficiencies for the other samples could not be computed

and the only viable comparison was to present the results in terms of the moles of H_2 produced per hour per gram of catalyst. Table 6.3 shows the results of these H_2 generation experiments compared with other work.

Table 6.3 Comparison of synthesised catalysts to other TiO_2 supported Pt, Pd and RuO_2 photocatalysts in the literature

Catalyst	Activity/ H_2/ µmol/h	Catalyst loading/ g/L	Additive/ mol	Activity/ H_2/ µmol/h/g	Refs
Pd:TiO_2 + RuO_2:TiO_2	**192**	**0.330**	**0.49 MeOH**	**5818**	-
Pd:TiO_2	**171**	**0.330**	**0.49 MeOH**	**5182**	-
Pd:TiO_2	**188**	**0.165**	**0.49 MeOH**	**5710**	-
Pd:TiO_2	**126**	**0.083**	**0.49 MeOH**	**3830**	-
Pd: RuO_2:TiO_2	**140**	**0.330**	**0.49 MeOH**	**4242**	-
RuO_2:TiO_2	**47**	**0.660**	**0.49 MeOH**	**1435**	-
RuO_2:TiO_2	**33**	**0.330**	**0.49 MeOH**	**1000**	-
RuO_2:TiO_2	**24**	**0.165**	**0.49 MeOH**	**717**	-
Pt:TiO_2	5	0.1	-	50	[37]
Pd:TiO_2	12.5	0.5	1.24 MeOH	25	[31]
Pt:TiO_2	568	0.3	0.76 $NaCO_3$	1893	[207]
Pt:TiO_2	34	0.1	-	340	[232]
Pt:RuO_2:TiO_2	125	0.025	-	5000	[127]
Pd:TiO_2	107	0.2	0.002 MeOH	535	[118]

The rate of H_2 generation obtained using the photocatalysts described in this study under solar conditions was found to be among the highest rates reported in the literature for similar photocatalyst systems. All four of the tested catalysts showed high rates of H_2 generation compared with the literature; the most active photocatalyst showing a 14% increase in activity compared with the most active catalyst in the literature, which was based on a Pt:RuO_2:TiO_2 system.

It seems that the nanoparticle loading on the bimetallic Pd:RuO_2:TiO_2 photocatalyst exceeded the optimal distribution density for this type of co-catalyst system and as such, a reduction in its photocatalytic activity was observed compared with the Pd:TiO_2 samples or the combination of the Pd:TiO_2 + RuO_2:TiO_2 catalysts.

6.4 Summary

The efficient generation of H_2 via the photo-induced reforming of MeOH on Pd and RuO_2 modified TiO_2 has been observed. The results of the control experiments support the overall mechanism proposed, showing that both the generation of excited charge carriers in TiO_2 and the presence of the supported nanoparticles are essential for the increase in the photocatalytic activity of the catalysts. Furthermore, it was found that the highest rate of H_2 evolution was achieved via a combination of the monometallic Pd:TiO_2 + Ru:TiO_2 catalysts at 192 µmol/h. The photocatalytic activity of this sample is similar to the rate of H_2 production of Pd:TiO_2, which was found to be 188 µmol/h. This shows that the Pd:TiO_2 is the major influence on the rate of reaction in this system, with the contribution of the RuO_2:TiO_2 sample having a minimal effect when combined with the Pd:TiO_2 catalyst.

In addition, a decrease in photocatalytic activity was observed for the bimetallic Pd:RuO_2:TiO_2 photocatalyst, which is thought to arise from a reduction in the available surface area of TiO_2 required for super-band gap absorption and for the reduction of H_2O. The reduction in surface area was found to be due to the high distribution density of supported Pd and RuO_2 nanoparticles as a result of the combination of the synthesis procedures to produce the bimetallic catalyst.

This photocatalyst is believed to be the first example of such a co-catalyst using a combination of Pd and RuO_2. The combination of the monometallic Pd:TiO_2 and Ru:TiO_2 catalysts showed the highest STH conversion efficiency of any Pd-based photocatalyst reported in the literature for similar systems, with a STH value of 0.77%. The photocatalytic activity of the most efficient catalyst in this study showed a 14% increase in the rate of H_2 production compared with the most active PGM modified TiO_2 photocatalyst reported in the literature.

7 Conclusions and future work

7.1 Conclusions

The key findings of this thesis can be summarised as follows:

A new PGM modified TiO_2 catalyst was synthesised using a photochemical reduction procedure where its photocatalytic activity was tested in the photodegradation of RhB dye and in the production of H_2 via the photo-induced reforming of MeOH.

The photocatalytic activity of the Pd:TiO_2 photocatalyst in the decolourisation rate of RhB was measured to be a 19-fold improvement compared to unmodified TiO_2 under full solar irradiation. The rate of H_2 evolution through the photo-induced reforming of MeOH for the same photocatalyst was found to be among the highest found in the literature. Furthermore, the Pd:TiO_2 catalyst used in conjunction with a RuO_2:TiO_2 in H_2 evolution experiments was found to have a solar to hydrogen conversion efficiency of 0.95% and the highest H_2 production rate in terms of μmol/hour/gram of catalyst, reported in the literature.

The synthesis of the photocatalyst comprised a procedure designed to photochemically reduce Pd metal onto TiO_2 at low intensity of UV irradiation. It was observed that the metal nanoparticles formed stable hemispherical morphologies with sizes averaging 2 nm to 4 nm in diameter. The preparation of the photocatalyst was altered in order to investigate the effects of changing certain procedural parameters on the physical properties and resultant photocatalytic activity of the catalyst.

The initial nucleation/deposition of the Pd nanoparticles was found to be consistent with previous studies where the distribution density of the nucleation sites was dependent on the intensity of the UV irradiation. The exposure of the metal salt precursor to higher

UV intensity values resulted in a higher overall distribution of Pd nanoparticles on the surface of the substrate. It was also shown that the total loading of the metal was dependent only on the concentration of the precursor.

The initial nucleation step in this procedure was observed to occur in less than 10 s as no significant further increase in metal loading was observed after longer periods of irradiation. Nucleation has previously been reported to occur in the order of 100 ms, which is consistent with findings in this work.

Irradiation of the solution for longer periods resulted in the subsequent growth of the metal nanoparticles. This was attributed to the coalescence of Pd nanoclusters via a slow diffusion limited process, as no further increase in the Pd content was measured for samples synthesised at the same concentrations.

The Pd nanoparticles were observed to exhibit LSPR, which extended to the visible region of the spectrum. Though the Pd LSPR peak is normally observed in the UV region for nanoparticles of less than 10 nm, the results show a significant shift due to the strong metal-support interaction. This is supported by previous research indicating that the interaction of the metal nanoparticles with the substrate can induce a red-shift in the position of the plasmon peak by up to 100 nm and is consistent with the findings in this thesis.

The magnitude of the red-shift of the plasmon peak was dependent on the size of the supported Pd such that larger nanoparticles produced a shift of a larger magnitude. This in turn is ultimately dependent on the concentration of the Pd and the length of the UV exposure.

For RhB photodecolourisation experiments, the photocatalytic activity of the catalysts was found to be dependent on the position of the plasmon peak; catalysts exhibiting larger red-shifts in the plasmon peak showed faster photodecolourisation of RhB. This increase in activity is attributed to the improved visible light harvesting capabilities of the catalyst and also the reduction of charge carrier recombination.

It was found that a combination of both UV and visible light were required to produce the best results in terms of the photodecolourisation of RhB and this was attributed to two separate mechanisms working in cooperation under full solar irradiation. To investigate the mechanisms separately, optical band pass filters were used to block regions of the incident solar irradiation to monitor the photocatalytic activity of the catalyst under UV or visible light irradiation only. The investigation observed that one mechanism is characterised by the absorption of super band gap photons inducing the generation of the charge carriers within the TiO_2. The supported Pd nanoparticles act as electron traps preventing the recombination of electron-hole pairs and promoting redox reactions on the surface of the catalyst. As the LSPR extends into the UV, some of the effects of this, such as the resonant energy transfer (RET) of excited electrons to the TiO_2 can occur, contributing to the increase in activity.

The second mechanism is attributed to the visible light excitation and the associated LSPR, where some of the excited electrons can overcome the Schottky barrier formed at the Pd/TiO_2 interface and transfer to the semiconductor. These electrons can then react with species adsorbed to the catalyst surface. The combination of these two mechanisms were observed to have a beneficial synergistic effect on the overall photocatalytic activity of the catalyst under AM 1.5 irradiation.

The photocatalytic activity of the catalyst was also tested by measuring the rate of H_2 production. Two further catalysts were synthesised to determine their capability for H_2 production via the direct photolysis of water; a RuO_2:TiO_2 catalyst and a bimetallic Pd:RuO_2:TiO_2 catalyst. The Pd:RuO_2:TiO_2 sample is believed to be the first reported instance of a photocatalyst comprised of these materials on a TiO_2 substrate capable of producing H_2.

In all tests it was found that no H_2 was produced in the absence of an electron donor in the presence of any of the photocatalysts. H_2 generation was only observed when alcohols such as methanol, ethanol and isopropyl alcohol were used as sacrificial reagents.

RuO_2 was chosen for the TiO_2 modification because it is more oxidative than Pd and the idea was to promote reduction on the Pd nanoparticles and oxidation on the RuO_2 nanoparticles. The Pd:RuO_2:TiO_2 photocatalyst was synthesised to try and spatially separate these redox reactions on the surface of the photocatalyst in a system analogous to a photoelectrochemical nano-cell. The direct photolysis of water did not proceed under the tested conditions so the spatial separation of the redox reactions could not be confirmed.

The rate of H_2 production was observed to be highest for a combination of the Pd:TiO_2 and RuO_2:TiO_2 catalysts and lowest for the RuO_2:TiO_2. The rate of H_2 generation over the Pd:TiO_2 catalyst was similar to that of the combination of the Pd:TiO_2 and RuO_2:TiO_2 indicating that no summative effect of the two samples occurred. The Pd:RuO_2:TiO_2 photocatalyst showed an intermediate rate of H_2 production compared with the RuO_2:TiO_2 and Pd:TiO_2 samples. This was attributed to the increased distribution of

nanoparticles on the surface of the bimetallic catalyst relative to the surface distribution of nanoparticles on the monometallic samples. The higher density of metal distribution was found to prevent the absorption of super-band photons by the TiO_2 substrate and inhibit the rate of reaction. In addition, the LSPR of Pd did not have a significant effect on the rate of H_2 generation and no H_2 was produced under visible light irradiation only.

7.2 Future work

The investigations carried out have provided many opportunities for future research in order to further improve the efficiency of TiO_2 based photocatalysts. Some of the areas that would benefit from further work include:

- Improving the tuneable aspect of photochemical Pd reduction to further red-shift the LSPR peak. This work showed that the size and distribution of photochemically reduced Pd could be altered depending on the concentration of the metal precursor and intensity of the UV exposure. These parameters were shown to affect the position of the observed LSPR peak. The plasmonic properties of metals have been generating interest in a wide range of applications and the ability to tune the LSPR resonance peak of supported Pd nanoparticles is a promising prospect in visible light photocatalysis.
- The use of RuO_2 as supported nanoparticles on TiO_2 is an interesting prospect in improving the photocatalytic properties of TiO_2 photocatalysts. Further research should be undertaken to investigate the effects of the loading of RuO_2 on TiO_2 in terms of its selectivity towards the degradation of other compounds.
- An investigation into optimisation of bimetallic RuO_2 and Pd on TiO_2 substrates. It was shown that both Pd and RuO_2 can photo-reform methanol under ambient

conditions. The effect of the metal loading and distribution density on the rate of H_2 production should be explored in order to understand the interactions between the two metals on the support. The mechanism of these reactions at the catalyst surface should also be investigated to determine the reaction pathway and optimise the generation of H_2.

- The combination of different metals on a single substrate has been shown in other work to be an effective method to spatially separate redox reactions at different reactive sites. An investigation into the suitability of using a combination of other noble metal nanoparticles would be useful to try and improve the activity of TiO_2 based photocatalyst, with the possibility of discovering materials capable of achieving overall water splitting in the absence of sacrificial donors.

REFERENCES

(1) Graetzel, M. *Acc. Chem. Res.* **1981**, *14*, 376–384.

(2) Bard, A.; Fox, M. A. *Acc. Chem. Res.* **1995**, *28*, 141–145.

(3) Chen, X.; Shen, S.; Guo, L.; Mao, S. S. *Chem. Rev.* **2010**, *110* (11), 6503–6570.

(4) Gust, D.; Moore, T. a; Moore, A. L. *Acc. Chem. Res.* **2009**, *42* (12), 1890–1898.

(5) Kawai, T.; Sakata, T. *Nature* **1980**, *286*, 474–476.

(6) Chong, M. N.; Jin, B.; Chow, C. W. K.; Saint, C. *Water Res.* **2010**, *44* (10), 2997–3027.

(7) Murphy, a. B.; Barnes, P. R. F.; Randeniya, L. K.; Plumb, I. C.; Grey, I. E.; Horne, M. D.; Glasscock, J. a. *Int. J. Hydrogen Energy* **2006**, *31* (14), 1999–2017.

(8) Fujishima, A.; Honda, K. *Nature* **1972**, *238*, 37–38.

(9) Tong, H.; Ouyang, S.; Bi, Y.; Umezawa, N.; Oshikiri, M.; Ye, J. *Adv. Mater.* **2012**, *24*, 229–251.

(10) Kudo, A. *Pure Appl. Chem.* **2007**, *79* (11), 1917–1927.

(11) Li, J.; Wu, N. *Catal. Sci. Technol.* **2015**, *5* (3), 1360–1384.

(12) Hashimoto, K.; Irie, H.; Fujishima, A. *Jpn. J. Appl. Phys.* **2005**, *44* (12), 8269–8285.

(13) Litter, M. I. *Appl. Catal. B Environ.* **1999**, *23* (2-3), 89–114.

(14) Liu, G.; Wang, L.; Yang, H. G.; Cheng, H.-M.; (Max) Lu, G. Q. *J. Mater. Chem.* **2010**, *20* (5), 831.

(15) Wang, Q.; Chen, C.; Zhao, D.; Ma, W.; Zhao, J. *Langmuir* **2008**, *24* (14), 7338–7345.

(16) Choi, W.; Termin, A.; Hoffmann, M. R. *J. Phys. Chem.* **1994**, *98* (51), 13669–13679.

(17) Linsebigler, A. L.; Lu, G.; Yates, J. T. *Chem. Rev.* **1995**, *95* (3), 735–758.

(18) Hoffmann, M. R.; Martin, S. T.; Choi, W.; Bahnemannt, D. W. *Chem. Rev.* **1995**, *95* (1), 69–96.

(19) Yu, P.; Cardona, M. *Fundamentals of Semiconductors: Physics and Materials Properties*; 1996.

(20) Rajeshwar, K. In *Encyclopedia of electrochemistry*; 2001.

(21) Mills, A.; Le Hunte, S. *J. Photochem. Photobiol. A Chem.* **1997**, *108* (1997), 1–35.

(22) Bard, A. *Science (80-.).* **1980**, *207* (4427), 139–144.

(23) Bott, A. *Curr. Sep.* **1998**, *3*, 87–91.

(24) Renz, C. *Helv. Chim. Acta* **1921**, *4*, 961–968.

(25) Goodeve, C. F.; Kitchener, J. A. *Transactions of the Faraday Society*. 1938, p 570.

(26) Yamaguti, K.; Sato, S. *Journal of the Chemical Society, Faraday Transactions 1*. 1985, p 1237.

(27) Kudo, A.; Domen, K.; Maruya, K.; Onishi, T. *Chemical Physics Letters*. 1987, pp 517–519.

(28) Ohno, T.; Tanigawa, F.; Fujihara, K.; Izumi, S.; Matsumura, M. *J. Photochem. Photobiol. A Chem.* **1999**, *127* (1-3), 107–110.

(29) Abe, R.; Sayama, K.; Arakawa, H. *Chem. Phys. Lett.* **2003**, *371* (3-4), 360–364.

(30) Sasikala, R.; Sudarsan, V.; Sudakar, C.; Naik, R.; Sakuntala, T.; Bharadwaj, S. R. *Int. J. Hydrogen Energy* **2008**, *33*, 4966–4973.

(31) Kwak, B. S.; Chae, J.; Kim, J.; Kang, M. *Bull. Korean Chem. Soc.* **2009**, *30* (5), 1047–1053.

(32) Sasikala, R.; Shirole, a.; Sudarsan, V.; Sakuntala, T.; Sudakar, C.; Naik, R.; Bharadwaj, S. R. *Int. J. Hydrogen Energy* **2009**, *34* (9), 3621–3630.

(33) Dholam, R.; Patel, N.; Santini, a.; Miotello, a. *Int. J. Hydrogen Energy* **2010**, *35* (18), 9581–9590.

(34) Chen, X.; Liu, L.; Yu, P. Y.; Mao, S. S. *Science* **2011**, *331*, 746–750.

(35) Yu, J.; Hai, Y.; Jaroniec, M. *J. Colloid Interface Sci.* **2011**, *357* (1), 223–228.

(36) An, W.-J.; Wang, W.-N.; Ramalingam, B.; Mukherjee, S.; Daubayev, B.; Gangopadhyay, S.; Biswas, P. *Langmuir ACS J. surfaces colloids* **2012**, *28* (19), 7528–7534.

(37) Maeda, K. *Chem. Commun.* **2013**, *49* (75), 8404–8406.

(38) Reddy, J. K.; Lalitha, K.; Reddy, P. V. L.; Sadanandam, G.; Subrahmanyam, M.; Kumari, V. D. *Catal. Letters* **2013**, *144* (2), 340–346.

(39) Zhang, Z.; Zhang, L.; Hedhili, M. N.; Zhang, H.; Wang, P. *Nano Lett.* **2013**, *13* (1), 14–20.

(40) Liu, E.; Kang, L.; Yang, Y.; Sun, T.; Hu, X.; Zhu, C.; Liu, H.; Wang, Q.; Li, X.; Fan, J. *Nanotechnology* **2014**, *25* (16), 165401.

(41) Maijenburg, A. W.; Veerbeek, J.; de Putter, R.; Veldhuis, S. a.; Zoontjes, M. G. C.; Mul, G.; Montero-Moreno, J. M.; Nielsch, K.; Schäfer, H.; Steinhart, M.; ten Elshof, J. E. *J. Mater. Chem. A* **2014**, *2* (8), 2648.

(42) Zhao, C.; Luo, H.; Chen, F.; Zhang, P.; Yi, L.; You, K. *Energy Environ. Sci.* **2014**, *7* (5), 1700.

(43) Roy, S.; Varghese, O.; Paulose, M.; Grimes, C. *ACS Nano* **2010**, *4* (3), 1259–1278.

(44) Matthews, R. W. *Water Res.* **1990**, *24* (5), 653–660.

(45) Wang, C.-M.; Gerischer, H.; Heller, A. *J. Am. Chem. Soc.* **1992**, *114* (17), 5230–5234.

(46) Mengyue, Z.; Shifu, C.; Yaowu, T. *J. Chem. Technol. Biotechnol.* **1995**, *64* (4), 339–344.

(47) Muneer, M.; Philip, R.; Das, S. *Res. Chem. Intermed.* **1997**, *23* (3), 233–246.

(48) Shourong, Z.; Qingguo, H.; Jun, Z.; Bingkun, W. *J. Photochem. Photobiol. A Chem.* **1997**, *108*, 235–238.

(49) Sobczynski, A.; Dobosz, A. *Polish J. Environ. Stud.* **2001**, *10* (4), 195–205.

(50) Epling, G. a; Lin, C. *Chemosphere* **2002**, *46* (4), 561–570.

(51) Choi, W. *Catal. Surv. from Asia* **2006**, *10* (1), 16–28.

(52) Bowering, N.; Croston, D.; Harrison, P. G.; Walker, G. S. *Int. J. Photoenergy* **2007**, *2007*, 1–8.

(53) Hussein, F.; Abass, T. *Int. J. Chem. Sci.* **2010**, *8* (3), 1353–1364.

(54) Pelaez, M.; Nolan, N. T.; Pillai, S. C.; Seery, M. K.; Falaras, P.; Kontos, A. G.; Dunlop, P. S. M.; Hamilton, J. W. J.; Byrne, J. A.; O'Shea, K.; Entezari, M. H.; Dionysiou, D. D. *Appl. Catal. B Environ.* **2012**, *125*, 331–349.

(55) Lazar, M.; Varghese, S.; Nair, S. *Catalysts* **2012**, *2*, 572–601.

(56) Gaya, U. I.; Abdullah, A. H. *J. Photochem. Photobiol. C Photochem. Rev.* **2008**, *9* (1), 1–12.

(57) Fujishima, A.; Rao, T. *J. Chem. Sci.* **1997**, *109* (6), 471–486.

(58) Folli, A.; Jakobsen, U. H.; Guerrini, G. L.; Macphee, D. E. *J. Adv. Oxid. Technol.* **2009**, *12* (1), 126–133.

(59) Jiang, J.; Zhu, S.; Xu, W.; Cui, Z.; Yang, X. *Mater. Res. Bull.* **2015**, *65* (0), 302–306.

(60) Kelly, K. L.; Coronado, E.; Zhao, L. L.; Schatz, G. C. *J. Phys. Chem. B* **2003**, *107* (3), 668–677.

(61) Keleher, J.; Bashant, J.; Heldt, N.; Johnson, L.; Li, Y. *World J. Microbiol. Biotechnol.* **2002**, *18* (1996), 133–139.

(62) Chen, S. F.; Li, J. P.; Qian, K.; Xu, W. P.; Lu, Y.; Huang, W. X.; Yu, S. H. *Nano Res.* **2010**, *3* (4), 244–255.

(63) Jing, Z.; Wang, C.; Wang, G.; Li, W.; Lu, D. *J. Sol-Gel Sci. Technol.* **2010**, *56* (2), 121–127.

(64) Nakata, K.; Ochiai, T.; Murakami, T.; Fujishima, A. *Electrochim. Acta* **2012**, *84*, 103–111.

(65) Augustynski, J. *Electrochim. Acta* **1993**, *38* (1), 43–46.

(66) Zhang, J.; Zhou, P.; Liu, J.; Yu, J. *Phys. Chem. Chem. Phys.* **2014**, *16* (38), 20382–20386.

(67) Ohtani, B.; Ogawa, Y.; Nishimoto, S. *J. Phys. Chem. B* **1997**, *5647* (Iv), 3746–3752.

(68) Hou, Y.-Q.; Zhuang, D.-M.; Zhang, G.; Zhao, M.; Wu, M.-S. *Appl. Surf. Sci.* **2003**, *218* (1-4), 98–106.

(69) Ayllón, J. A.; Figueras, A.; Garelik, S.; Spirkova, L.; Durand, J.; Cot, L. *J. Mater. Sci. Lett.* **1999**, *18* (16), 1319–1321.

(70) Zhang, J.; Xu, Q.; Feng, Z.; Li, M.; Li, C. *Angew. Chemie - Int. Ed.* **2008**, *47* (9), 1766–1769.

(71) Kawahara, T.; Konishi, Y.; Tada, H.; Tohge, N.; Nishii, J.; Ito, S. *Angew. Chemie - Int. Ed.* **2002**, *41* (15), 2811–2813.

(72) Scanlon, D. O.; Dunnill, C. W.; Buckeridge, J.; Shevlin, S. a.; Logsdail, A. J.; Woodley, S. M.; Catlow, C. R. a.; Powell, M. J.; Palgrave, R. G.; Parkin, I. P.; Watson, G. W.; Keal, T. W.; Sherwood, P.; Walsh, A.; Sokol, A. a. *Nat. Mater.* **2013**, *12* (July), 1–4.

(73) Ohtani, B.; Prieto-Mahaney, O. O.; Li, D.; Abe, R. *J. Photochem. Photobiol. A Chem.* **2010**, *216*, 179–182.

(74) Bickley, R. I.; Gonzalez-Carreno, T.; Lees, J. S.; Palmisano, L.; Tilley, R. J. D. *J. Solid State Chem.* **1991**, *92* (1), 178–190.

(75) Veréb, G.; Ambrus, Z.; Pap, Z.; Kmetykó, Á.; Dombi, A.; Danciu, V.; Cheesman, A.; Mogyorósi, K. *Appl. Catal. A Gen.* **2012**, *417-418*, 26–36.

(76) Yu, J.; Zhou, P.; Li, Q. *Phys. Chem. Chem. Phys.* **2013**, *15* (29), 12040–12047.

(77) Dunnill, C. W.; Parkin, I. P. *Dalton Trans.* **2011**, *40* (8), 1635–1640.

(78) Ghosh, A. K.; Maruska, P. H. *J. Electrochem. Soc.* **1977**, *124* (10), 1516.

(79) Senthilkumaar, S.; Porkodi, K.; Gomathi, R.; Geetha Maheswari, a.; Manonmani, N. *Dye. Pigment.* **2006**, *69* (1-2), 22–30.

(80) Zhang, K.; Meng, Z.; Oh, W. *Cuihua Xuebao/Chinese J. Catal.* **2010**, *31* (7), 751–758.

(81) Liu, R.; Wang, P.; Wang, X.; Yu, H.; Yu, J. *J. Phys. Chem. C* **2012**, *116* (33), 17721–17728.

(82) Borgarello, E.; Kiwi, J.; Graetzel, M.; Pelizzetti, E.; Visca, M. *J. Am. Chem. Soc.* **1982**, *104* (11), 2996–3002.

(83) Khan, M. A.; Woo, S. I.; Yang, O. B. *Int. J. Hydrogen Energy* **2008**, *33* (20), 5345–5351.

(84) Zhou, J.; Zhang, Y.; Zhao, X.; Ray, A. *Ind. Eng. …* **2006**, *4* (3), 3503–3511.

(85) Triggs, P.; Lévy, F. *Phys. Status Solidi* **1985**, *129* (1), 363–374.

(86) Quan, X.; Tan, H.; Zhao, Q.; Sang, X. *J. Mater. Sci.* **2007**, *42*, 6287–6296.

(87) Jing, D.; Zhang, Y.; Guo, L. *Chem. Phys. Lett.* **2005**, *415* (1-3), 74–78.

(88) Anpo, M.; Takeuchi, M. *J. Catal.* **2003**, *216* (1-2), 505–516.

(89) Asahi, R.; Morikawa, T.; Ohwaki, T.; Aoki, K.; Taga, Y. *Science* **2001**, *293* (269), 269–271.

(90) Yan, X.; Ohno, T.; Nishijima, K.; Abe, R.; Ohtani, B. *Chem. Phys. Lett.* **2006**, *429* (4-6), 606–610.

(91) Park, H.; Choi, W. *J. Phys. Chem. B* **2004**, 4086–4093.

(92) Torres, G. R.; Lindgren, T.; Lu, J.; Granqvist, C. G.; Lindquist, S. E. *J. Phys. Chem. B* **2004**, *108* (19), 5995–6003.

(93) Tang, J.; Cowan, A.; Durrant; Klug, D. *J. Phys. Chem. C* **2011**, *115*, 3143–3150.

(94) Nishijima, K.; Ohtani, B.; Yan, X.; Kamai, T. A.; Chiyoya, T.; Tsubota, T.; Murakami, N.; Ohno, T. *Chem. Phys.* **2007**, *339* (1-3), 64–72.

(95) Luo, H.; Takata, T.; Lee, Y.; Zhao, J.; Domen, K.; Yan, Y. *Chem. Mater.* **2004**, *16* (5), 846–849.

(96) Fujishima, A.; Zhang, X.; Tryk, D. a. *Surf. Sci. Rep.* **2008**, *63* (12), 515–582.

(97) Sato, S. *Chem. Phys. Lett.* **1986**, *123* (1-2), 126–128.

(98) Chen, X.; Mao, S. S. *Chem. Rev.* **2007**, *107* (7), 2891–2959.

(99) Bessekhouad, Y.; Robert, D.; Weber, J. V. *J. Photochem. Photobiol. A Chem.* **2004**, *163* (3), 569–580.

(100) Brahimi, R.; Bessekhouad, Y.; Bouguelia, a.; Trari, M. *J. Photochem. Photobiol. A*

Chem. **2008**, *194* (2-3), 173–180.

(101) Sun, W.-T.; Yu, Y.; Pan, H.-Y.; Gao, X.-F.; Chen, Q.; Peng, L.-M. *J. Am. Chem. Soc.* **2008**, *130* (4), 1124–1125.

(102) Nazeeruddin, M. K.; Splivallo, R.; Liska, P.; Comte, P.; Grätzel, M. *Chem. Commun. (Camb).* **2003**, No. 12, 1456–1457.

(103) Bandara, J.; Mielczarski, J. a.; Kiwi, J. *Langmuir* **1999**, *15* (22), 7680–7687.

(104) Wu, T.; Liu, G.; Zhao, J.; Serpone, N. *J. Phys. Chem. B* **1998**, *5647* (1), 5845–5851.

(105) Wu, T.; Lin, T.; Zhao, J.; Hidaka, H.; Serpone, N. *Environ. Sci. Technol.* **1999**, *33* (9), 1379–1387.

(106) Zhao, J.; Wu, T.; Wu, K.; Oikawa, K. *Environ. Sci. Technol.* **1998**, *32* (16), 2394–2400.

(107) Naito, S. *J. Chem. Soc. Chem. Commun.* **1985**, No. 17, 1211.

(108) Sakthivel, S.; Shankar, M. V.; Palanichamy, M.; Arabindoo, B.; Bahnemann, D. W.; Murugesan, V. *Water Res.* **2004**, *38* (13), 3001–3008.

(109) Zhang, D. *Russ. J. Phys. Chem. A* **2012**, *86* (3), 498–503.

(110) Ryu, W.-H.; Lee, Y. W.; Nam, Y. S.; Youn, D.-Y.; Park, C. B.; Kim, I.-D. *J. Mater. Chem. A* **2014**, *2* (16), 5610.

(111) Xie, M.; Fu, X.; Jing, L.; Luan, P.; Feng, Y.; Fu, H. *Adv. Energy Mater.* **2014**, *4* (5).

(112) Serpone, N.; Maruthamuthu, P.; Pichat, P.; Pelizzetti, E.; Hidaka, H. *J. Photochem. Photobiol. A Chem.* **1995**, *85* (3), 247–255.

(113) Bessekhouad, Y.; Chaoui, N.; Trzpit, M.; Ghazzal, N.; Robert, D.; Weber, J. V. *J. Photochem. Photobiol. A Chem.* **2006**, *183* (1-2), 218–224.

(114) O'Regan, B.; Grätzel, M. *Nature* **1991**, *353* (6346), 737–740.

(115) Su, R.; Tiruvalam, R.; Logsdail, A. J.; He, Q.; Downing, C. a.; Jensen, M. T.; Dimitratos, N.; Kesavan, L.; Wells, P. P.; Bechstein, R.; Jensen, H. H.; Wendt, S.; Catlow, C. R. a; Kiely, C. J.; Hutchings, G. J.; Besenbacher, F. *ACS Nano* **2014**, *8* (4), 3490–3497.

(116) Bian, Z.; Tachikawa, T.; Zhang, P.; Fujitsuka, M.; Majima, T. *J. Am. Chem. Soc.* **2014**, *136* (1), 458–465.

(117) Jiang, Z.; Zhu, J.; Liu, D.; Wei, W.; Xie, J.; Chen, M. *CrystEngComm* **2014**, *16*, 2384.

(118) Bahruji, H.; Bowker, M.; Davies, P. R.; Morgan, D. J.; Morton, C. a.; Egerton, T. a.; Kennedy, J.; Jones, W. *Top. Catal.* **2014**, *58* (2-3), 70–76.

(119) Ji, X. Z.; Somorjai, G. a. *J. Phys. Chem. B* **2005**, *109* (47), 22530–22535.

(120) Borgarello, E.; Serpone, N.; Emo, G.; Harris, R.; Pelizzetti, E.; Minerolb, C. *Inorg. Chem.* **1986**, *25* (4), 4499–4503.

(121) Greaves, J.; Al-Mazroai, L.; Nuhu, A.; Davies, P.; Bowker, M. *Gold Bull.* **2006**, *39*, 216–219.

(122) Park, H.; Choi, W. *J. Phys. Chem. B* **2003**, *107*, 3885–3890.

(123) Tanaka, K.; Harada, K.; Murata, S. *Sol. Energy* **1986**, *36* (2), 159–161.

(124) Blondeel, G.; Porter, G.; Urwln, D. *J. Phys. Chem.* **1983**, *339* (87), 2629–2636.

(125) Kawai, T.; Sakata, T. *Chem. Phys. Lett.* **1980**, *72* (1), 87–89.

(126) Uddin, M. T.; Babot, O.; Thomas, L.; Olivier, C.; Redaelli, M.; D'Arienzo, M.; Morazzoni, F.; Jaegermann, W.; Rockstroh, N.; Junge, H.; Toupance, T. *J. Phys. Chem. C* **2015**, 150218095347003.

(127) Duonghong, D.; Borgarello, E.; Graetzel, M. *J. Am. Chem. Soc.* **1981**, *103* (00), 4685–4690.

(128) Bard, A. J. *J. Photochem.* **1979**, *10* (1), 59–75.

(129) Nozik, a. J. *Philos. Trans. R. Soc. A Math. Phys. Eng. Sci.* **1980**, *295* (1414), 453–470.

(130) Möllers, F.; Tolle, H. J.; Memming, R. *J. Electrochem. Soc.* **1974**, *121*, 1160.

(131) Kraeutler, B.; Bard, A. J. *J. Am. Chem. Soc.* **1978**, *13* (100), 4317–4318.

(132) Curran, J.; Domenech, J.; Jaffreziec-Renault, N.; Philippe, R. *J. Phys. Chem.* **1985**, *89* (6), 957–963.

(133) Harada, M.; Tamura, N.; Takenaka, M. *J. Phys. Chem. C* **2011**, *115*, 14081–14092.

(134) Sclafani, A.; Mozzanega, M.-N.; Pichat, P. *J. Photochem. Photobiol. A Chem.* **1991**, *59* (2), 181–189.

(135) Disdier, J.; Herrmann, J.-M.; Pichat, P. *J. Chem. Soc. Faraday Trans.* **1983**, *79*, 651–660.

(136) Jaffrezic-Renault, N.; Pichat, P.; Foissy, A.; Mercer, R. *J. Phys. Chem.* **1986**, *90* (13), 2733–2738.

(137) Uddin, M. T.; Nicolas, Y.; Olivier, C.; Toupance, T.; Müller, M. M.; Kleebe, H. J.; Rachut, K.; Ziegler, J.; Klein, A.; Jaegermann, W. *J. Phys. Chem. C* **2013**, *117* (42), 22098–22110.

(138) Lu, X.; Rycenga, M.; Skrabalak, S. E.; Wiley, B.; Xia, Y. *Annu. Rev. Phys. Chem.* **2009**, *60*, 167–192.

(139) Noguez, C. *J. Phys. Chem. C* **2007**, *111* (10), 3806–3819.

(140) Hutter, E.; Fendler, J. H. *Adv. Mater.* **2004**, *16* (19), 1685–1706.

(141) Hou, W.; Cronin, S. B. *Adv. Funct. Mater.* **2013**, *23* (13), 1612–1619.

(142) Ingram, D.; Linic, S. *J. Am. Chem. Soc.* **2011**, 5202–5205.

(143) Jain, P. K.; Huang, X.; El-Sayed, I. H.; El-Sayed, M. a. *Plasmonics* **2007**, *2*, 107–118.

(144) Linic, S.; Christopher, P.; Xin, H.; Marimuthu, A. *Acc. Chem. Res.* **2013**, *46* (8), 1890–1899.

(145) Zhang, X.; Chen, Y. L.; Liu, R.-S.; Tsai, D. P. *Rep. Prog. Phys.* **2013**, *76* (4), 046401.

(146) Zhou, X.; Liu, G.; Yu, J.; Fan, W. *J. Mater. Chem.* **2012**, *22* (40), 21337.

(147) Kochuveedu, S.; Kim, D. D. *J. Phys. Chem. C* **2012**, *116* (3), 2500–2506.

(148) Kowalska, E.; Mahaney, O. O. P.; Abe, R.; Ohtani, B. *Phys. Chem. Chem. Phys.* **2010**, *12* (10), 2344–2355.

(149) Tian, Y.; Tatsuma, T. *J. Am. Chem. Soc.* **2005**, *127* (20), 7632–7637.

(150) Awazu, K.; Fujimaki, M.; Rockstuhl, C.; Tominaga, J.; Murakami, H.; Ohki, Y.; Yoshida, N.; Watanabe, T. *J. Am. Chem. Soc.* **2008**, *130* (4), 1676–1680.

(151) Clavero, C. *Nat. Photonics* **2014**, *8* (2), 95–103.

(152) Langhammer, C.; Yuan, Z.; Zorić, I.; Kasemo, B. *Nano Lett.* **2006**, *6* (4), 833–838.

(153) Langhammer, C.; Kasemo, B.; Zorić, I. *J. Chem. Phys.* **2007**, *126* (19), 194702.

(154) Gonçalves, M. S. T.; Oliveira-Campos, A. M. F.; Pinto, E. M. M. S.; Plasência, P. M. S.; Queiroz, M. J. R. P. *Chemosphere* **1999**, *39* (5), 781–786.

(155) Konstantinou, I. K.; Albanis, T. a. *Appl. Catal. B Environ.* **2004**, *49* (1), 1–14.

(156) Zhao, J.; Chen, C.; Ma, W. *Top. Catal.* **2005**, *35* (3-4), 269–278.

(157) Sökmen, M.; Özkan, a. *J. Photochem. Photobiol. A Chem.* **2002**, *147* (1), 77–81.

(158) Zhang, Q.; Lima, D. Q.; Lee, I.; Zaera, F.; Chi, M.; Yin, Y. *Angew. Chemie - Int. Ed.* **2011**, *50* (31), 7088–7092.

(159) Chen, J.; Wu, J.; Wu, P.; Tsai, D. *J. Phys. …* **2010**, 210–216.

(160) Lee, J.; Mubeen, S.; Ji, X.; Stucky, G. D.; Moskovits, M. *Nano Lett.* **2012**, *12* (9), 5014–5019.

(161) Linic, S.; Christopher, P.; Ingram, D. B. *Nat. Mater.* **2011**, *10* (12), 911–921.

(162) Liu, Z.; Hou, W.; Pavaskar, P.; Aykol, M.; Cronin, S. B. *Nano Lett.* **2011**, *11*, 1111–1116.

(163) Haque, M. M.; Muneer, M. *J. Hazard. Mater.* **2007**, *145* (1-2), 51–57.

(164) Al-Mazroai, L. S.; Bowker, M.; Davies, P.; Dickinson, A.; Greaves, J.; James, D.; Millard, L. *Catal. Today* **2007**, *122* (1-2), 46–50.

(165) Yu, K. M. K.; Tong, W.; West, A.; Cheung, K.; Li, T.; Smith, G.; Guo, Y.; Tsang, S. C. E. *Nat. Commun.* **2012**, *3*, 1230.

(166) Hussein, F. H.; Rudham, R. *J. Chem. Soc. Faraday Trans. 1 Phys. Chem. Condens. Phases* **1987**, *83* (5), 1631.

(167) Chiarello, G. L.; Ferri, D.; Selli, E. *J. Catal.* **2011**, *280* (2), 168–177.

(168) Carey, J. H.; Lawrence, J.; Tosine, H. M. *Bull. Environ. Contam. Toxicol.* **1976**, *16* (6), 697–701.

(169) Bideau, M.; Claudel, B.; Otterbein, M. *J. Photochem.* **1980**, *14* (4), 291–302.

(170) Izumi, I.; Dunn, W. W.; Wllbourn, K.; Fan, F. F.; Bard, A. J. *J. Phys. Chem.* **1980**, *84*, 3207–3210.

(171) Izumi, I.; Fan, F.; Bard, A. *J. Phys. Chem.* **1981**, *85*, 218–223.

(172) Herrmann, J.-M.; Mozzanega, M.-N.; Pichat, P. *J. Photochem.* **1983**, *22* (4), 333–

343.

(173) Yoneyama, H.; Takao, Y.; Tamura, H.; Bard, a J. *J. Phys. Chem.* **1983**, *87* (14), 1417–1422.

(174) Rochkind, M.; Pasternak, S.; Paz, Y. *Molecules* **2014**, *20* (1), 88–110.

(175) Zheng, Z.; Huang, B.; Qin, X.; Zhang, X.; Dai, Y.; Whangbo, M.-H. *J. Mater. Chem.* **2011**, *21* (25), 9079.

(176) Asenjo, N. G.; Santamaría, R.; Blanco, C.; Granda, M.; Álvarez, P.; Menéndez, R. *Carbon N. Y.* **2013**, *55*, 62–69.

(177) Tunesi, S.; Anderson, M. *J. Phys. Chem.* **1991**, *95* (8), 3399–3405.

(178) García-Zaleta, D. S.; Montes De Oca-Valero, J. a.; Torres-Huerta, A. M.; Domínguez-Crespo, M. a.; Dorantes-Rosales, H. J.; López-González, R.; García-Murillo, A. *J. Nano Res.* **2014**, *28*, 9–20.

(179) Kim, J.; Monllor-Satoca, D.; Choi, W. *Energy Environ. Sci.* **2012**, *5* (6), 7647.

(180) Ibhadon, A.; Fitzpatrick, P. *Catalysts* **2013**, *3*, 189–218.

(181) Park, J. Y.; Lee, I. H. *Korean J. Chem. Eng.* **2009**, *26* (2), 387–391.

(182) Muggli, D. S.; Keyser, S. a; Falconer, J. L. *Catal. Letters* **1998**, *55*, 129–132.

(183) Muggli, D. S.; Falconer, J. L. *J. Catal.* **1999**, *187*, 230–237.

(184) Grzechulska, J.; Morawski, A. W. *Appl. Catal. B Environ.* **2002**, *36* (1), 45–51.

(185) Amala Infant Joice, J.; Sivakumar, T.; Ramakrishnan, R.; Ramya, G.; Shanmuga Prasad, K. P.; Arul Selvan, D. *Chem. Eng. J.* **2012**, *210*, 385–397.

(186) Zhang, F.; Zhaoa, J.; Shen, T.; Hidakab, H.; Pelizzettic, E.; Serponed, N. *Appl. Catal. B Environ.* **1998**, *15*, 147–156.

(187) Chen, F.; Zhao, J.; Hidaka, H. *Int. J. Photoenergy* **2003**, *5* (4), 209–217.

(188) Asiltürk, M.; Sayilkan, F.; Erdemoğlu, S.; Akarsu, M.; Sayilkan, H.; Erdemoğlu, M.; Arpaç, E. *J. Hazard. Mater.* **2006**, *129* (1-3), 164–170.

(189) Li, J.; Ma, W.-H.; Lei, P.-X.; Zhao, J.-C. *J. Environ. Sci. (China)* **2007**, *19* (7), 892–896.

(190) Lakshmi, S.; Renganathan, R.; Fujita, S. *J. Photochem. Photobiol. A Chem.* **1995**, *88* (2-3), 163–167.

(191) Kawai, T.; Sakata, T. *J. Chem. Soc. Chem. Commun.* **1980**, *47* (15), 694.

(192) Cubeiro, M. L.; Fierro, J. L. G. *Appl. Catal. A Gen.* **1998**, *168* (2), 307–322.

(193) Zhou, C.; Ren, Z.; Tan, S.; Ma, Z.; Mao, X.; Dai, D.; Fan, H.; Yang, X.; LaRue, J.; Cooper, R.; Wodtke, A. M.; Wang, Z.; Li, Z.; Wang, B.; Yang, J.; Hou, J. *Chem. Sci.* **2010**, *1* (5), 575.

(194) Sakata, T.; Kawai, T. *Chem. Phys. Lett.* **1981**, *80* (2), 341–344.

(195) Bahruji, H.; Bowker, M.; Brookes, C.; Davies, P. R.; Wawata, I. *Appl. Catal. A Gen.* **2013**, *454*, 66–73.

(196) Tamaki, Y.; Furube, A.; Murai, M.; Hara, K.; Katoh, R.; Tachiya, M. *J. Am. Chem. Soc.* **2006**, *128* (2), 416–417.

(197) Bahruji, H.; Bowker, M.; Davies, P. R.; Al-Mazroai, L. S.; Dickinson, A.; Greaves, J.; James, D.; Millard, L.; Pedrono, F. *J. Photochem. Photobiol. A Chem.* **2010**, *216* (2-3), 115–118.

(198) Guillard, C.; Lachheb, H.; Houas, A.; Ksibi, M.; Elaloui, E.; Herrmann, J. M. *J. Photochem. Photobiol. A Chem.* **2003**, *158* (1), 27–36.

(199) Araña, J.; Martínez Nieto, J. L.; Herrera Melián, J. a.; Doña Rodríguez, J. M.; González Díaz, O.; Pérez Peña, J.; Bergasa, O.; Alvarez, C.; Méndez, J. *Chemosphere* **2004**, *55* (6), 893–904.

(200) Santhanalakshmi, J.; Komalavalli, R.; Venkatesan, P. *Nanosci. Nanotechnol.* **2012**, *2* (1), 8–12.

(201) Alkaim, A. F.; Aljeboree, A. M.; Alrazaq, N. A.; Baqir, S. J.; Hussein, F. H.; Lilo, A. J. *Asian J. Chem.* **2014**, *26* (24), 8445–8448.

(202) Ni, M.; Leung, M. K. H.; Leung, D. Y. C.; Sumathy, K. *Renew. Sustain. Energy Rev.* **2007**, *11* (3), 401–425.

(203) Maeda, K. *J. Photochem. Photobiol. C Photochem. Rev.* **2011**, *12* (4), 237–268.

(204) Zhu, J.; Zäch, M. *Curr. Opin. Colloid Interface Sci.* **2009**, *14* (4), 260–269.

(205) Kudo, A.; Miseki, Y. *Chem. Soc. Rev.* **2009**, *38* (1), 253–278.

(206) Moniz, S. J. a.; Shevlin, S. a.; Martin, D. J.; Guo, Z.-X.; Tang, J. *Energy Environ. Sci.* **2015**, *8*, 731–759.

(207) Sayama, K.; Arakawa, H. *J. Chem. Soc. Faraday Trans.* **1997**, *93* (8), 1647–1654.

(208) Harada, H.; Ueda, T. *Chemical Physics Letters*. 1984, pp 229–231.

(209) Dickinson, A.; James, D.; Perkins, N.; Cassidy, T.; Bowker, M. *J. Mol. Catal. A Chem.* **1999**, 211–221.

(210) Bowker, M.; Morton, C.; Kennedy, J.; Bahruji, H.; Greves, J.; Jones, W.; Davies, P. R.; Brookes, C.; Wells, P. P.; Dimitratos, N. *J. Catal.* **2014**, *310*, 10–15.

(211) Ismail, A. a; Robben, L.; Bahnemann, D. W. *Chemphyschem* **2011**, *12* (5), 982–991.

(212) Heinzel, a.; Vogel, B.; Hübner, P. *J. Power Sources* **2002**, *105* (2), 202–207.

(213) Polo, A. S.; Santos, M. C.; De Souza, R. F. B.; Alves, W. a. *J. Power Sources* **2011**, *196* (2), 872–876.

(214) Herrmann, J. *Catal. Today* **1999**, *53* (1), 115–129.

(215) Tiwari, D.; Dunn, S. *Mater. Lett.* **2012**, *79*, 18–20.

(216) Jacobs, J. *J. Phys. Chem.* **1986**, *90*, 6507–6517.

(217) Finney, E. E.; Finke, R. G. *J. Colloid Interface Sci.* **2008**, *317* (2), 351–374.

(218) Aarthi, T.; Madras, G. *Ind. Eng. Chem. Res.* **2007**, 7–14.

(219) Li, J.; Liu, X.; Pan, L.; Qin, W.; Sun, Z. *RSC Adv.* **2014**, *4*, 62387–62392.

(220) Yu, K.; Yang, S.; He, H.; Sun, C.; Gu, C.; Ju, Y. *J. Phys. Chem. A* **2009**, *113* (37), 10024–10032.

(221) Serpone, N.; Sauve, G.; Koch, R.; Tahiri, H. *J. Photochem. Photobiol. A Chem.* **1996**, *94* (2-3), 191–203.

(222) Fox, M. A.; Dulay, M. T. *Chem. Rev.* **1993**, *93*, 341–357.

(223) Hinckley, D. a.; Seybold, P. G.; Borris, D. P. *Spectrochim. Acta Part A Mol. Spectrosc.* **1986**, *42* (6), 747–754.

(224) Ramette, R. W.; Sandell, E. B. *J. Am. Chem. Soc.* **1956**, *78* (19), 4872–4878.

(225) Sakthivel, S.; Neppolian, B. *Sol. Energy Mater. …* **2003**, *77* (3), 65–82.

(226) Lide, D. R. *CRC Handbook of Chemistry and Physics*, 85th ed.; CRC Press, 2004.

(227) Wodka, D.; Bielaníska, E.; Socha, R. P.; Elzbieciak-Wodka, M.; Gurgul, J.; Nowak, P.; Warszyníski, P.; Kumakiri, I. *ACS Appl. Mater. Interfaces* **2010**, *2* (7), 1945–1953.

(228) Chung, I.; Lee, B.; He, J.; Chang, R. P. H.; Kanatzidis, M. G. *Nature* **2012**, *485* (7399), 486–489.

(229) Xiong, Y.; Chen, J.; Wiley, B.; Xia, Y.; Yin, Y.; Li, Z. Y. *Nano Lett.* **2005**, *5* (7), 1237–1242.

(230) Qadir, K.; Joo, S. H.; Mun, B. S.; Butcher, D. R.; Renzas, J. R.; Aksoy, F.; Liu, Z.; Somorjai, G. a.; Park, J. Y. *Nano Lett.* **2012**, *12* (11), 5761–5768.

(231) Bahruji, H.; Bowker, M.; Davies, P. R.; Kennedy, J.; Morgan, D. J. *Int. J. Hydrogen Energy* **2014**, *40* (3), 2–8.

(232) Maeda, K.; Murakami, N.; Ohno, T. *J. Phys. Chem. C* **2014**, *118* (17), 9093–9100.

APPENDICES

Appendix A GC calibration

A.1 Silica gel packed column

The calibration was performed using N_2 and a column temperature of 80°C. Before calibration the column was condition by ramping from 110°C to 290°C at 5°C/min and holding at 290°C for 180 min.

A.1.1 Preparation of gas mixtures

First, three microwave vials fitted with a balloon each were evacuated using a vacuum pump. Two of the vials were filled with pure gas; one with $H_2$and the other with N_2. A total gas volume of 20 mL was used such that H_2 concentrations of 1%, 2%, 3%, 4% and 5% could be prepared in N_2.

In the third empty sealed and evacuated vial, H_2/N_2 mixtures were prepared by inserting 19.8 mL of N_2 and 0.2 mL of H_2 for a 1% mixture; 19.6 mL N_2 and 0.4 mL H_2 for a 2% mixture; 19.4 mL N_2 and 0.6 mL H_2 for a 3% mixture, etc. up to 5%

For each mixture of gas 0.1 mL was injected into the GC and measured. These were repeated 3 times.

This process gave a good calibration curve and the measured values for the percentages of each gas were reproducible. However, there was a systematic error introduced using this process that made the values obtained for all percentages higher than the values obtained using the gas calibration standards purchased from Scotty. This is thought to be due to the dead volume of the syringe needle, where there may have been extra H_2 to account for the systematic error.

A.1.2 Gas standards measurement and normalisation

The calibration standards are reliable in accuracy up to ± 0.01% and the percentage of H_2 was by injecting 0.1 mL for 1% H_2, 0.2 mL for 2% H_2 and 0.3 mL for 3% H_2. The percentage of H_2 was taken as the height of the peak rather than the area since poor resolution between H_2 and O_2 under these conditions could affect the results.

The calibration standards were not used as the sole H_2 source for the GC calibration since measuring each increase in H_2 percentage meant an increase in the injected gas volume, which contributed to an uncertainty in the calibration. The resulting calibrations were not reliable. Instead, a 3 point calibration was performed with the gas standards with which to normalise the 5 point calibration carried out with the prepared mixture.

Table A.1 Results of the detected H_2 peaks using the prepared gas mixtures and the average value obtained for each percentage

Mixtures

Volume used	apparent H_2/ %	detector peak			average
0.1	1	26.584	23.729	23.81	24.71
0.1	2	56.247	51.985	52.25	53.49
0.1	3	82.662	79.2	76.249	79.37
0.1	4	94.306	97.327	97.115	96.25
0.1	5	126.906	118.303	120.49	121.90

Table A.2 Results of the detected H_2 peaks using the calibration standards and the average value obtained for each percentage

Gas standards

volume used	H_2 %	detector peak/ mV			average
0.1	1	12.146	10.888	11.26	11.43
0.2	2	24.029	30.09	18.074	24.06
0.3	3	36.56	40.018	44.709	40.43

A straight line fit was plotted on excel and this Equation was used to calculate the equivalent percentages measured using the gas mixtures. This way the values measure using the gas mixtures are normalised to accurate values and a good calibration curve was obtained.

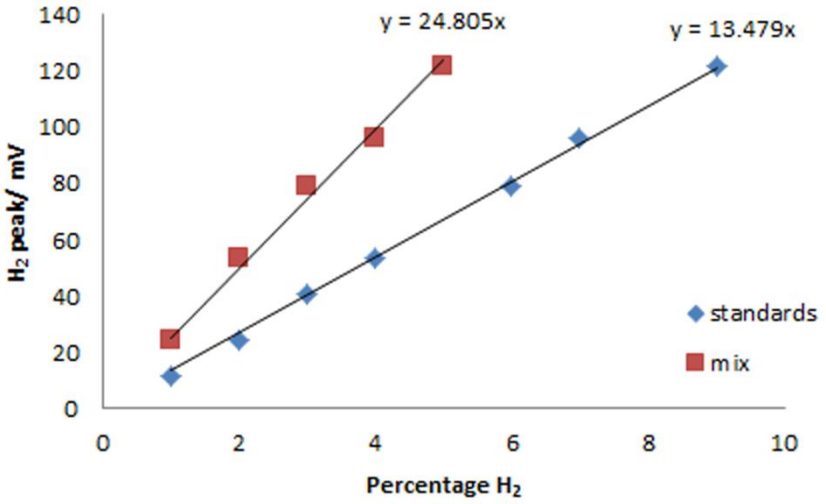

Figure A.1 Calibration curves obtained from the prepared mix

Appendix B Plasmon fit calculations

B.1 Normal distribution function

The diffuse reflectance UV-vis measurements of the synthesised catalysts were analysed in MS Excel. In order to fit the plasmon curves to the UV-vis results a normal distribution function of the form given in Equation B.1 was used:

$$f(a,\mu,\sigma) = \frac{a}{\sigma\sqrt{\pi/2}} \exp\left(-2\frac{(x_i-\mu)^2}{\sigma}\right) \quad \textbf{(B.1)}$$

where a is the amplitude of the distribution curve, μ is the position of the centre of the peak and σ is the standard deviation or width of the curve.

Using the solver add-in with MS Excel, the three variables a, μ and σ were altered to find the best fit to each UV-vis measurement. The result gave the position of the plasmon peak, the amplitude of the peak and the distribution from the centre.

Appendix C Error analysis of TEM measurements

C.1 Pd nanoparticle size measurements

The size of the Pd nanoparticles was measured from the TEM micrographs obtained for each catalyst using the ImageJ software package. The total amount of measurements per catalyst was dependent on the number and quality of the TEM images obtained. The software includes a command to return the mean value and standard deviation from the mean. This value of the standard deviation was used to calculate the uncertainty. The uncertainty in the measurements of the photochemically reduced nanoparticles was calculated using Equation C.1.

$$SE_{\bar{x}} = \frac{s_N}{\sqrt{n}} \quad \textbf{(C.1)}$$

Where SE_x is the standard error, S_N is the standard deviation and n is the number measurements. The standard deviation is given by Equation C.2:

$$s_N = \sqrt{\frac{1}{n}\sum_{i=1}^{n}(x_i - \bar{x})^2} \quad \textbf{(C.2)}$$

Equation C.2 is normally used to calculate the standard deviation however, in this instance the value of the standard deviation was automatically calculated by the program ImageJ and these values were used in ascertaining the standard error in the measurement of the Pd nanoparticle sizes.

The average size of the nanoparticles as measured using ImageJ as well as the standard deviation for each photocatalyst and the total number of particle size measurments made for each catalyst is presented in Table C.1.

Table C.1 Average size and standard error of photochemically deposited Pd of each catalyst

Photocatalyst	Mean Pd diameter/ nm	Standard deviation/ nm	Total number of particles measured
AL091	2.6	0.6	64
AL092	1.6	0.4	104
AL093	1.9	0.4	159
AL094	2.1	0.5	84
AL095	1.8	0.3	91
AL096	1.4	0.4	41
AL097	2.0	0.7	139
AL098	2.5	0.8	182
AL099	2.8	0.5	120
AL100	2.2	0.5	36
AL101	1.5	0.3	90
AL102	1.3	0.3	37
AL103	2.4	0.7	150
AL104	1.2	0.3	107
AL105	1.7	0.8	105
AL106	2.2	0.5	26
AL107	1.9	0.8	101
AL108	2.4	0.5	96
AL109	2.9	0.7	133
AL110	1.9	0.5	96
AL111	1.9	0.5	91
AL112	1.7	0.4	75
AL113	2.0	0.5	42
AL114	1.7	0.5	110

Appendix D Full list of synthesised photocatalysts

Table D.1 List of all the synthesised photocatalyst

10ml 0.01M @ 2.05 mW/cm2	$PdCl_2$/ mol/L	Vol. of solution/ ml	Pd per gram of catalyst/ mg	dye adsorption/%	$t_{1/2}$/ min	Irradiance/ mW/ cm^2	irradiation time/ min	Plasmon peak/ nm
AL091	0.01	10	5.195	7.4	1.00	2.05	30	379
AL093	0.01	10	4.21	9.39	1.01	2.05	3	437
AL094	0.01	10	5.331	18.3	0.53	2.05	1	446
AL095	0.01	10	5.287	12.05	1.40	2.05	0.167	437
10ml 0.01M @ 9.54 mW/cm2	$PdCl_2$/ mol/L	Vol. of solution/ ml	Pd per gram of catalyst/ mg	dye adsorption/%	$t_{1/2}$/ min	Irradiance/ mW/ cm^2	irradiation time/ min	Plasmon peak/ nm
AL119	0.01	10	-	10.0	0.90	9.54	60	-
AL092	0.01	10	5.442	12.3	3.28	9.54	30	477
AL112	0.01	10	4.868	-	1.17	9.54	3	409
AL096	0.01	10	5.451	20.5	0.63	9.54	1	442
AL097	0.01	10	4.851	10.1	0.43	9.54	0.167	438
5ml 0.02M @ 9.54 mW/cm2	$PdCl_2$/ mol/L	Vol. of solution/ ml	Pd per gram of catalyst/ mg	dye adsorption/%	$t_{1/2}$/ min	Irradiance/ mW/ cm^2	irradiation time/ min	Plasmon peak/ nm
AL098	0.02	5	5.817	11.4	0.66	9.54	30	453
AL099	0.02	5	5.924	18.6	0.55	9.54	3	438
AL100	0.02	5	5.814	12.0	0.83	9.54	1	432
AL101	0.02	5	5.885	16.0	0.95	9.54	0.167	430
5ml 0.02M @ 2.05 mW/cm2	$PdCl_2$/ mol/L	Vol. of solution/ ml	Pd per gram of catalyst/ mg	dye adsorption/%	$t_{1/2}$/ min	Irradiance/ mW/ cm^2	irradiation time/ min	Plasmon peak/ nm
AL102	0.02	5	5.953	11.5	1.15	2.05	30	440
AL103	0.02	5	5.886	15.1	0.58	2.05	3	448
AL104	0.02	5	5.751	13.2	0.92	2.05	1	441
AL105	0.02	5	5.887	12.7	1.19	2.05	0.167	435
10ml 0.02M @ 9.54 mW/cm2	$PdCl_2$/ mol/L	Vol. of solution/ ml	Pd per gram of catalyst/ mg	dye adsorption/%	$t_{1/2}$/ min	Irradiance/ mW/ cm^2	irradiation time/ min	Plasmon peak/ nm
AL106	0.02	10	6.118	14.2	0.46	9.54	30	454
AL113	0.02	10	6.262		0.77	9.54	3	432
AL107	0.02	10	5.898	17.3	0.92	9.54	1	419
AL108	0.02	10	5.845	12.3	0.38	9.54	0.167	439

Table D.1 (Cont.) List of all the synthesised photocatalyst

10ml 0.02M @ 2.05 mW/cm2	$PdCl_2$/ mol/L	Vol. of solution/ ml	Pd per gram of catalyst/ mg	dye adsorption/ %	$t_{1/2}$/ min	Irradiance/ mW/ cm^2	irradiation time/ min	Plasmon peak/ nm
AL109	0.02	10	6.272	13.9	0.36	2.05	30	454
AL114	0.02	10	6.46	10.9	0.46	2.05	3	447
AL110	0.02	10	5.407	14.6	0.52	2.05	1	428
AL111	0.02	10	6.281	22.2	0.53	2.05	0.167	425
10ml 0.005M @ 9.54 mW/cm2	$PdCl_2$/ mol/L	Vol. of solution/ ml	Pd per gram of catalyst/ mg	dye adsorption/ %	$t_{1/2}$/ min	Irradiance/ mW/ cm^2	irradiation time/ min	Plasmon peak/ nm
AL122	0.005	10	4.898	10.7	1.18	9.54	30	453
AL121	0.005	10	5.066	11.1	1.59	9.54	3	440
AL120	0.005	10	5.201	6.4	1.37	9.54	1	437
AL118	0.005	10	4.818	9.9	1.08	9.54	0.167	437
AL117	0.005	10	4.423	6.0	1.39	9.54	0.0167	439
10ml 0.001M @ 9.54 mW/cm2	$PdCl_2$/ mol/L	Vol. of solution/ ml	Pd per gram of catalyst/ mg	dye adsorption/ %	$t_{1/2}$/ min	Irradiance/ mW/ cm^2	irradiation time/ min	Plasmon peak/ nm
AL115	0.001	10	-	7.8	4.32	9.54	1	-
AL116	0.001	10	-	11.4	4.33	9.54	0.0167	-
Others	$PdCl_2$/ mol/L	Vol. of solution/ ml	Pd per gram of catalyst/ mg	dye adsorption/ %	$t_{1/2}$/ min	Irradiance/ mW/ cm^2	irradiation time/ min	Plasmon peak/ nm
AL132	0.02 (PdNO3)	10	-	5.8	43.05	9.54	3	no peak
AL133	0.1	10	-	19.1	0.65	9.54	3	-

Appendix E Dye degradation error analysis

E.1 Uncertainties in catalyst loading

The values of k_{app} at each catalyst loading were obtained by plotting a $\ln(C_0/C)$ versus time graph where the slope of the straight line, $m = k_{app}$.

At each catalyst loading, n values of k_{app} were obtained depending on the number of values of C measured during dye decolourisation tests. The standard error of the average k_{app} value at each catalyst loading was obtained using Equation C.1 and Equation C.2.

Table E.1 Mean k_{app} values and the standard error of the mean (SE_x) at a range of catalyst loadings

Catalyst loading/g/ L	mean k_{app}	SE_x
7	1.379	0.079
6	1.700	0.052
5	1.462	0.023
4	1.632	0.126
3	1.272	0.144
2	0.817	0.052
1	0.690	0.007